Designing Solid Electrolytes for Rechargeable Solid-State Batteries

Haowei Zhai

Submitted in partial fulfillment of the
requirements for the degree of
Doctor of Philosophy
in the Graduate School of Arts and Sciences

COLUMBIA UNIVERSITY

2019

ABSTRACT

Designing Solid Electrolytes for Rechargeable Solid-State Batteries

Haowei Zhai

Lithium-ion battery (LIB) is an indispensable energy storage device in portable electronics, and its applications in electric vehicles and grid-level energy storage are increasing dramatically in recent years due to high demands. To meet energy demands and address fire hazards, next generation batteries with better safety, higher energy density, and longer cycle life have been actively investigated. In this thesis, works on polymer and ceramic solid electrolytes to improve safety and energy density of rechargeable solid-state batteries are discussed.

In the first section, a flexible composite solid electrolyte is presented. Since ceramic electrolytes have high conductivities but are fragile, and polymer electrolytes are easy to process but have low conductivities, we propose a composite structure that combines these advantages. A vertically aligned and connected ceramic electrolyte is realized through the ice-templating method to improve the ionic conduction. Then a polyether-based polymer electrolyte is added to make the composite electrolyte flexible. Specifically, vertically aligned and connected LATP and LAGP nanoparticles (NPs) in the polyethylene oxide (PEO) matrix are made. The conductivity reaches 0.52×10^{-4} S/cm for LATP/PEO, and 1.67×10^{-4} S/cm for aligned LAGP/PEO composite electrolytes, which are several times higher than that with randomly dispersed LATP/LAGP NPs in PEO. Compared to the pure PEO electrolyte, the mechanical and thermal stabilities of the composite solid electrolyte are higher. The LFP-LAGP/PEO-Li cell with 148.7 mAh/g during the first discharge at 0.3C has over 95% capacity retention after 200 cycles. This method opens a new approach to optimize ion conduction in composite solid electrolytes for solid-state batteries.

In the next section, polyether-based polymer electrolytes such as PEO and PEG are studied. Polyether-based electrolytes are electrochemically unstable above 4 V, restricting their use with high voltage cathodes such as NMC for high energy density. A technique involving atomic layer deposition (ALD) of Al_2O_3 to stabilize the polyether-based electrolyte with 4 V class cathodes is described. With a 2 nm Al_2O_3 coating, the capacity retention stays at 84.7% after 80 cycles and 70.3% after 180 cycles for the polyether-based electrolyte. Without the coating, the capacity drops more than 50% after only 20 cycles. This study opens new opportunity to develop safe electrolytes for lithium batteries with high energy density.

In the final section, we propose a new polymer electrolyte, a poly(vinylidene fluoride) (PVDF) polymer electrolyte with organic plasticizer dimethylformamide (DMF), which possesses compatibility with 4V cathode for high energy density and high ionic conductivity (1.2×10^{-4} S/cm) at room temperature. This polymer electrolyte can be used as a supplement for the polyether-based electrolytes we discussed in the first two sections. In this polymer electrolyte, palygorskite ($(Mg,Al)_2Si_4O_{10}(OH)$) nanowires are introduced to form composite solid electrolytes (CPE) to enhance both stiffness and toughness of PVDF/DMF-based polymer electrolyte. With 5 wt % of palygorskite nanowires, the elastic modulus of the PVDF-DMF CPE increases from 9.0 MPa to 96 MPa, and its yield stress increases by 200%. We further demonstrate that full cells composed of $Li(Ni_{1/3}Mn_{1/3}Co_{1/3})O_2$ (NMC 111) cathode, PVDF-DMF/palygorskite CPE, and lithium metal anode, can be cycled over 200 times at 0.3 C, with 97% capacity retention. Moreover, the PVDF-DMF electrolyte is nonflammable, making it a safer alternative to the conventional liquid electrolyte. Our work illustrates that the PVDF-DMF/palygorskite CPE is a promising electrolyte for solid state batteries with better safety and cycling performance.

Collectively, we study the polyether-based polymer electrolyte and ceramic electrolyte to combine their advantages through the ice-templating method in a battery, use ALD technique to stabilize polyether-based electrolyte for high energy density, and propose an alternative PVDF/DMF-based polymer electrolyte with nanowire additives for high energy density and stable cycling, contributing to the rechargeable solid-state batteries, with better safety, higher energy density and better cycling stability.

Table of Contents

List of Figures

List of Tables

Acknowledgements

I would like to extend my sincere gratitude to my advisor Prof. Yuan Yang for all his guidance, support, encouragement and concern throughout my entire Columbia experience for my PhD studies. Yuan is not only a professional coach to me, but also an older brother, who has given me countless instruction and advice for my career and life philosophy. He introduced battery to me in my first year at Columbia and inspired my passion for this subject, and consequently I hope this will be a major part of my future career. His constant patience and critical opinions provided a path for my research experience. I have been very fortunate to have him as my supervisor, mentor and friend for life.

I would like to thank Prof. James Im, Prof. Simon J. L. Billinge, Prof. William E. Bailey, Prof. Xavier Roy, for being my Ph.D. defense committee members.

I would like to thank the whole Yang group for support and help in the past four years. I would like to acknowledge help from Dr. Zeyuan Cao for his tutoring. I would like to thank help from Dr. Qian Cheng, Jyotirmoy Mandal for giving me precious comments during my research. I would like to thank Dr. Bin Zhu, Dr. Yali Qiao, Mingqiang Ning, Pengyu Xu, Sicen Du, Shui Jing, Ji Tong, Keren He, Hao Fan, Pengcheng Yao, Yuxiang Zhu, Weiheng Xu, Nathan Fritz, Xiujia Yang, Yanke Fu, Nan Ni, Guoyu Qian, Boyu Qie, Xinyue Li, Zhe Sang, Kerui Sun, Aijun Li, Xue Wang, Bingqing Xu, Meijie Chen, Zeyu Hui, Tianwei Jin, Tianyang Wang, Tianyao Gong, Changmin Shi, Qingquan Song, Laiyuan Tan, Yijun Chen, Wenlong Huang, Peiyu Wang, Zhenxuan Fu, Zeyuan Li, and Hanrui Zhang for their assistance.

My acknowledgements also go to Prof. Simon J. L. Billinge for his guidance during the first semester I was at Columbia University.

I would like to thank Prof. Alan C. West and Prof. Daniel Esposito for pleasant collaboration on high energy density lithium batteries with stable cycling, and Prof. Kristin Myers and Dr. Charles Jayyosi for working on the mechanical properties of the solid electrolytes.

Furthermore, I would like to thank all my friends that I was lucky enough to meet, especially those at Columbia. I enjoy the life here in the last four years as I am lucky to know you. They include but not limited to Xiangbiao Liao, Xiaolong Wu, Shuoxun Wang, Tianze Cao, Long Yang, Alexander Beecher, Octavi Semonin, Wei Cao, Xun Wang, Tianjian Chen, Xi Chen, Hanqing Fan, Qiang Zeng, Jingwei Gao, Ming Gao, Weichang Ge, Dongrong Li, Mingjun Li, Yuanchunyu Lin, Zhexi Lin, Jiaxing Liu, Tingkai Liu, Xiangye Liu, Kuo Ren, Chen Shi, Ruobing Song, Dale Zhao, Bigeng Wang, Tianle Wang, Wanyin Yu, Nan Jiang, and Junkai Zhang.

I'd like to offer my sincere thanks to Mr. Luming Ai and Wuhan Dangdai Science & Technology Industries Group, Columbia University, and Gotion Inc. for their generous and persistent financial and personal support for my thesis research. I cannot finish my PhD without support from these agencies and fellowships.

Finally, I also want to express my appreciation to my family, especially my parents Zhihong Zhai and Shumei Zhang, my grandparents Guangyu Zhai and Guiying Wang for their infinite love, support and encouragement that fostered me with a positive personality and enhanced my self-confidence allowing me to achieve this wonderful goal.

Chapter 1: Introduction

1.1 Motivation

In recent years, the demand of clean energy, including batteries, solar, wind energy etc. is continuously booming due to electricity demand increase, global warming situation and shortage in oil production. Among them, batteries are attractive and play a very important role in portable electronics and electric vehicles.

Especially in electric vehicle market, the global stock of electric cars surpassed 3 million vehicles in 2017 after crossing the 1 million in 2015 and the 2 million marks in 2016. In 2017, China had the largest electric car stock: 40% of the global total, whereas the European and the US each occupied about a quarter of the global total. Norway has the world's highest share at 6.4% of electric cars in its vehicle stock. While the number of electric cars is notably on the rise, only three of the countries have a stock share of 1% or higher: Norway (6.4%), Netherlands (1.6%) and Sweden (1.0%). In addition to the 3.1 million passenger electric cars, there were around 250,000 electric light commercial vehicles (LCVs) on the road in 2017.

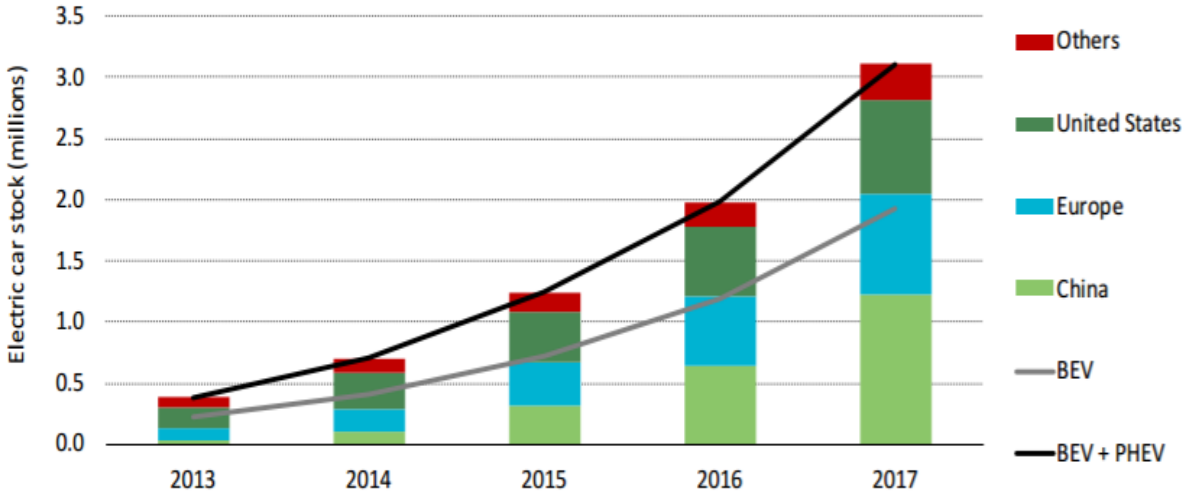

Figure 1.1. Evolution of the global electric vehicle market. Source: Sources: IEA analysis based on country submissions, complemented by ACEA (2018); EAFO (2018a)

In recent years, the global electric vehicle market has grown dramatically, with the annual sales around 1.2 million in 2017. China has the world's largest electric car market and nearly 580,000 electric cars were sold there in 2017, up 72% from the year before. The market is projected to grow at a compound annual growth rate (CAGR) of 32.6% to reach around 11 million units by 2025, including both the pure electric vehicles and the plug-in hybrid vehicles[1]. Under the increasing situation, the demand for battery, as the energy supplier, will accordingly rise, to accommodate the large number of electric vehicles.

However, the current battery technology does not well satisfy all the applications above. The next-generation batteries with better safety, higher energy density, faster charge/discharge rate, longer cycle life are desired.[2, 3]

In the following text, I will talk about the background and principles of batteries. Then our developments of composite solid electrolyte with flexibility for stable lithium metal battery and stabilizing the nonflammable electrolyte in the above system with LFP cathode will be discussed. Next, ALD technique is applied to stabilize the polyether-based electrolytes with high voltage cathode such as NMC for high energy density. In the last part of this thesis, an alternative kind of polymer electrolyte with mechanical strength and stable cycling for the high voltage cathode will be presented.

1.2 Lithium-ion Batteries

An electric battery is a device whose chemical reactions create a flow of current in a circuit, transforming chemical energy into electrical energy[4, 5]. It is composed of three key elements, a cathode, an anode which are the two electrodes, and a kind of electrolyte used to conduct ions

between the cathode and the anode. The battery voltage is from the difference of the electrochemical potentials of the two electrodes. When connected with the external circuit in the discharge state, reduction reaction takes place at the cathode, or the positive electrode, and oxidation reaction at the anode or the negative electrode, providing the output voltage and current for the circuit. In charge state, the reactions are reversed. Batteries are generally classified into two categories, primary and secondary batteries. Primary batteries are created for one time use and then disposed, since the reactions in the primary batteries are not reversable. Secondary batteries, or rechargeable batteries are created to be recharged and reused for multiple times. The reactions that take place in them can be reversed.

Lithium-ion batteries (LIBs) fall in the secondary batteries, and since the first LIB commercialized by Sony in 1991 with the $LiCoO_2$/graphite system, LIBs have become very important energy storage devices in portable electronics, electric vehicles and grid-level energy storage. During the almost 30 years development, extensive studies have been done to improve the performance of the electrode materials and to develop new material systems, such as nonflammable liquid electrolytes and solid-state batteries.

In LIBs, lithium ions move from cathode to anode during charge, and reversely during discharge. A commercially used LIB composed of $LiCoO_2$ cathode and graphite anode is illustrated in Figure 1.2 as an example. The green and yellow cuboids are the aluminum and copper foils as the current collectors for the $LiCoO_2$ cathode and graphite anode respectively. The cathode and anode materials are mixed with carbon additives as the conductive material and binders (e.g. polyvinylidene fluoride), to form films attached to the aluminum and copper substrates. To conduct ions between the two electrodes, an organic liquid electrolyte is needed composed of carbonate ethers (e.g. ethylene carbonate and diethyl carbonate) and a lithium salt (e.g. $LiPF_6$). A porous

polymer film (e.g. polyethylene) called separator, is also required between the electrodes to separate the cathode and anode, preventing shorting issues.

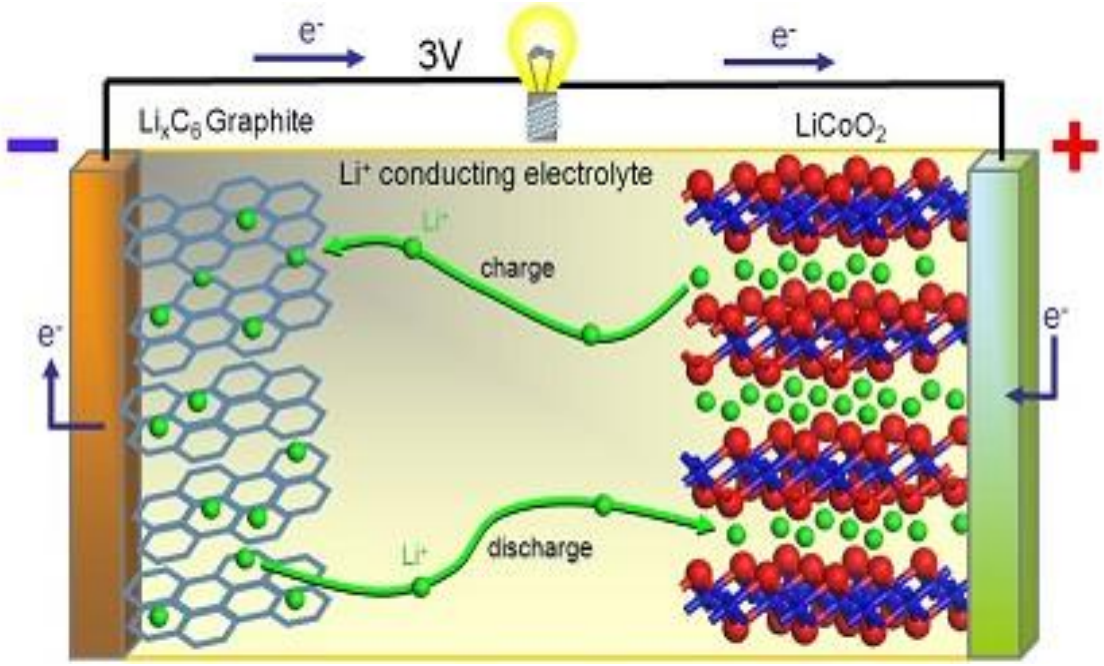

Figure 1.2. The working principle of a $LiCoO_2$/graphite battery system. Source: Johnson Matthew Battery Systems.

During charging process, the following reactions take place in the cathode and anode,

Cathode: $LiCoO_2 \rightarrow Li_{1-x}CoO_2 + x\ Li^+ + x\ e^-$,

Anode: $6\ C + Li^+ + e^- \rightarrow LiC_6$,

and the reversed reactions would happen during discharging process.

1.3 Next-generation Lithium Batteries

The current battery technology does not well satisfy all the applications. The next-generation batteries with better safety, higher energy density, faster charge/discharge rate, longer

cycle life and lower cost are desired. In the currently commercialized lithium-ion batteries, organic liquids are used as the electrolyte such as ethylene carbonate (EC) and diethyl carbonate (DEC). The issue herein is that these organic liquid electrolytes are very flammable, causing some safety concerns like EV and smartphone fires.

To achieve better safety, two approaches have attracted significant amount of attention. One is to use novel nonflammable liquid electrolytes instead of the commercially used organic ones [6, 7], another is to replace the liquid electrolytes directly with solid electrolytes which do not ignite [8-10]. These two approaches will be discussed in the following chapters.

For the energy density improvement which is one of the most important parameters in battery and directly related with the battery life and mileage in EVs, lithium metal is considered as the "Holy grail" of the next-generation batteries, as it has more than 10 times specific capacity than the commercial graphite anode (3860 vs. 372 mAh/g) and the lowest electrochemical potential (–3.04 V versus the standard hydrogen electrode). With the lithium metal anode, a Li–LMO cell (where LMO is a lithium transition-metal oxide) can deliver a specific energy of ~ 440 Wh/kg, compared with the state-of-the-art ~ 250 Wh/kg lihthium-ion batteries[11]. In lithium batteries with lithium metal as the anode, the following reaction happens in the charging process:

Cathode: $LiCoO_2 \rightarrow Li_{1-x}CoO_2 + x\ Li^+ + x\ e^-$,

Anode: $Li^+ + e^- \rightarrow Li$,

while the reversed reaction occurs during discharge. The difference with lithium-ion battery is that during the battery charge and discharge, lithium element will undergo the oxidation and reduction reactions.

Like many other metals, lithium metal tends to deposit in dendritic form[12] during battery cycling. This is the main reason for thermal runaway and fire hazards resulting from internally shorting the cells. Thus, dendrite-free lithium batteries are desired as one basic demand.

In the current LIBs, the commercial liquid electrolytes react with lithium metal, forming resistive solid state interphase (SEI) composed of solid-phase electrolyte decomposition products and resulting in low Coulombic efficiency and gradual increase of lithium metal anode overpotential. The consequence is that the battery capacity degrades over time. To prevent this and achieve a stable cycling stability with the desired lithium metal anode for the next-generation lithium batteries, lithium-stable nonflammable liquid electrolytes and solid electrolytes also serve as two important candidates.

In the following chapters, solid electrolytes are studied, designed and utilized in the solid-state rechargeable batteries.

1.4 Important Parameters

1.4.1 Battery Voltage

For a simple chemical reaction

$$A + B \rightarrow AB,$$

The driving force for the reaction results from the standard Gibbs free energy of AB and A+B,

$$\Delta G^o_{rxn} = \sum \Delta G^o_f(AB) - \sum \Delta G^o_f(A + B)$$

The electrostatic energy per mole of a species is nEF, where E is the voltage between the cathode and anode, n is the charge number of electrons involved in the reaction, F is the Faraday constant (96500 C/mol). Thus, a battery voltage can be expressed as

$$E = -\Delta G/nF,$$

The chemical potential of species i is denoted as

$$\mu_i = \partial G/\partial n_i,$$

and the integer form of this is

$$\Delta\mu_i = \Delta G = -nEF$$

The chemical potential of a species is related with its activity

$$\mu_i = \mu_i^o + RTlna_i,$$

where μ_i^o is the chemical potential of species i in the standard state, a_i is the activity of species i, R is the ideal gas constant (8.31 J/mol), and T is the temperature. The activity is the effective concentration. If the activity is equal to 1, it behaves like the pure species.

In LIBs, the potential is always compared with the redox couple Li/Li^+, which is -3.04 V vs. the standard hydrogen electrode. The potentials of several commonly used cathode and anode materials are listed below:

Cathodes: $Li(Ni_{1/3}Mn_{1/3}Co_{1/3})O_2$: 3.7 V, $LiCoO_2$: 3.8-4.3 V, $LiFePO_4$: 3.4 V

Anodes: Graphite : 0 - 0.25 V, $Li_4Ti_5O_{12}$: 1.55 V

In a battery, the voltage profile is demonstrated vs. the capacity. To understand the voltage profile across the battery with the state of charge, the Gibbs Phase Rule can be applied. The Gibbs Phase Rule is expressed as

$$F = C - P + 2,$$

where F is the number of degrees of freedom, C is the number of elements, and P is the number of phases in the system. The voltage is one of the intensive thermodynamic parameters that can describe the system, falling in the freedom range.

As an illustration, the Li/I_2 cell has iodine and lithium as the cathode and anode respectively, and for the reaction at I_2 electrode,

$$2Li^+ + I_2 + 2\,e^- \rightarrow 2LiI$$

Lithium and iodine two elements exist in this system. Thus C is 2. Here, the reaction for lithium ion and iodine will generate a new phase of LiI, so there are two phases in this reaction. Based on the Gibbs Phase Rule, the freedom F is equal to 2. However, in an electrochemical reaction, temperature and pressure need to be specified, meaning no other freedom is allowed in this system. In this case, the voltage does not change with the concentration of Li, or state of the charge, as shown in Figure 1.3. This is a two-phase reaction.

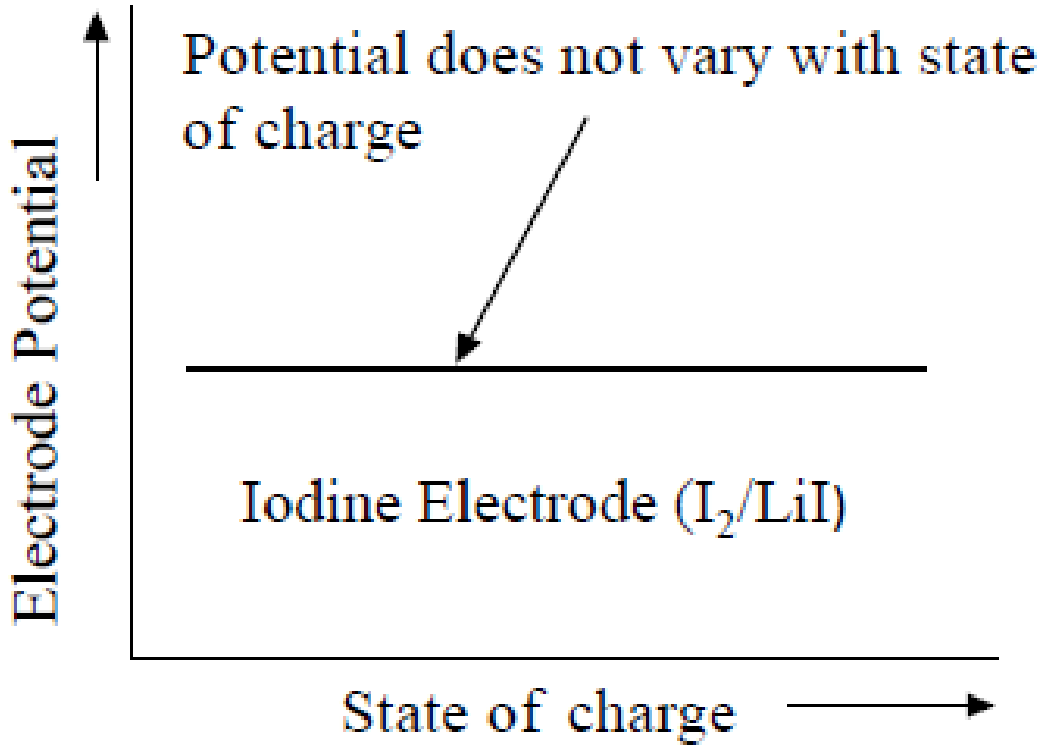

Figure 1.3. Potential vs. state of charge for a two-phase reaction. Figure adapted from ref. 5.

As another example, the Li/TiS_2 cell has TiS_2 and lithium as the cathode and anode respectively, and for the reaction at TiS_2 electrode,

$$\delta Li^+ + Li_xTiS_2 + \delta e^- \rightarrow Li_{x+\delta}TiS_2$$

There are three elements exist in this system. Thus C is 3. Here, lithium ions are inserting into the Li_xTiS_2 materials forming one solid solution, so the reaction has only one Li_xTiS_2 phase. Based on the Gibbs Phase Rule, the freedom F is equal to 4. Other than temperature and pressure, there are two more parameters needed. Voltage is one of the two, indicating voltage is changing with the state of the charge, as shown in Figure 1.4. This is a single-phase reaction.

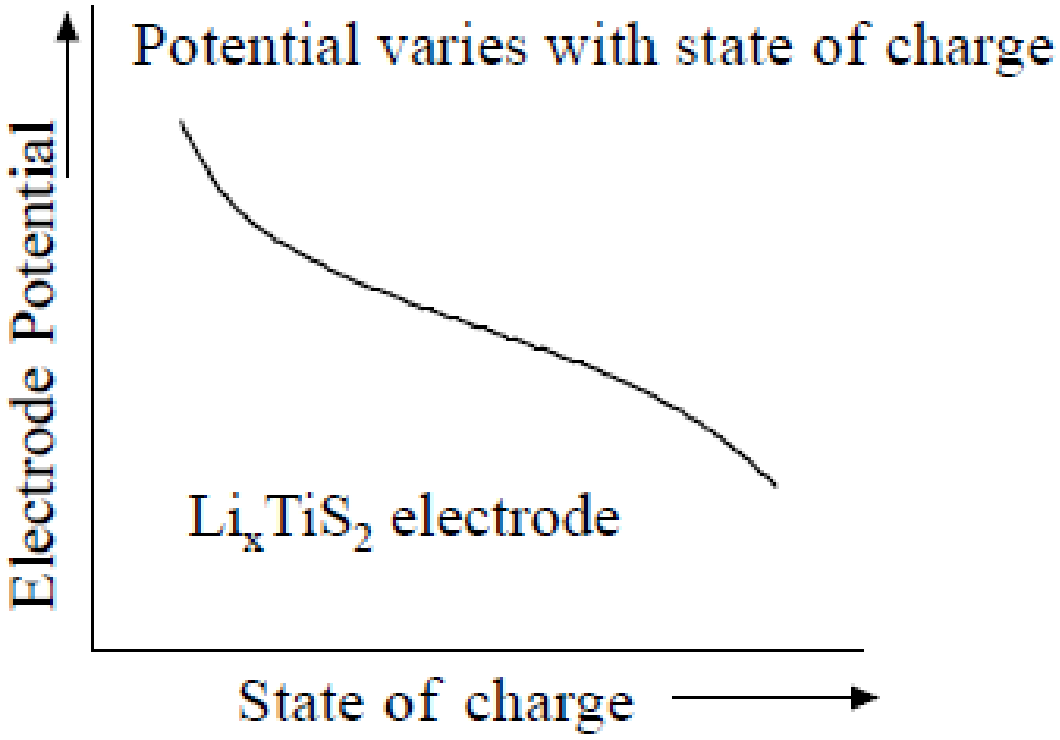

Figure 1.4. Potential vs. state of charge for a single-phase reaction. Figure adapted from ref. 5.

1.4.2 Capacity

Capacity describes the amount of charge that a material can store. In battery, capacity is associated with each electrode material. The specific capacity of a material is expressed as

$$\text{Specific Capacity } \left(\frac{\text{mAh}}{\text{g}}\right) = \frac{Charge\ stored\ per\ mole\ of\ material\ \left(\frac{mAh}{mol}\right)}{Molecular\ weight\ \left(\frac{g}{mol}\right)}$$

$$\text{C } \left(\frac{\text{mAh}}{\text{g}}\right) = \frac{nF\ \left(\frac{C}{mol}\right)}{M_w\ \left(\frac{g}{mol}\right)} = \frac{1000nF\ \left(\frac{mAh}{mol}\right)}{3600M_w\ \left(\frac{g}{mol}\right)}$$

where C is the specific capacity, n is the mole number of electrons transferred in a reaction, F is the Faraday constant (96500 C/mol), M_w is the molecular weight of a material.

For a battery with a cathode and an anode, the effective capacity is

$$\mathrm{C} = \frac{C_+ C_-}{C_+ + C_-}$$

where C_+ and C_- are the cathode and anode specific capacity respectively.

1.4.3 Coulombic Efficiency

The Coulombic efficiency (CE) is the ratio of discharge capacity and charge capacity. CE indicates the reversibility of the battery charging/discharging process, meaning the lithiation/delithiation abilities.

$$\mathrm{CE} = \frac{Discharge\ capacity}{Charge\ capacity}$$

1.4.4 Energy Density

Energy density is the amount of energy stored in a battery per weight or per volume. The total energy stored in a battery has the form

$$E = \int V dC$$

where V is the voltage in the voltage profile and C is the corresponding capacity.

The energy over the total weight of a battery is the gravimetric energy density, and the energy over the total volume is the volumetric energy density. The gravimetric energy density has the unit of Wh/kg, and the volumetric energy density unit is Wh/L. In theoretical energy density, only the specific capacities and weights of cathode and anode are considered. The practical energy

density in the battery should contain the weights of inactive materials in cathode and anode (conductive additives and binders), electrolyte, separator, and current collectors.

Energy density is one of the most important parameters to demonstrate the performance of a battery.

1.4.5 C-rate

The power generated from a battery is the voltage times the current. With a high current for charging or discharging, there will be a high voltage loss due to the internal resistance (IR loss), polarization, solid-state diffusion and phase transformation. For this reason, batteries are tested at different currents, or C-rates. The discharge rate of a battery is expressed as C/n, where n is the number of hours needed to fully discharge the battery's nominal capacity. For example, C/10 current indicates that the current will fully discharge the battery in 10 hours, 5C means the current will discharge the battery in 12 minutes. Typically, commercial lithium ion battery can be operated up to 1 - 2C, and certain high-power lithium ion batteries could reach 5 - 10C. With different materials, the C-rate capabilities are different.

1.4.6 Cycle Life

The battery cycle life is another important parameter to evaluate a battery. It is defined as the cycle number (a charge/discharge cycle is one cycle) of cycles when the capacity of the battery drops down to 80% of its initial capacity.

1.4.7 Retention

The battery capacity retention is defined as the fraction of the remaining capacity after a period of cycling or storage under certain discharge conditions.

Chapter 2: Characterization Techniques

2.1 Electron Microscopies

Electron microscopies are used to characterize the morphology of materials. A scanning electron microscope (SEM) is an important electron microscope that can generate images of a material with a focused beam around 0.4 – 5 nm of electrons. The electrons are interacting with the atoms in the target material and scattered, including elastic, inelastic scatterings for secondary electrons, and emission of radiations, to provide the morphology and composition information of the target material. SEM can reach a resolution less than 1 nm. SEM images in this thesis are generated with a ZEISS SIGMA VP SEM in Columbia Nano Initiative (CNI) at Columbia University, as shown in figure 2.1 below.

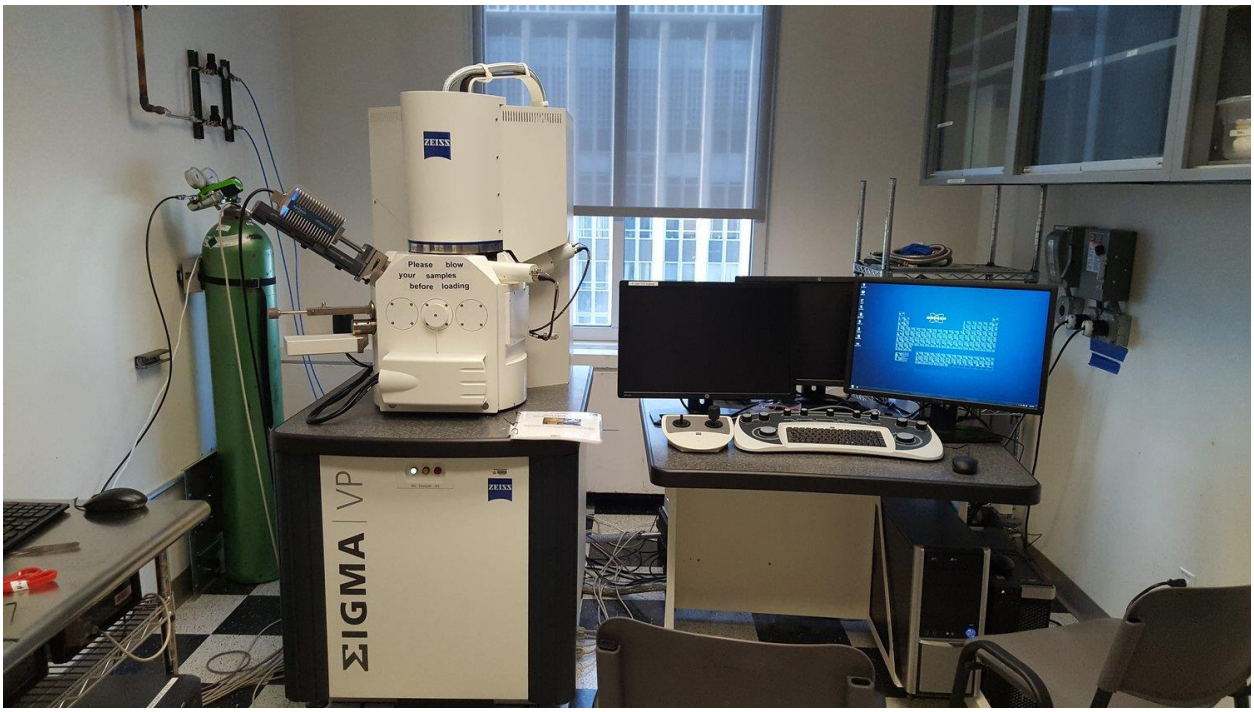

Figure 2.1. ZEISS SIGMA VP SEM at Columbia University.

A transmission electron microscope (TEM) is another important microscope that a beam of electrons is transmitted through a thin target material less than 100 – 200 nm. The images or diffraction patterns are generated from the interaction of the electrons with the sample. TEM has a much higher resolution than other microscopes due to the smaller de Broglie wavelength of electrons. TEM images in this thesis are generated with a FEI TALOS F200X S-TEM in Columbia Nano Initiative (CNI) at Columbia University (Figure 2.2).

FEI Talos
F200X

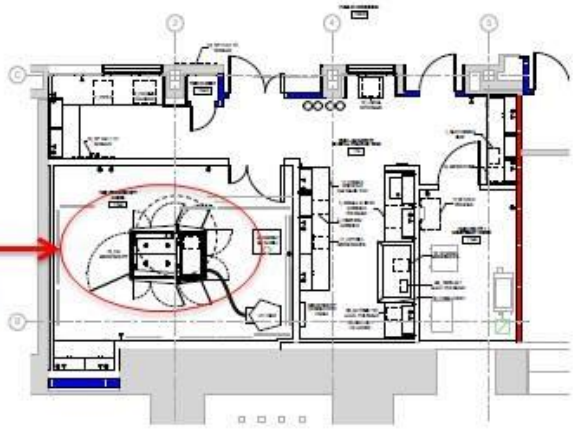

Havemeyer 100 Level

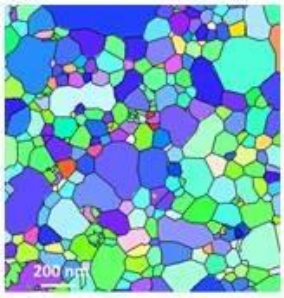

Crystal Orientation Map

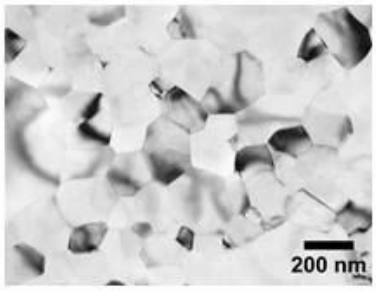

Bright-field image

Figure 2.2. FEI TALOS F200X S-TEM at Columbia University.

When the electrons are interacting with the atoms in the samples, radiations such as X-ray will be generated in both SEM and TEM. The X-ray radiation can be used for the elemental analysis or chemical characterization, which is called the energy dispersive X-ray spectroscopy (EDS). In the interaction, the electron beam kicks out electrons in the inner shell of the atoms in the sample, followed by the electrons falling to empty inner shells from the outer shells. The excessive energy of electrons distinct for different elements is released as X-ray, and can be collected by the EDS detector, providing elemental and compositional information. The EDS detectors are embedded within the SEM and TEM instruments.

2.2 X-ray Diffraction

X-ray diffraction (XRD) is an important non-destructive tool to analyze the crystalline phases of materials. The Bragg equation

$$n\lambda = 2d \sin\theta$$

is the key to understand XRD. Here n is an integer, λ is the wavelength of the X-ray, d is the interplanar spacing between atoms, and θ is the angle of the incident X-ray beam with respect to the plane. Knowing the wavelength and the incident angle, the spacings and then the crystal structure in the sample can be determined. The XRD data in this thesis is generated from PANALYTICAL XPERT3 POWDER XRD in Columbia Nano Initiative (CNI) at Columbia University (Figure 2.3).

Figure 2.3. PANALYTICAL XPERT3 POWDER XRD at Columbia University.

2.3 X-ray Photoelectron Spectroscopy

X-ray photoelectron spectroscopy (XPS) is a surface-sensitive technique that can be applied to a broad range of elements, providing quantitative and chemical state information. A beam of X-ray is irradiating on the sample which causes photoelectrons to be emitted from the sample surface. By measuring the energy of the emitted electrons with the energy analyzer, the binding energy and intensity can be obtained to present the elemental and chemical state information. The XPS data in this thesis is generated from PHI 5500 XPS in Columbia Nano Initiative (CNI) at Columbia University (Figure 2.4).

Figure 2.4. PHI 5500 XPS at Columbia University.

2.4 Thermogravimetric Analysis

Thermogravimetric analysis (TGA) is a technique for thermal analysis. TGA measures the amount of weight change of the sample as a function of elevated temperature or time isothermally, under a certain atmosphere. The TGA result provides the information about the phase transitions, absorption, desorption, decompositions and other reactions. The TGA data in this thesis is generated from Q500 TGA in Columbia Nano Initiative (CNI) at Columbia University (Figure 2.5).

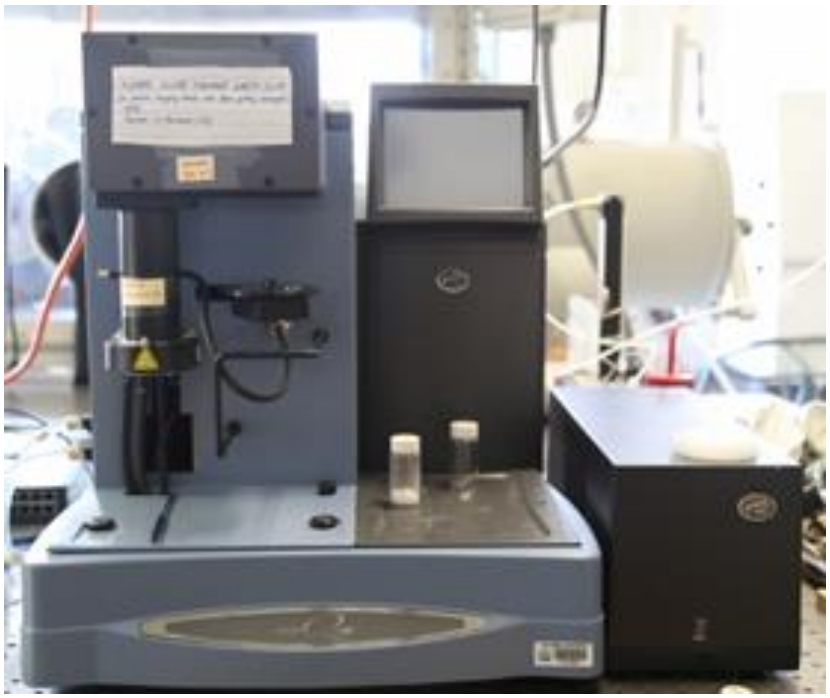

Figure 2.5. Q500 TGA at Columbia University.

2.5 Electrochemical Characterizations

2.5.1 Cyclic Voltammetry

Cyclic voltammetry (CV) is a potentiodynamic electrochemical measurement that can provide qualitative analysis of electrochemical reactions. In a CV experiment, the working electrode potential is scanned linearly vs. time, at a certain rate, typically between one hundredth millivolt to tens of millivolt per second. The CV is always plotted as current vs. voltage. When there is a peak spike for current, it indicates a reaction at that voltage. The cathodic peak exists at a lower potential and the anodic peak shows up at a higher potential.

2.5.2 Electrochemical Impedance Spectroscopy

Electrochemical impedance spectroscopy (EIS) is useful technique to detect the impedance by applying a sinusoidal voltage perturbation to the system, in the frequency domain. Small

alternating current (AC) signals with different frequencies exist with the voltage amplitudes ranging from 5 – 20 mV.

The EIS measurement can be modeled with an equivalent circuit, and the results are always demonstrated in a Nyquist plot. In a Nyquist plot, the y-axis represents the negative of the imaginary part of the impedance, and the x-axis represents the real part. The impedance of a common resistor only contains a real resistance which is in phase with the AC voltage, and it occupies a dot on the x-axis in the Nyquist plot, as shown in Figure 2.6a. The impedance of a capacitance is out of phase with the AC signal and is called the reactance which is pure imaginary with the form

$$Z_{im} = -\frac{i}{\omega C}$$

where i is the imaginary unit, ω is the angular frequency of the AC signal, and C is the capacitance. In a Nyquist plot, the capacitance is a line overlapping with the y-axis, and the dots on the line are originating from the alternating frequencies (Figure 2.6b). If a resistance and a capacitance are in series, as shown in Figure 2.6c, the Nyquist plot would have a line vertical to the x-axis, with the intersection as the resistance value. If a resistance is in parallel with a capacitance, there will be a semicircle in the Nyquist plot in Figure 2.6d. The right intersecting point with the x-axis represents the resistance value.

In lithium-ion batteries, when the lithium ions insert into the cathode or anode materials, there will be resistances from the electrolyte, a double-layer capacitance, a charge transfer resistance at the electrolyte-electrode interface, and the diffusion process inside the material. The equivalent circuit is illustrated in Figure 2.6e. The resistance Rs is composed of electronic resistance in the system and the ionic resistance of the electrolyte. The lithium ions moving through the electrolyte-electrode interface, which is called the charge transfer process, can be represented

by a charge transfer resistance Rct and a capacitance in parallel. This capacitance is resulted from the double layer capacitance of the electrolyte-electrode interface. The diffusion process of lithium ions inside the solid phase is described as the Warburg element (straight line with 45°), with the expression

$$Z = A\omega^{-1/2} - iA\omega^{-1/2}.$$

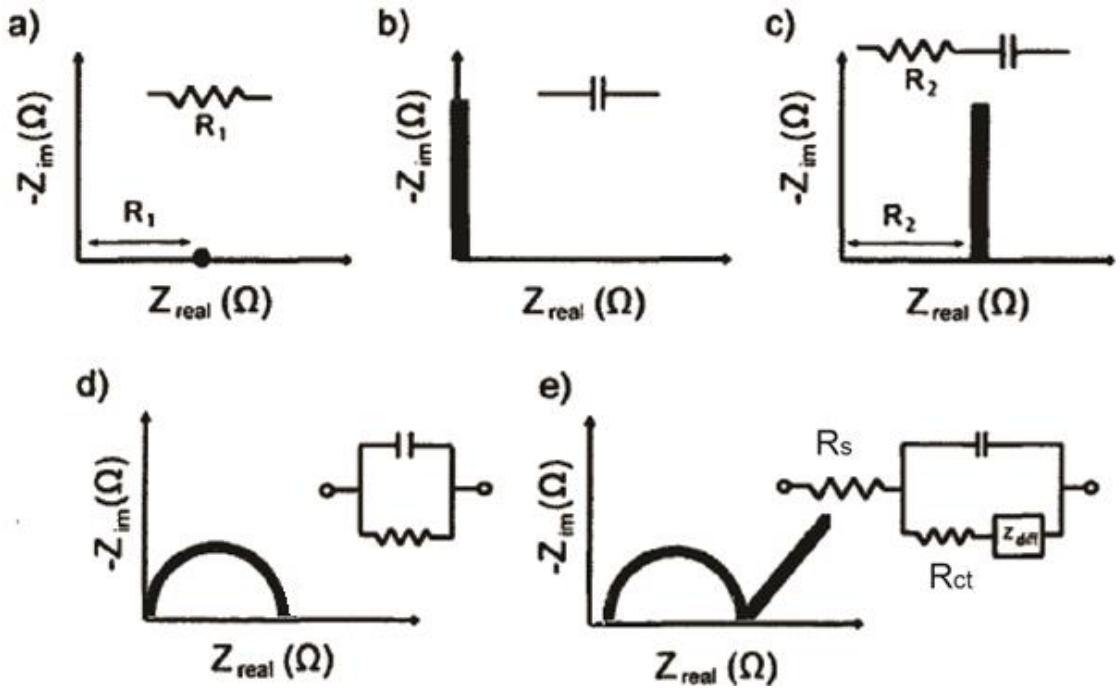

Figure 2.6. Schematics of basic circuit elements and corresponding Nyquist plots. (a) Resistance, (b) capacitance, (c) resistance and capacitance in series, (d) resistance and capacitance in parallel, (e) resistance and capacitance in parallel with diffusion into the electrode. Figure adapted from the thesis of Candace Chan at Stanford University.

Chapter 3: Flexible Composite Solid Electrolyte Composed of Ceramics and Polymer

3.1 Introduction to Solid Electrolyte

Lithium-based rechargeable batteries are important energy storage devices for portable electronics, electric vehicles and grid-level energy storage[4, 13]. High energy density, high safety and low-cost are the essential factors for developing next-generation lithium batteries. State-of-the-art Li-ion batteries (LIBs) use organic liquid-based electrolytes, which readily conduct ions and have a reasonably large stability window of ~ 4 V, leading to both high power and high energy densities[4, 13, 14]. However, the organic liquid electrolytes have several drawbacks, such as high flammability, side reactions with both anode and cathode, electrolyte decomposition at high temperatures, potential leakage, and toxicity[14-16]. Solid electrolytes are attractive compared to liquid organic electrolytes, as they are much less flammable, and less reactive with electrode materials[17-20]. Moreover, they can also suppress the growth of dendrites in lithium anode, which has a specific capacity ten times that of graphite anode, and the most negative electrode potential (-3.04 V vs. standard hydrogen electrode). Therefore, successful development of solid electrolytes could potentially lead to rechargeable batteries with high safety, high energy density and low cost.

Solid polymer electrolytes and inorganic ceramic electrolytes are most widely studied among solid electrolytes. Solid polymer electrolytes typically use polyethylene oxide (PEO) as the matrix with lithium salts (e.g. $LiClO_4$) filled inside[4, 21, 22], while ceramic electrolytes are commonly based on oxides[23, 24] and sulfides[25, 26]. High ionic conductivities of 10^{-4} - 10^{-2} S/cm have been observed in various ceramic electrolytes, such as NaSICON-type $Li_{1+x}Al_xTi_{2-x}(PO_4)_3$ (LATP)[27-29], $Li_{1.5}Al_{0.5}Ge_{1.5}(PO_4)_3$ (LAGP)[30, 31], garnet-type $Li_7La_3Zr_2O_{12}$ (LLZO)[23, 32,

33] and sulfides[25, 26]. However, ceramics are typically rigid, difficult to process, and exhibit high interfacial resistance with electrode materials[34, 35]. In contrast, solid polymer electrolytes can be prepared by simple solution-based processes, but they typically have low ionic conductivities (<10^{-5} S/cm at room temperature)[22, 36, 37].

3.2 Flexible Solid Electrolyte with Vertically Aligned Structure

In order to combine the advantages of both types of electrolytes, composite electrolytes have been developed where ceramic particles are dispersed in a polymer electrolyte matrix (Figure 3.1a)[8]. As demonstrated in previous work, the fillers could be either non-Li^+ conducting, such as Al_2O_3[38], SiO_2[22], TiO_2[39] and ZrO_2[40], or Li^+ conducting, such as $Li_{0.5}La_{0.5}TiO_3$ (LLTO)[41], LLZO[42] and LATP[43, 44]. For non-conducting fillers, ionic conductivities in the order of 10^{-5} S/cm can be achieved and the mechanism is considered to be the amorphorization of PEO and the creation of space-charge regions to facilitate Li^+ transport[22, 45]. For ion-conducting fillers, ionic conductivity in the order of 10^{-4} S/cm has been reported[8]. However, the arrangement of fillers is either uniform dispersion[22] or fibers nearly in parallel to the surface of the solid electrolyte membrane[8]. For uniform dispersions, ion transport is significantly obstructed by the PEO matrix with a low conductivity, and conductivities even lower than the polymer matrix itself may be observed[45]. For fibers, a significant portion of ceramic does not contribute to ion conduction as they are aligned in parallel to the electrolyte surface. To maximize ionic conductivity of the composite electrolyte, it is ideal to have vertically aligned and connected ceramic conductors which is also predicted in a recent review article[11], as shown in Figure 3.1b. Here we present an ice-templating-based method to fabricate such structures in a composite electrolyte, where vertically aligned ion-conductive ceramic fillers form fast pathways for Li^+ transport, while the

polymer matrix provides flexibility and mechanical support of the composite. In this work, LATP filler in PEO is used as an example. The composite electrolyte reaches an ionic conductivity of 0.52×10^{-4} S/cm, which is close to the theoretical value based on the conductivity and volume portion of LATP (0.45×10^{-4} S/cm). The conductivity is largely limited by that of the ceramic phase, but this method can be extended to other ceramic systems, such as LLZO and even sulfides, to further enhance the ionic conductivity.

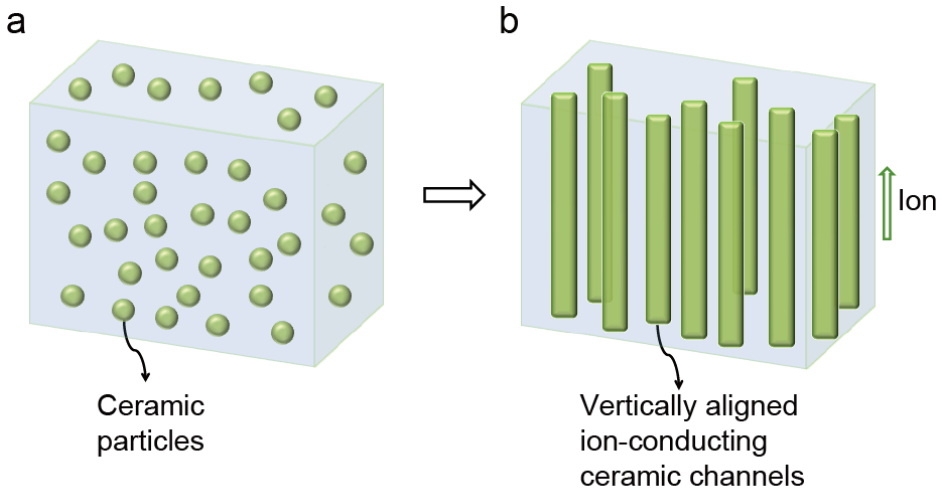

Figure 3.1. The schematic of vertically aligned and connected ceramic channels for enhancing ionic conduction. (a) Ceramic particles are randomly dispersed in the polymer matrix, where ion transport is blocked by the polymer matrix with a low conductivity. (b) Vertically aligned and connected structure to facilitate ion transport, which can be realized by the ice-templating method.

Figure 3.3a illustrates the principle of the ice-templating process, which has been developed in the past decade to form vertical structures for thermal insulation, battery electrodes and other functional materials[46-53]. In our experiments, the LATP nanoparticles (NPs) are dispersed in water and cast onto a substrate (step 1), after which the bottom end is slowly cooled.

Therefore, a vertical temperature gradient forms and ice nucleates from the bottom of the suspension, pushing the ceramic particles together to form vertically aligned structures (step 2). After ice sublimation, LATP particles are sintered together to form vertically aligned, straight channels for fast ionic transport (step 3 and 4). Lastly PEO/$LiClO_4$ polymer electrolyte is filled into the porous ceramic structure to provide mechanical strength and flexibility (step 5).

To realize such a composite electrolyte with a rationally designed structure, LATP NPs with high ionic conductivity are needed. Such NPs are synthesized by a co-precipitation process[54]. An 8 mL aqueous solution of 0.185 g lithium acetate dihydrate ($CH_3CO_2Li•2H_2O$, 99%; Alfa Aesar) and 0.418 g ammonium phosphate monobasic ($NH_4H_2PO_4$, 98.5%; Sigma Aldrich), and a 2 mL ethanol solution containing 0.136 g aluminum nitrate non-anhydrate ($Al(NO_3)_3•9H_2O$, 98%; Alfa Aesar) and 0.701 g titanium butoxide (97%, Sigma Aldrich) are mixed together, and a white precipitation is formed immediately. Then the precipitation is collected and heated at 850 ^oC for 2.5 hours. The X-ray diffraction (XRD) of the as-sintered LATP powders show mainly the LATP pattern[54, 55] (Figure 3.2b). To measure the ionic conductivity, the LATP particles are pressed into pellets at 240 MPa and sintered at 1000 ^oC for 10 hours. After annealing, the pellet shows almost the same phase as powders (Figure 3.2b). Figure 3.2a and inset are the SEM image of the as-synthesized LATP powders, with an average size of 200-500 nm and the camera image of the pellet. EIS measurement (Figure 3.2c) shows that the conductivity reaches 1.0×10^{-4} S/cm at room temperature, comparable to the reported values[8, 54, 56].

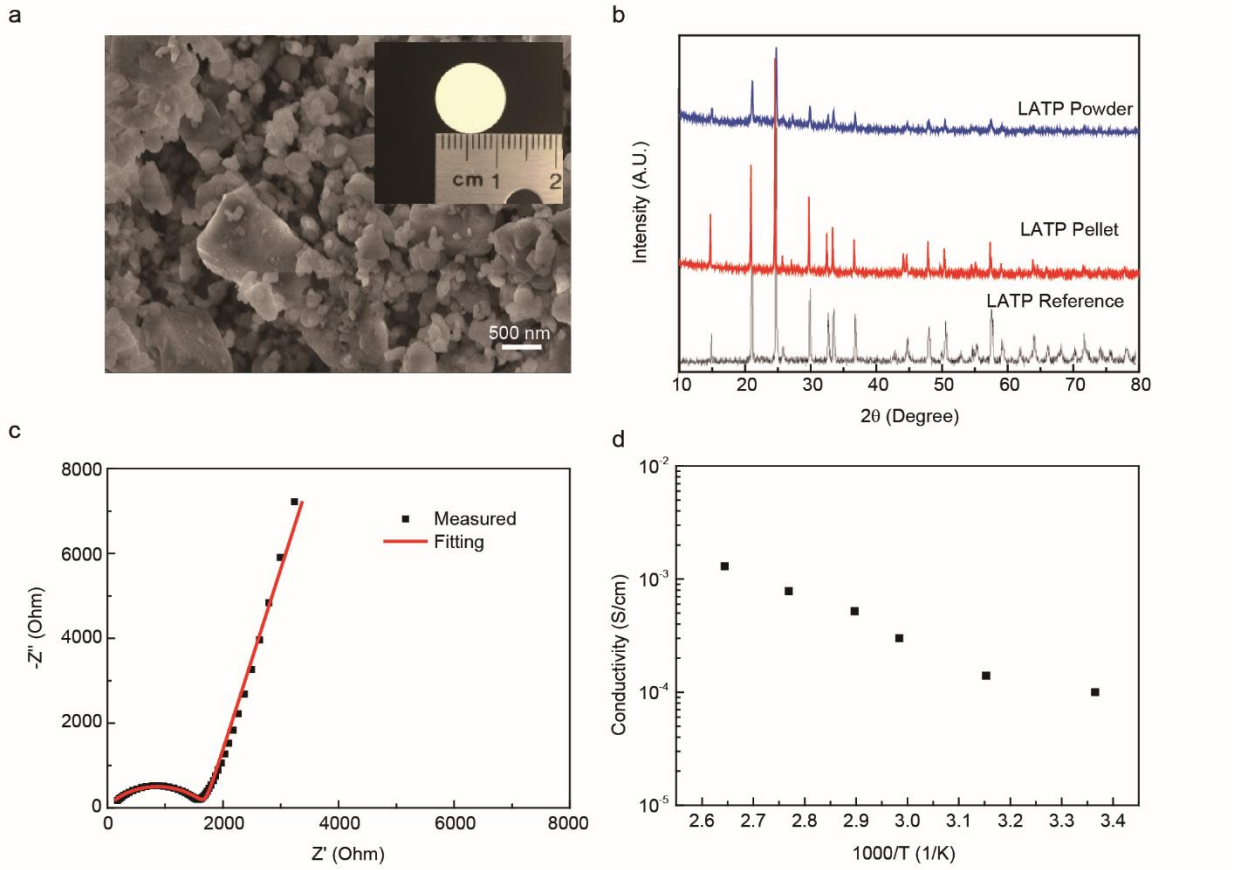

Figure 3.2. Characterizations of as-synthesized LATP. (a) SEM image of as-synthesized LATP powders. Inset is the camera image of the LATP pellet. (b) XRD of as-synthesized LATP powders. (c) Impedance measurement of the LATP pellet at room temperature. (d) Temperature–dependent ionic conductivity of the pellet.

After synthesizing LATP NPs with a high conductivity, they are dispersed in de-ionized (DI) water to form a suspension. Polyvinyl alcohol (PVA) and polyethylene glycol (PEG, MW=400) are added as binder and plasticizer, respectively. Then the suspension is dropped onto an Al_2O_3 plate, which is cooled afterwards from the bottom by a thermoelectric plate with a cooling rate of 3 ^{o}C/min. After the water is fully frozen, a vacuum is applied to sublime ice and the

vertically aligned structure of LATP particles are revealed. Figure 3.3b and c are SEM images of the top and cross-section views of the vertically aligned ice-templated LATP structure before sintering, respectively. Clearly, straight pores are formed over a large area with typical pore sizes of 5-10 um. After sintering, the vertically aligned porous structure still remains, and particles are better sintered together, providing the direct pathways for lithium ions transport (Figure 3.3d and e). From SEM images, the typical film thickness is measured to be ~ 100 μm, and can be further reduced by lowering the thickness of the initial suspension coating. After sintering the LATP NPs and adding the PEO polymer electrolyte, the LATP porous structure is fully covered by PEO/$LiClO_4$ (Figure 3.3f). The composite electrolyte is also flexible and can be easily bent (Figure 3.3g).

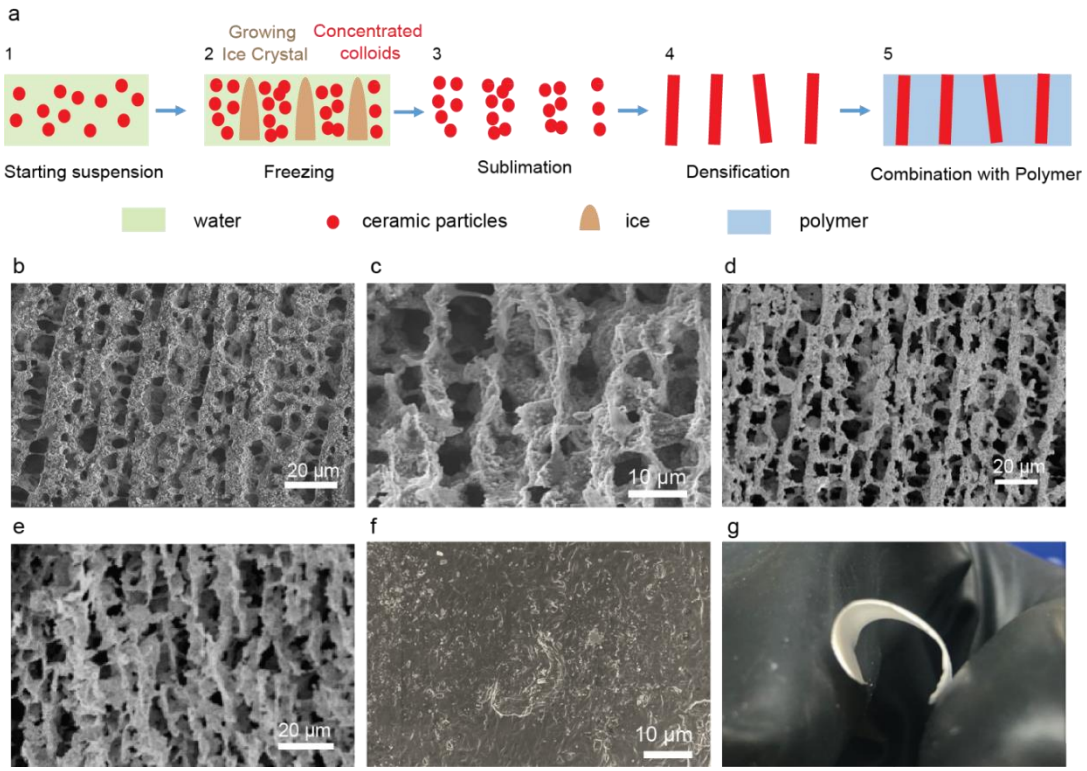

Figure 3.3. The ice-templating process and the as-fabricated composite electrolyte. (a) 1. Starting suspension with ceramic particles dispersed in water. 2. Unidirectional freezing through cooling from the bottom. 3. Sublimation of ice in a vacuum. 4. Densification of ceramics through sintering. 5. Combination

with the polymer electrolyte matrix to form the composite electrolyte. (b-e) SEM images of the ice-templated LATP channels. (b) Top view before sintering, (c) Cross-section view before sintering, (d) Top view after sintering, and (e) Cross-section view after sintering. (f) SEM image (top view) of the aligned structure after filling the PEO/$LiClO_4$ electrolyte. (g) Camera image showing the flexibility of the composite film.

3.3 Thermal and Mechanical Stability

Thermogravimetric analysis (TGA) is used to understand the thermal stability of the composite electrolyte. The electrolyte is heated in O_2 with a heating rate of 10 °C/min. Both the pure PEO/PEG and PEO/PEG/ice-templated LATP composite samples are tested. The pure PEO/PEG electrolyte is thermally stable at up to temperatures of around 145 °C, whereas the ice-templated composite is stable up to around 167 °C, indicating that LATP helps improve the thermal stability of the composite electrolyte. Above this temperature, polymers begin to decompose and most mass is lost before 400 °C. For the ice-templated composite electrolyte, the weight loss occurs in the similar temperature range, and the mass left is from LATP NPs inside the composite electrolyte. The ice-templated LATP fillers also stabilize the structure of the composite solid electrolyte. In Figure 3.4b, without any ice-templated structure, the PEO/PEG electrolyte melts and shrinks after heating at 180 ^oC for 30 min since there is no rigid ceramic backbone inside. In contrast, the electrolyte with ice-templated LATP NPs is intact at 180 ^oC, showing that the ceramic fillers can effectively stabilize the integrity of the structure.

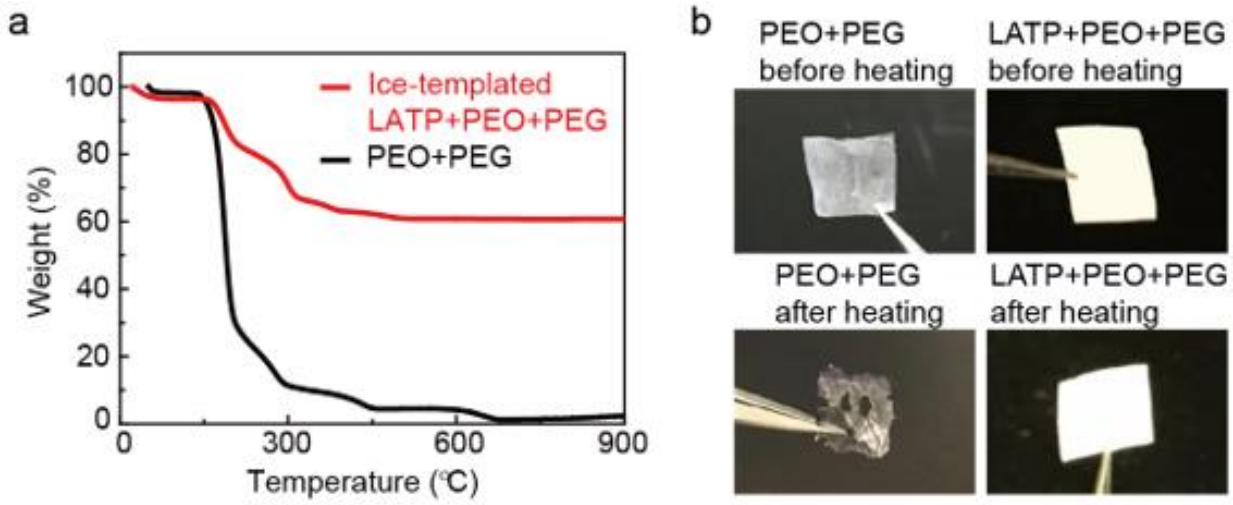

Figure 3.4. Thermal properties of the composite electrolyte. (a) TGA curves of the PEO/PEG and PEO/PEG/ice-templated LATP electrolytes. The heating rate is 10 °C/min in O_2 environment. (b) PEO/PEG and PEO/PEG/ice-templated LATP electrolytes before and after heating at 180 °C for 30 min.

To evaluate the flexibility of the composite electrolyte, the ice-templated LATP/PEO/PEG composite film is bent for various times, followed by measurement of ionic conductivity (Figure 3.5a). The film is first bent down to diameter of 5 cm up to 100 times. After an initial drop, the conductivity becomes stable after bending for 5 times. After 100 times bending, the conductivity remains at 82% of the initial value. The composite film is also bent down to diameter of 2.5 cm for various times. After 100 times, the conductivity remains at 74% of that before bending. The data supports that as-prepared composite film with vertical structure is mechanically flexible.

The modulus of the composite electrolyte is also studied. Standard stress/strain curves are measured for both tension and compression. The tensile tests are conducted along the in-plane direction with a Model 5948 MicroTester Instron instrument, and the film shows the standard linear strain-stress curve at low strains (Figure 3.5b), which is used to calculate Young's modulus. For the compressive tests, multiple pieces of composite electrolyte film are first compressed at 500

MPa to form a pellet. Then the pellet is compressed by the same MicroTester above. Non-linear behavior is observed in compression. The initial low modulus region is likely due to the stacking of multiple pieces. Therefore, the compression modulus is measured based on the linear regimes at larger strain (0.35 to 0.55 for PEO/PEG and 0.40 to 0.53 for PEO/PEG/ice-templated LATP). For PEO/PEG samples, moduli are 1.9 MPa and 1.4 MPa for tension and compression, respectively. For PEO/PEG/ice-templated LATP films, moduli are 6.6 MPa and 3.6 MPa for tension and compression, respectively. Obviously, the incorporation of LATP ceramic particles enhances the Young's modulus of the solid electrolyte. The measured values are consistent with various previous reports on polymer electrolytes[57, 58]. The work by Khurana et al shows that even lower modulus is capable of suppressing dendrite growth[59].

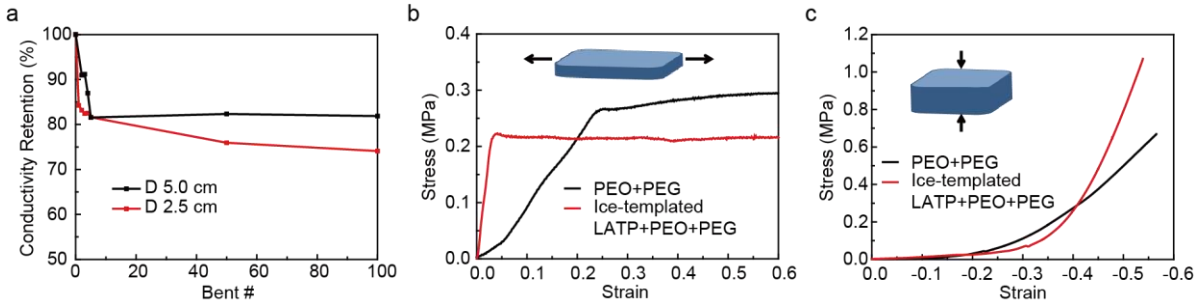

Figure 3.5. Mechanical properties of as-prepared composite electrolyte. (a) Ionic Conductivity vs. bending times. After an initial drop, the PEO/PEG/ice-templated LATP film shows stable ionic conductivities. (b) Tensile stress/strain curves for PEO/PEG and PEO/PEG/ice-templated LATP samples. Inset is the schematic of the in-plane tensile test. (c) Compressive stress/strain curves for PEO/PEG and PEO/PEG/ice-templated LATP samples. Inset is the schematic of the compressive test along z direction.

3.4 Electrochemical Characterizations

To validate our assumption that the vertically aligned and connected channels could enhance the ionic conductivity of the composite electrolyte, electrochemical impedance

spectroscopy (EIS) measurements of three types of samples at different temperatures are taken: a pure PEO electrolyte, PEO with randomly dispersed LATP NPs, and PEO with ice-templated LATP NPs (Figure 3.6a). In all samples, the molar ratio of ethylene oxide (EO) to $LiClO_4$ is fixed at 8:1. The volume percentages of the LATP NPs in the two composite electrolytes are both 40% based on the thermogravimetric analysis. Since the surface of ice-templated LATP NPs + polymer composite is rough, it is difficult to get accurate EIS results with either stainless steel or sputtered Au electrode. Therefore, lithium metal foils are used as electrodes for EIS measurement in all samples; and thus two semicircles are observed, which correspond to the resistance of bulk electrolyte and the geometric capacitance in parallel (high frequencies), and the charge transfer resistance and the double layer capacitance in parallel (low frequencies), respectively. In order to extract the electrolyte conductivity, an equivalent circuit shown in Figure 3.6a is used to fit the two semicircles in the plot, and the fitting results are illustrated as red curves. The conductivity of pure PEO electrolyte is only 3.6×10^{-8} S/cm at room temperature (See Table 3.1 for conductivities at room temperature), and it increases to 7.0×10^{-5} S/cm at 70 ^{o}C, which is consistent with previous reports[22, 60]. After adding the randomly dispersed LATP NPs, the conductivity increases to 1.4×10^{-6} S/cm at room temperature. The increased conductivity is quite small compared to the conductivity of LATP itself (~ 1.0×10^{-4} S/cm), as the LATP NPs are not connected and the conduction of Li^{+} ions is limited by the low conductivity of the matrix. The ionic conductivity of the ice-templated LATP film reaches 6.8×10^{-6} S/cm at room temperature, five times that of the randomly dispersed case. This shows that this design of vertically aligned and connected LATP fillers indeed improves the conductivity significantly.

In order to understand the relation between EIS measured by stainless steel electrodes and lithium metal electrodes, EIS of the pure PEO electrolyte and the pure PEO/PEG electrolyte are

measured with both stainless steel (SS) and lithium metal electrodes. When Li metal is used, there are two semi-circles in the EIS, with the first corresponding to the resistance of the polymer electrolyte and the geometric capacitance in parallel, and the second corresponding to the charge transfer resistance and the double layer capacitance in parallel. The stainless steels act as blocking electrodes, so only one semi-circle shows up. From results shown in Figure 3.7, for PEO/PEG, the conductivities are 7.7×10^{-6} and 1.2×10^{-5} S/cm for Li and SS electrodes, respectively; for PEO, the conductivities are 3.6×10^{-8} and 5.6×10^{-8} S/cm for Li and SS electrodes, respectively. The conductivities are consistent between Li electrodes and SS electrodes for both PEO and PEO/PEG electrolytes in Figure 3.7. The results also suggest that the conductivities represented in our paper may be underestimated, since the lithium metal electrodes give lower conductivities than SS electrodes.

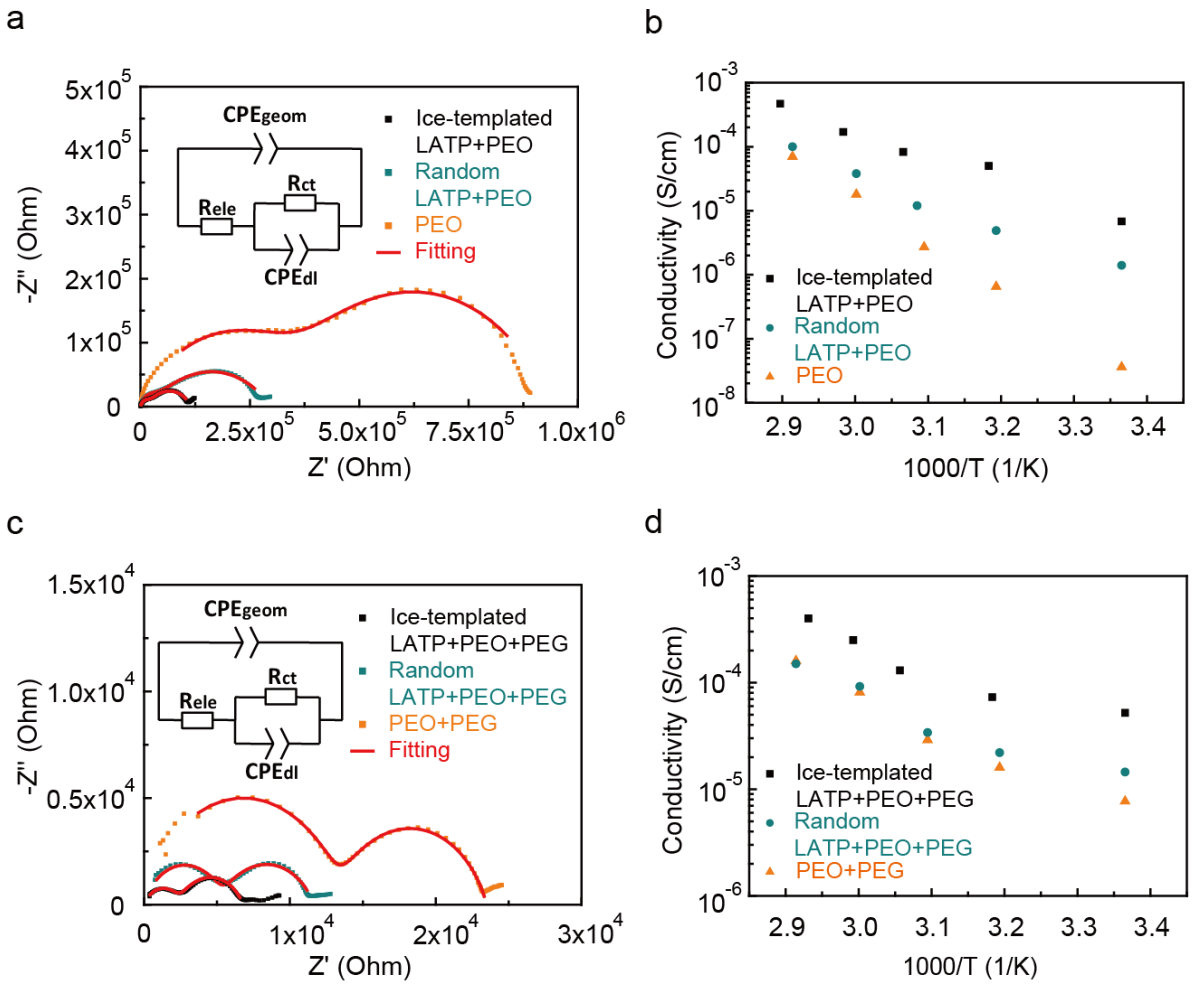

Figure 3.6. EIS measurements of the composite electrolyte. (a) EIS at room temperature for the pure PEO, PEO/randomly dispersed LATP NPs, and PEO/ice-templated LATP NPs electrolytes. Inset is the corresponding equivalent circuit. (b) Ionic conductivities of the three structures in (a) at different temperatures. (c) EIS at room temperature for the pure PEO/PEG, PEO/PEG/randomly dispersed LATP NPs, and PEO/PEG/ice-templated LATP NPs electrolytes. Inset is the equivalent circuit. (d) Ionic conductivities of the three structures in (c) at different temperatures. In (a) and (c), R_{ct} and CPE_{dl} represent the charge transfer resistance and the double layer capacitance; R_{ele} and CPE_{geom} indicate the resistance of the electrolyte and the geometric capacitance.

Table 3.1. Conductivities for different structures at room temperature, without and with the plasticizer PEG.

Filler / Matrix	No filler (S/cm)	Randomly dispersed LATP NPs (S/cm)	Ice-templated LATP NPs (S/cm)
PEO	3.6×10^{-8}	1.4×10^{-6}	6.8×10^{-6}
PEO/PEG	7.7×10^{-6}	1.5×10^{-5}	5.2×10^{-5}

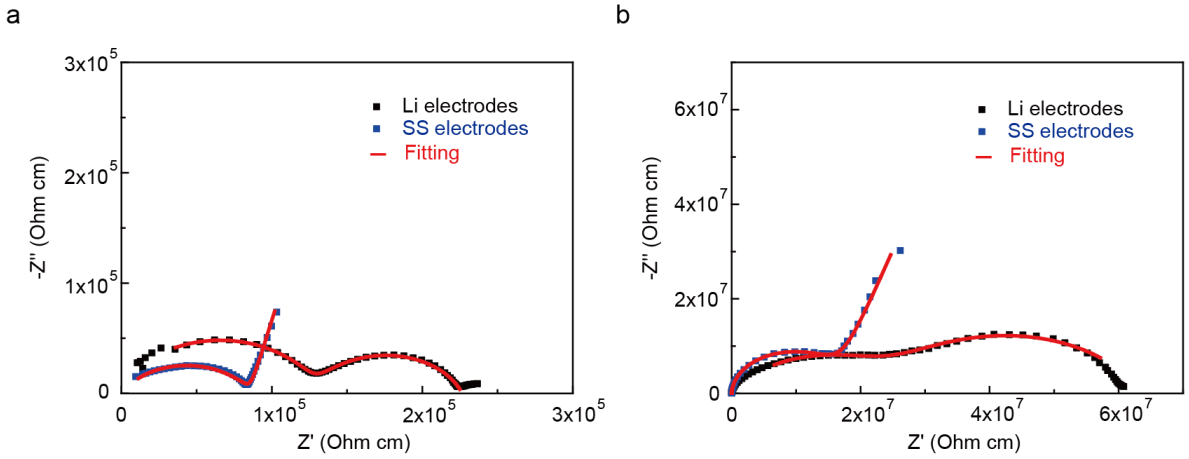

Figure 3.7. EIS measurements for SS and Li electrodes. (a) EIS for PEO/PEG with Li and SS electrodes. (b) EIS for PEO with Li and SS electrodes.

Although an improved ionic conductivity has been observed in the ice-templated composite electrolyte, it is still much less than the theoretical value (0.4×10^{-4} S/cm) based on the volume portion and the ionic conductivity of LATP (40%, 1.0×10^{-4} S/cm) and PEO (60%, 3.6×10^{-8} S/cm). This is likely due to the poor ionic transport at particle-particle interfaces, which may arise

from two factors: 1) the poor conduction at the LATP-LATP particle interfaces, since the ice-templated film is not pressed, and 2) interfacial regions which form at the LATP/PEO interfaces and block the transport of Li ions along the pathways of LATP-PEO-LATP[45, 61]. To address this issue, PEG is added into the composite as a plasticizer to reduce the interfacial resistance and thus enhance the ionic conductivity. Although PEG is not stable with the lithium metal in the long term, here it is used as a model example to demonstrate the enhancement of the ionic conductivity after improving the interfacial conduction. As done for to EIS tests without PEG, three kinds of samples are prepared, including the pure PEO/PEG electrolyte, the PEO/PEG electrolyte with randomly dispersed LATP NPs, and the PEO/PEG electrolyte with ice-templated LATP NPs. As earlier, the volume portion of LATP NPs is kept at 40% in the two composite electrolytes. The pure PEO/PEG electrolyte has a conductivity of 7.7×10^{-6} S/cm at room temperature, which is two orders of magnitude higher than that of the pure PEO electrolyte. The conductivity further increases to 1.6×10^{-4} S/cm at 70 ^{o}C. After adding the randomly dispersed LATP NPs, the conductivity is 1.5×10^{-5} S/cm at room temperature, which is only twice that of the pure PEO/PEG electrolyte. This suggests that LATP does not help improve the ion transport significantly if particles are not well connected, especially when the matrix has a high conductivity. In contrast, the ice-templated LATP film reaches a conductivity of 0.52×10^{-4} S/cm at room temperature, 3.6 times that of the PEO/PEG electrolyte with randomly dispersed LATP NPs. The value is also 6.8 times that of the pure PEO/PEG electrolyte (Figure 3.6c). These results demonstrate that the rational design of vertically aligned LATP fillers play a role for the conductivity increase as well in the composite with the PEG plasticizer. Moreover, the conductivity of the PEO/PEG/ice-templated LATP composite electrolyte (0.52×10^{-4} S/cm) is 7.6 times that of the one without PEG (6.8×10^{-6} S/cm), indicating the plasticizer indeed improve transport at the LATP/LATP and

LATP/PEO interfaces. The conductivity of PEO/PEG/ice-templated LATP composite electrolyte (0.52×10^{-4} S/cm) is also almost the same as the theoretical value of conductivity (0.45×10^{-4} S/cm) discussed above, which supports the effectiveness of the ice-templated structure. This also suggests that a higher conductivity of 3.0×10^{-4} S/cm could be realized if ceramic fillers with higher conductivity are used, such as LLZO[23, 32, 33] or sulfides[25, 26]. The reason why the conductivity is beyond the theoretical value may be that the PEG plasticizer helps improve the interfacial transport between ceramic particles and polymer/ceramic particles.

The porous LATP film itself without polymer is too fragile to measure its intrinsic conductivity. In order to validate that LATP contributes significantly to the ionic conduction, we measured the conductivity of the sintered porous LATP film soaked in dilute liquid organic electrolyte (0.125 mM $LiPF_6$ in ethylene carbonate/diethyl carbonate of weight ratio 1:1, with the conductivity of 1.1×10^{-5} S/cm) instead of polymer, as shown in Figure 3.8. The EIS measurement is conducted with stainless steel as the electrodes.

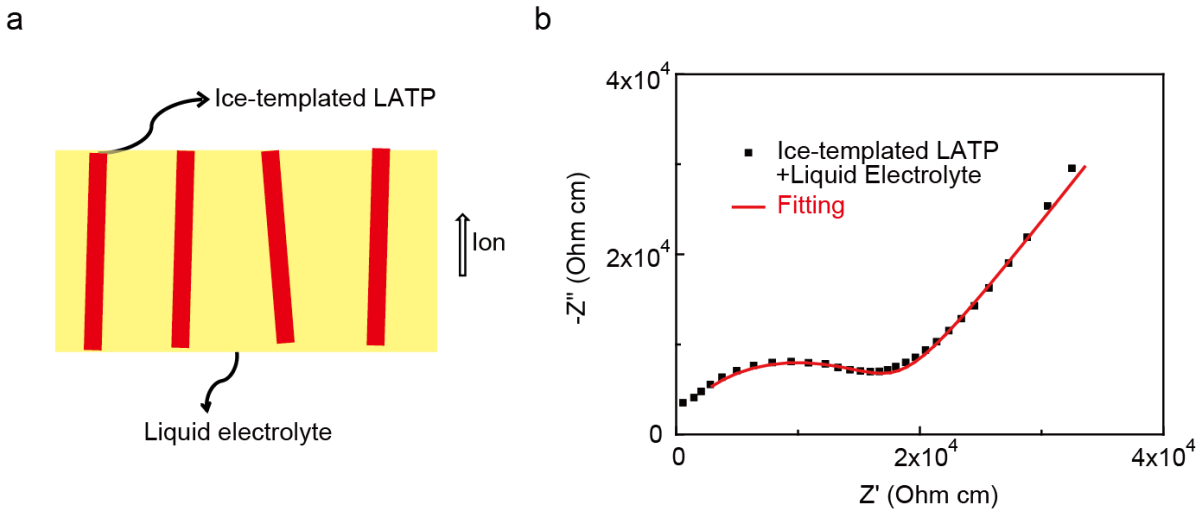

Figure 3.8. Ice-templated LATP with liquid electrolyte. (a) Schematic of the sample, combining ice-templated LATP with liquid electrolyte. (b) EIS measurement for ice-templated LATP with liquid

electrolyte, with a conductivity of 5.9×10^{-5} S/cm based on the total area of LATP and pores (filled with electrolyte).

Such sample shows a conductivity of 5.9×10^{-5} S/cm (Figure 3.8). Based on the porosity (60%) of the film and the fact that the liquid electrolyte and LATP are in parallel, the corresponding conductivity of the LATP bulk phase is estimated to be 1.2×10^{-4} S/cm, which is consistent with our result of the LATP pellet conductivity. This indicates that the LATP phase is the key reason for the high conductivity.

LATP is just an example to demonstrate the effectiveness of vertically aligned and connected ceramic fillers for enhancing ionic conductivity[62], and the concept can be applied to other ceramic solid electrolytes such as LAGP, LLZO and sulfides. LAGP has similar properties with LATP, so ice-templating with water should also work with LAGP ceramic particles. LLZO is known to be unstable in water due to the ion-exchange between LLZO and protons in water[63]. However, we find that adding LiOH into water could compensate lithium loss in water and the LLZO phase is recovered after sintering at 900 ^{o}C (Figure 3.9).

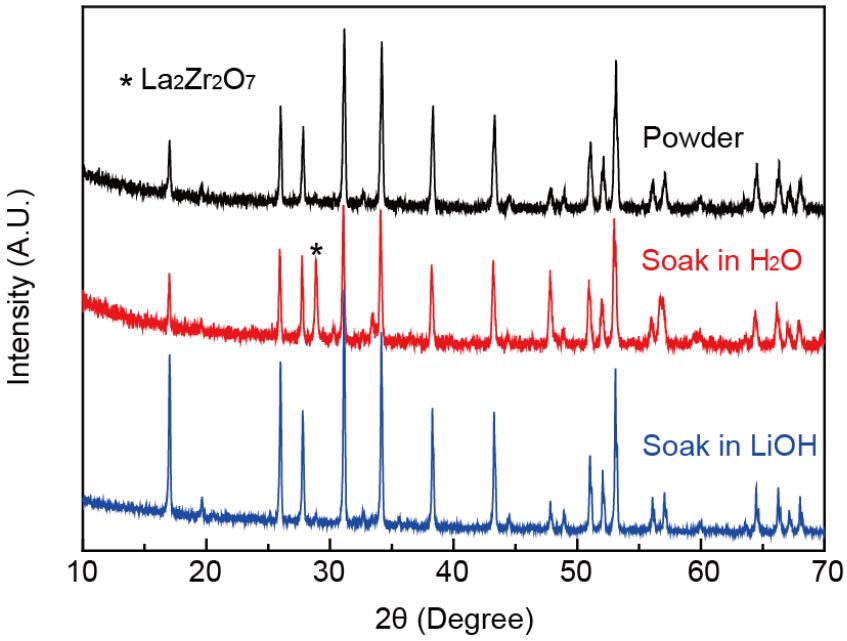

Figure 3.9. XRD for the as-synthesized LLZO powders (black), LLZO powders soaked in DI water and heated at 900 °C (red), and LLZO powders soaked in 2M LiOH solution and annealed at 900 °C (blue). A secondary phase of $La_2Zr_2O_7$ shows up for the sample soaked in pure water, but it does not exist if LLZO powders are soaked in 2M LiOH solution.

Therefore, LLZO is compatible with proposed ice-templating method. For sulfides, water can be replaced by camphene, which also produces the vertical structure and allows the operation at room temperature[64].

To test the battery cycling performance by charging and discharging with lithium metal anode, LATP cannot be used since it will be reduced by lithium metal (Figure 3.10).

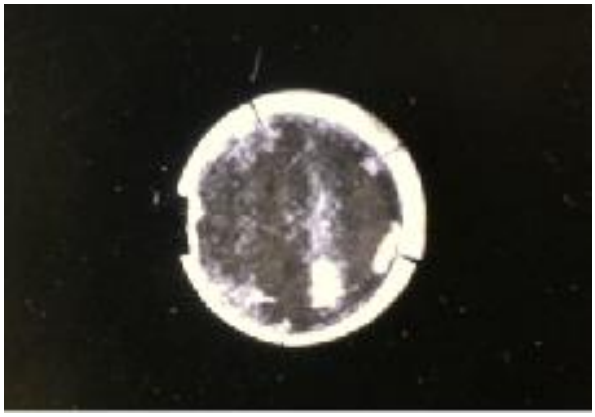

Figure 3.10. After contacting with lithium metal for 24 hours, the LATP pellet turns into black, indicating that LATP is reduced by the lithium metal.

Since LAGP has the similar properties with LATP, and it is stable with lithium metal[30, 65, 66], LAGP can serve as the ceramic electrolyte in the ice-templating technique to test the battery cycling performance with cathode and lithium metal anode. As expected, vertically aligned structure can be obtained with LAGP (Figure 3.11), just like in LATP.

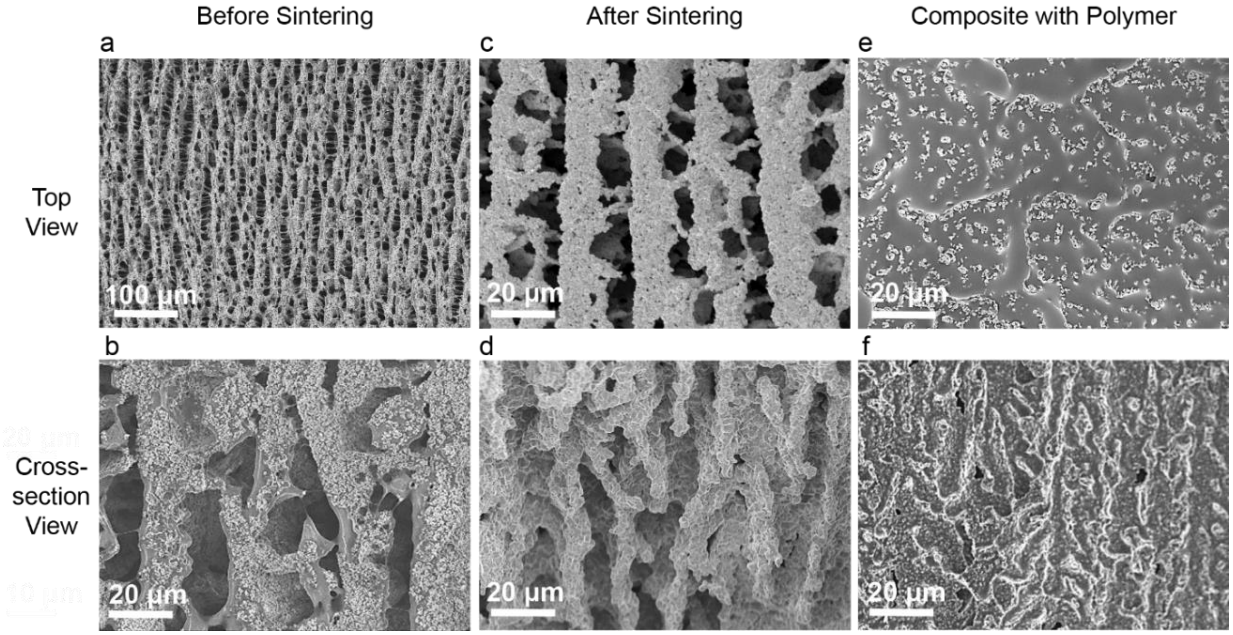

Figure 3.11. SEM images of the ice-templated LAGP solid electrolyte. (a) Top view before sintering, (b) Cross-section view before sintering, (c) Top view after sintering, (d) Cross-section view after sintering, (e) Top view of the solid electrolyte after PEO polymer filling, (f) Cross-section view after polymer filling.

To verify the ionic conduction, the electrochemical impedance spectroscopy (EIS) of the ice-templated LAGP/PEO composite electrolyte is tested at different temperatures in Figure 3.12. Its ionic conductivity could achieve 1.67×10^{-4} S/cm at room temperature and finally reaches 1.11×10^{-3} S/cm when heated to 60 ℃.

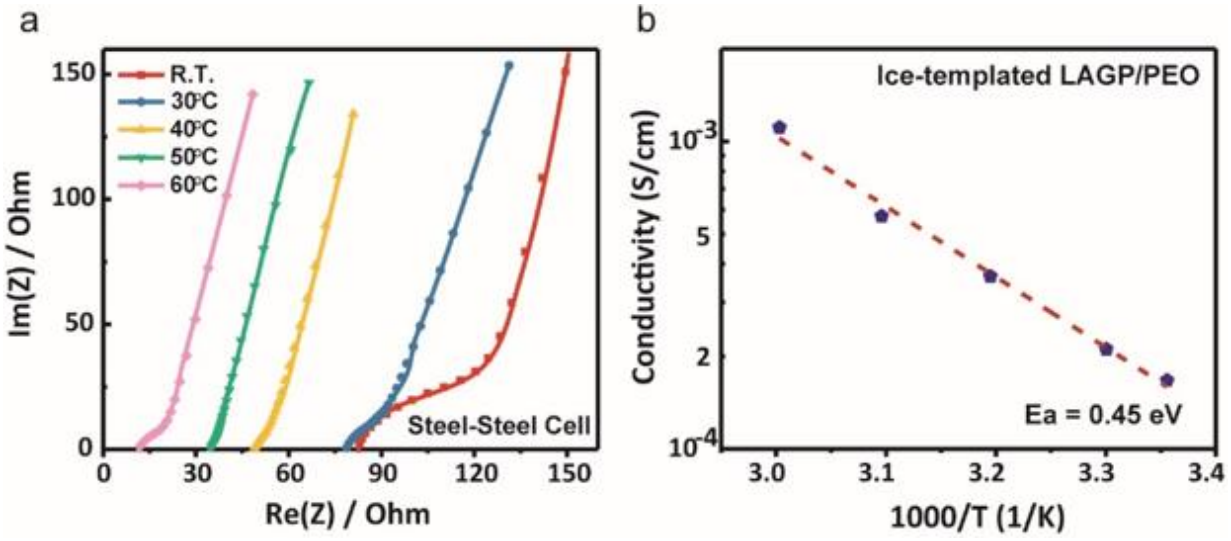

Figure 3.12. EIS at different temperatures for LAGP/PEO. (a) EIS at different temperatures for the ice-templated LAGP/PEO composite electrolytes. The test is performed with stainless steel electrodes. (b) Ionic conductivities and activation energy of the ice-templated LAGP/PEO composite electrolytes.

For the Li-LAGP/PEO-Li symmetric cell to test the cycling stability of lithium ion moving back and forth by charging and discharging, the cycling remains stable for 200 hours with a current

density 0.1 mA/cm^2 and capacity 0.1 mAh/cm^2. Increasing to 0.3 mA/cm^2 and 0.3 mAh/cm^2, the cycling is still stable for 200 hours in Figure 3.13a. This result indicates the LAGP/PEO composite electrolyte is stable towards lithium metal anode. To demonstrate the feasibility of the LAGP/PEO composite electrolyte in a cell, $LiFePO_4$ (LFP) and lithium metal are used as the cathode and the anode respectively. In the cycling test with the voltage range 2.5 – 3.8 V, the cell has an initial capacity of 148.7 mAh/g at 0.2C for the first cycle. When the current increases to 0.3C, the capacity remains at 141.0 mAh/g after 200 cycles, and the capacity retention is above 95% (Figure 3.13b). This result further testifies that the stable cycling with lithium metal and also LFP cathode could be achieved with this composite electrolyte. The voltage profile in Figure 3.13c shows that from the 1st cycle to 200th cycle, the voltage hysteresis remains unchanged at ~0.15 V. This small and stable voltage hysteresis illustrates an unobstructed lithium ion transportation in our vertically aligned LAGP ceramic structure. Moreover, this vertically aligned structure with rapid Li^+ transport also benefits power capability. The cell delivers capacities of 150.6 mAh/g, 139.0 mAh/g and 123.7 mAh/g at rates of 0.3C, 0.5C, and 1C, respectively, and retains the capacity steadily for 10 cycles (Figure 3.13d). After that, the same cell is cycled following 0.2C rate for 30 cycles and 0.6C rate for more than 400 cycles. The rate capability performance with a high capacity retention 87.4% over 400 cycles under 0.6C demonstrates the benefits from the unique vertically aligned structure.

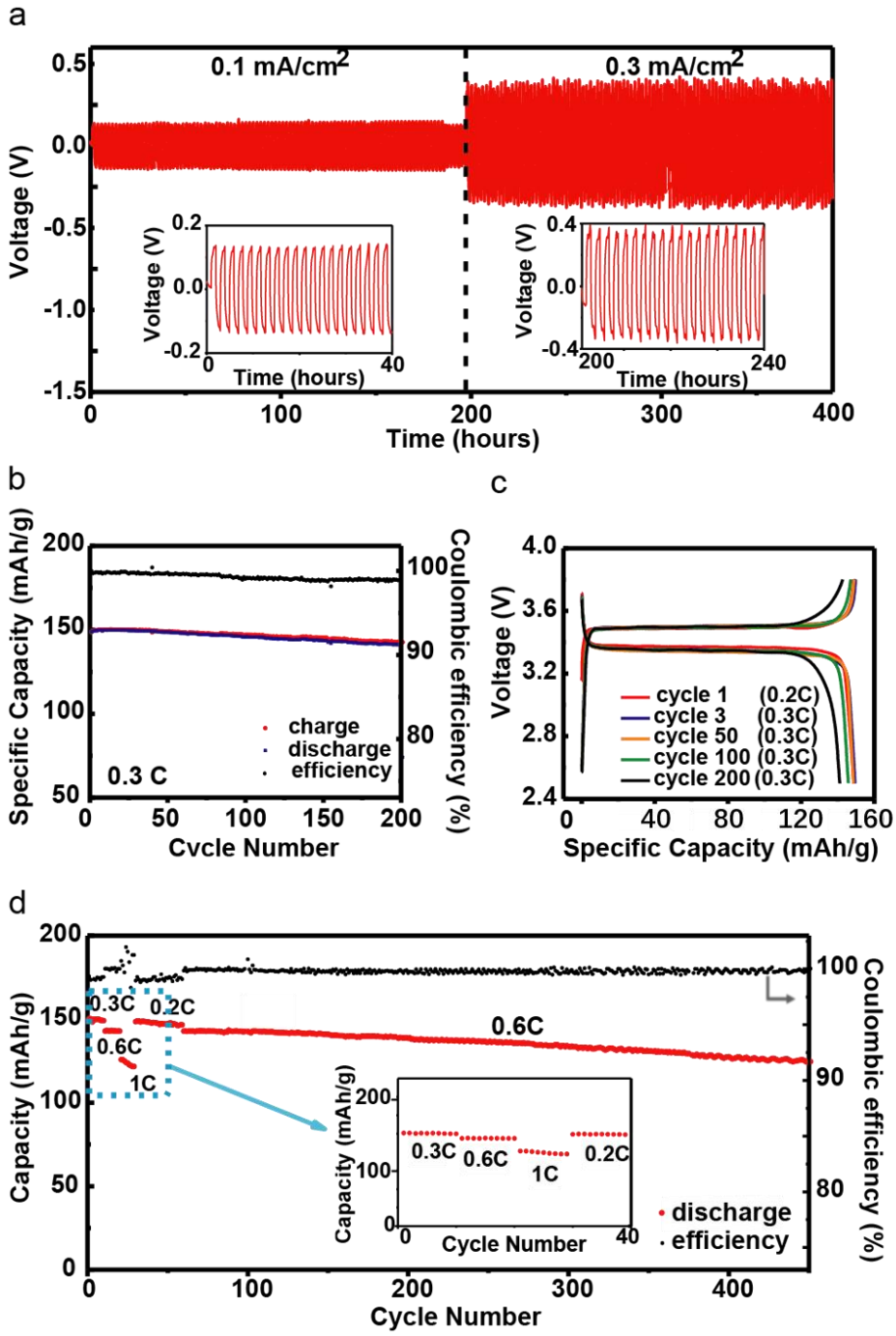

Figure 3.13. Electrochemical characterizations of LAGP/PEO system. (a) Voltage profiles at current densities 0.1 and 0.3 mA cm^{-2}, and capacities 0.1 and 0.3 mAh cm^{-2}, respectively. (b) Galvanostatic charge and discharge profiles of Li-LAGP/PEO-$LiFePO_4$ cell at 0.2 C for the first two cycles and 0.3 C for the following 200 cycles between 2.5 V to 3.8 V vs Li^+/Li. (c) Voltage profile at different cycles of Li-LAGP/PEO-$LiFePO_4$ cell between 2.5 V to 3.8 V vs Li+/Li. The testing condition is the same as (b). (d)

Rate capacities of the Li-LAGP/PEO-$LiFePO_4$ cell cycling at different rates from 0.3C to 1C and continuously cycling at 0.6C for 400 cycles. All the tests are performed at 60 °C.

3.5 Conclusion

Replacing flammable organic liquid electrolytes with solid Li-ion conductors is a promising approach to realize safe rechargeable batteries with high energy density. Composite solid electrolytes, which are comprised of a polymer matrix with ceramic Li-ion conductors dispersed inside, are attractive, since they combine the flexibility of polymer electrolytes and high ionic conductivities of ceramic electrolytes. However, the high conductivity of ceramic fillers is largely compromised by the low conductivity of the matrix, especially when nanoparticles (NPs) are used. Therefore, optimizations of the geometry of ceramic fillers are critical to further enhance the conductivity of composite electrolytes.

In this chapter, the fabrication of a flexible composite electrolyte composing of a vertically aligned and connected ceramic particles and a polymer is presented. LATP and LAGP NPs in the polyethylene oxide (PEO) matrix are aimed to maximize the ionic conduction, while maintaining the flexibility of the composite. This vertically aligned structure can be fabricated by an ice-templating-based method, and its conductivity reaches 0.52×10^{-4} S/cm for LATP/PEO, and 1.67×10^{-4} S/cm for LAGP/PEO composite electrolytes, which are several times higher than that of the composite electrolyte with randomly dispersed LATP/LAGP NPs. The composite electrolytes also show enhanced thermal and mechanical stability compared to the pure PEO electrolyte. The LFP-LAGP/PEO-Li cell reaching 148.7 mAh/g during the first discharge at 0.3C has over 95% capacity retention after 200 cycles. This method opens a new approach to optimize ion conduction in composite solid electrolytes for next-generation rechargeable batteries.

PEO and PEG are polyether-based electrolytes, and they are not stable above 4 V, vs. Li^+/Li, so that it is considered to be only compatible with $LiFePO_4$ with lower energy density, but not 4 V $Li(Ni_xMn_yCo_{1-x-y})O_2$ electrode materials with high energy density, limiting their use for high energy density applications such as electric vehicles. In the next chapter, we propose a solution to stabilize the polyether-based electrolytes at high voltage above 4 V.

Chapter 4: Polyether-based Nonflammable Electrolyte with High Voltage Cathode

4.1 Introduction

Lithium-based rechargeable batteries with high energy density are highly attractive for applications ranging from portable electronics to electric vehicles and grid-level energy storage. However, higher energy density is typically accompanied by lower thermal stability and higher safety risk[67, 68]. One intrinsic and critical safety issue in lithium-based batteries is the flammability of liquid organic carbonate electrolyte, which has a low flash point around room temperature[69]. Although ionic liquids have shown potential to be non-flammable, their costs are high for large-scale production[70]. Polyethylene oxide (PEO) or polyethylene glycol (PEG)-based electrolytes are attractive to address this issue on thermal stability, as they have much higher flash point (e.g. >150-200 ℃), and they are compatible with state-of-the-art techniques for industrial manufacturing[60]. Unfortunately, PEO is a polyether and easily oxidized above 4.0 V vs. Li^+/Li, so that it is traditionally considered to be only compatible with $LiFePO_4$ with lower energy density, but not 4 V $Li(Ni_xMn_yCo_{1-x-y})O_2$ electrode materials with high energy density[14]. Although various reports have shown anodic stability beyond 4.5 V vs. Li^+/Li in cyclic voltammetry tests with stainless steel electrodes[22, 71], most full cell tests are with $LiFePO_4$, except few with $LiMn_{1-x}Fe_xPO_4$[72]. In contrast, $LiCoO_2$/PEO/Li cells show fast capacity decay, even with polymeric protection on the surface[73]. This suggests that the Ni/Co-rich surface of $Li(Ni_xMn_yCo_{1-x-y})O_2$ catalyzes oxidation reaction of PEO and accelerate its degradation. Therefore, we hypothesize that effective passivation of NMC will reduce the surface's activity toward PEO oxidation, and its cycling performance can be stabilized.

4.2 Protective Coating Layer for the Cathode

By hypothesizing that effective passivation of NMC will reduce the surface's activity toward PEO oxidation and the cycling can be stabilized, 2 nm Al_2O_3 coating is formed on the $Li(NMC)_{1/3}O_2$ (NMC) electrode by atomic layer deposition (ALD) to passivate the surface in our experiment, and possibly the as-coated electrode shows significantly improved stability with short-chain polyethylene glycol electrolyte (Molecular weight Mw of 500). The design is shown in Figure 4.1A.

The coating of Al_2O_3 was performed in a Cambridge Nanotech Savannah 200 ALD system. ALD coating is performed on as-prepared NMC electrode by alternating water and trimethyl aluminum sources in a 4-inch ALD chamber. To allow precursors fully penetrating the torturous battery electrode, a 5 s holding period is inserted between precursor pulse (0.03 s) and pumping (30 s). The existence of ALD Al_2O_3 coating is clearly shown in the high-angle annular dark-field (HAADF) image in Scanning Transmission Electron Microscopy (STEM) (Figure 4.1B), where a 2 nm amorphous coating presents on NMC surface, and EDS mapping shows that the coating layer is Al_2O_3, indicated by the concentrated Al signal (Figure 4.1C-E). The existence of Al_2O_3 is further supported by Energy Dispersive Spectrometer (EDS) in Scanning Electron Microscope (SEM), as a clear peak of Al can be seen in the spectrum over a large area (Figure 4.1F).

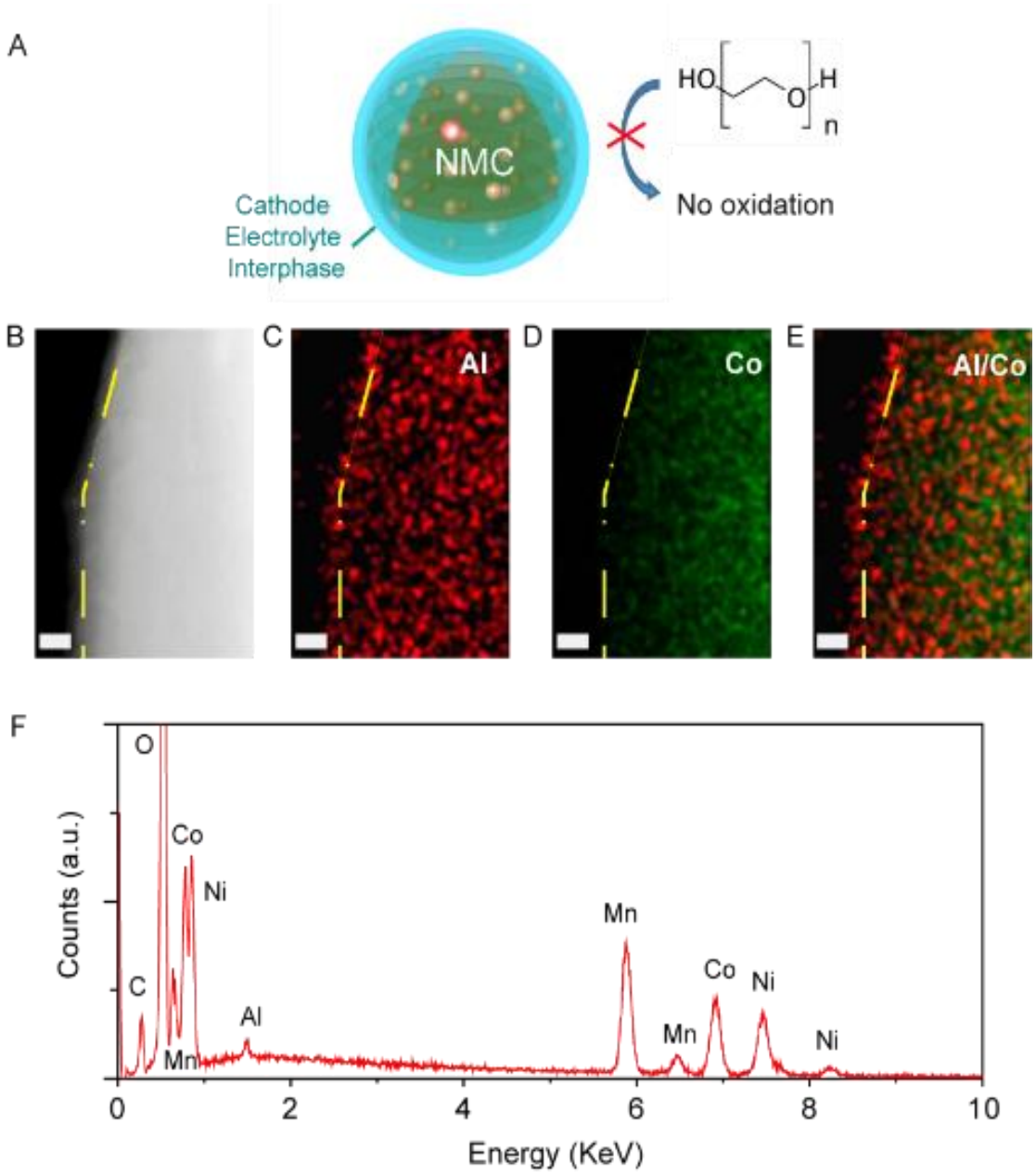

Figure 4.1. Design of Cathode Electrolyte Interphase coating to suppress the oxidation of PEO and stabilize the NMC cathode. (A) A schematic to illustrate the concept of protection. (B) The HAADF image of an NMC electrode with 2 nm Al2O3 coating by atomic layer deposition (ALD). (C-E) EDS mapping of (C) Aluminum, (D) Cobalt and (E) overlapping of Aluminum and Cobalt in the STEM mode. All scale bars are 5 nm. (F) EDS spectrum in SEM for large area. Al peak is clear.

4.3 Electrochemical Characterizations

To evaluate the effectiveness of such oxide coating, the as-coated NMC electrode is combined with poly(ethylene glycol) dimethyl ether (PEGDME) with M_w of 500, and a binary salt of 0.6 M lithium bis(trifluoromethanesulfonyl)imide (LiTFSI) and 0.4 M lithium bis(oxalato)borate (LiBOB). The reason to choose such small M_w is to increase the electrolyte conductivity, which reaches 1.1×10^{-3} S/cm at 30 ℃ and 3.4×10^{-3} S/cm at 60 ℃ (Figure 4.2).

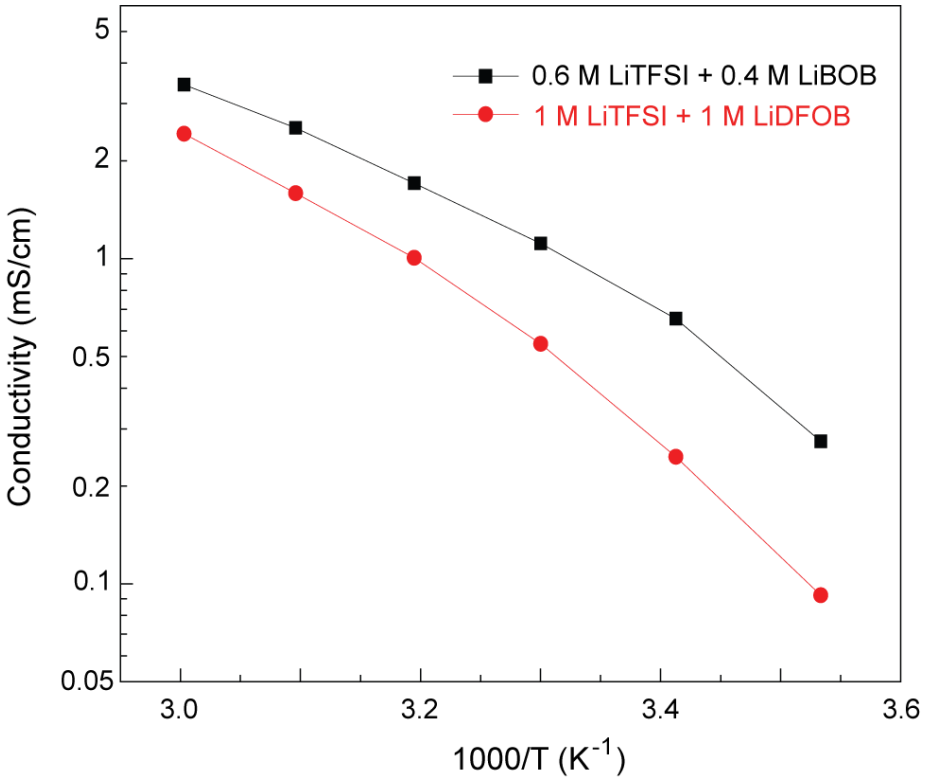

Figure 4.2. Conductivity of 0.6 M LiTFSI + 0.4 M LiBOB in poly(ethylene glycol) dimethyl ether (M_w = 500) and 1 M LiTFSI + 1 M LiDFOB in poly(ethylene glycol) dimethyl ether (M_w = 500) between 10 and 60℃.

Meanwhile, as the chemical nature of PEGDME and PEO with higher molecular weight are the same, the low M_w should have little effect on electrochemical/chemical reactions between

NMC and the electrolyte, and our conclusion that Al_2O_3 coating can stabilize such polyether electrolyte with 4V NMC cathode should not change. For simplicity, we will use the abbreviation PEG instead of PEGDME with M_w of 500 in this article. The dual salt combination of LiBOB and LiTFSI is selected as it can help prevent Al substrate from the corrosion of LiTFSI[74-76].

The electrochemical performance of such Al_2O_3-coated NMC / PEG-LiTFSI-LiBOB / Li cell is first tested by galvanostatic cycling. After two cycles at C/10, the cell is charged at C/3 (1C = 150 mA/g) followed by a CV step down to C/20, and discharged at C/3. Both ranges of 2.8-4.2 V and 2.8-4.25 V are tested. In the 2.8-4.2 V range, it is clear that the cycling stability is greatly enhanced with thicker ALD coating (Figure 4.3). Without coating, the initial capacity at C/3 is 130.1 mAh/g, but drops fast to 26.3 mAh/g after only 40 cycles (Figure 4.3C). Improvement can be already seen in 1 nm coating, but not very effective. The initial capacity at C/3 is 125.1 mAh/g, and remains at 108.3 mAh/g after 40 cycles. However, the capacity decays fast between the 50^{th} and 80^{th} cycle, and is below 10 mAh/g at the 100^{th} cycle. In contrast, with 2 nm coating, the initial capacity at C/3 reaches 128.5 mAh/g, and maintains as high as 101.8 mAh/g after 100 cycles, and 85.7 mAh/g at the 200th cycles. This represents a capacity retention of 66.7% after 200 cycles or a loss of only 0.021% per cycle.

Such improved performance clearly validates our hypothesis that a high-quality cathode electrolyte interphase (CEI, typically used to describe the cathode-side surface layer that is composed of solid-phase electrolyte decomposition products) can passivate NMC surface and suppress the oxidation of PEG electrolytes. This is further confirmed by the stabilized Coulombic efficiency (CE) for samples with Al_2O_3 coating. First, the initial CE increases slightly from 83.0% at 0 nm to 84.0% at 1 nm, and 84.9% at 2 nm Al_2O_3 coating, and the average CE in the first 100 cycles at C/3 also improves from 98.10% for 0 nm to 98.60% for 1 nm and 99.43% for 2 nm

coating. Moreover, a strong correlation is also observed between the onset of fast capacity fading and the destabilization of CE. Once CE starts to fluctuate, such as the 16th cycle for bare NMC and the 50th cycle for 1 nm coating (marked by arrows), the capacity starts to fade quickly. This suggests that the fast capacity fading in samples without Al_2O_3 protection is induced by side reactions between NMC and the PEG electrolyte.

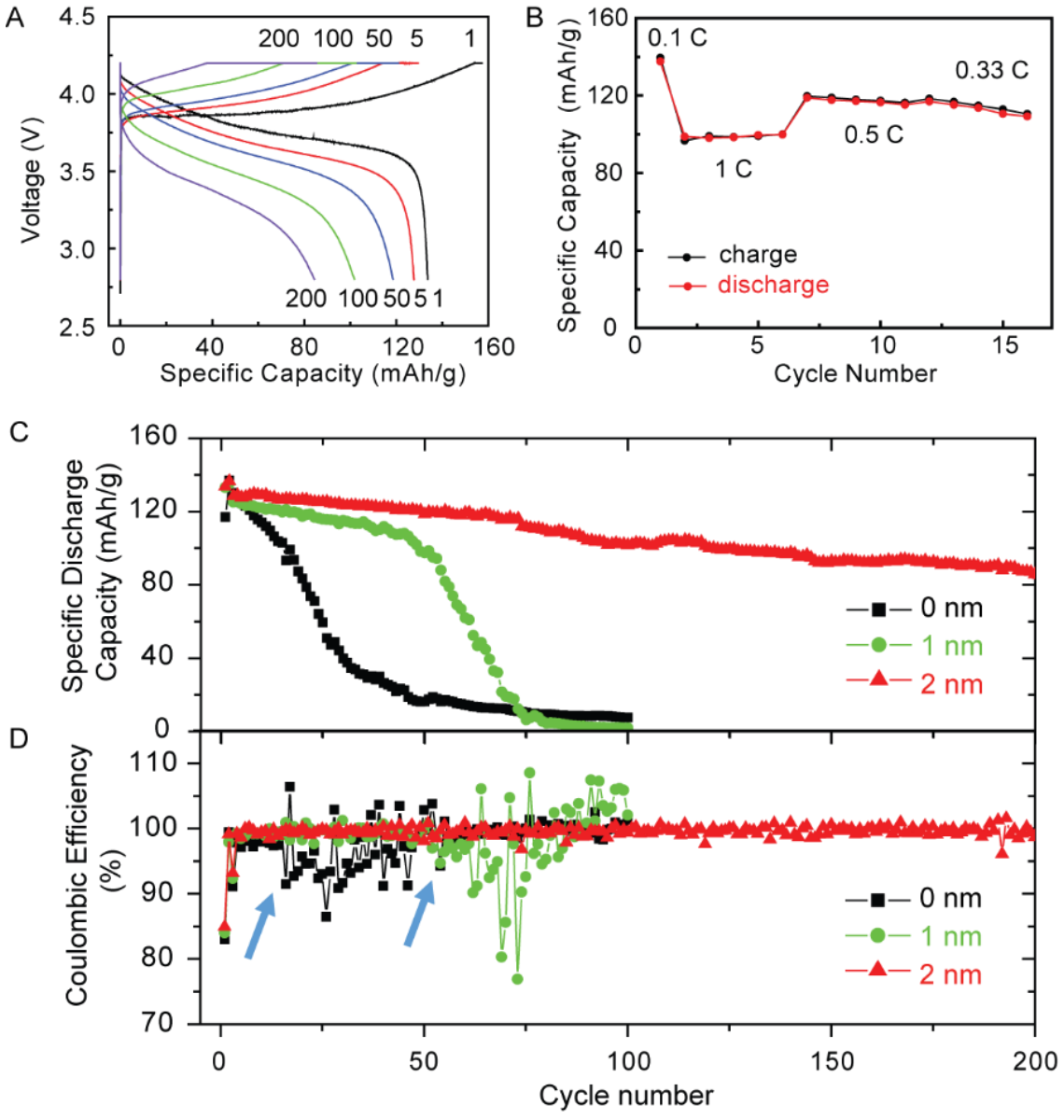

Figure 4.3. Electrochemical performance of Al_2O_3-coated $Li(NiMnCo)_{1/3}O_2$ (NMC) electrodes. (A) Voltage profiles of NMC electrode with 2 nm coating at 1st, 10th, 50th, 100th and 200th cycles. (B) Specific

discharge capacity vs. current rates for NMC electrode with 2 nm coating. (C) Cycling performance of NMC electrodes with 0, 1 and 2 nm Al_2O_3 coating. (D) Corresponding coulombic efficiency of NMC electrodes in (C). Cells in (A, C, D) are cycled at C/3 between 4.2 and 2.8 V (1 C = 150 mA/g). A constant voltage step is added at the end of Charging with a current cut-off of C/20. In (B), the testing condition is the same as (A, C, D) except that the discharge voltage cut-off is 2.7 V instead of 2.8 V.

The power capability of the 2 nm Al_2O_3-coated NMC electrodes are further evaluated for the range of 2.8-4.2 V. The specific capacity at 0.3, 0.5 and 1 C are 118.8, 116.9 and 98.8 mAh/g, which are 86.3%, 85.0% and 71.8% of that at 0.1 C (137.6 mAh/g). These results are reasonable for wide applications, and the lower discharge capacity at 1 C is likely a result of excessive resistance induced by the ALD coating, which can be further engineered to reduce resistance.

Similar trend of enhanced cycling stability is also observed when the cell is cycled between 2.8 and 4.25 V (Figure 4.4). Without coating, the initial capacity is 135.0 mAh/g, but drops fast to 19.3 mAh/g after 50 cycles. In contrast, with 2 nm coating, the initial capacity reaches 141.2 mAh/g, and maintains at 91.5 mAh/g after 100 cycles, or a capacity retention of 65%. The improved performance is further confirmed by the more stable CE for samples with Al_2O_3 coating. For bare NMC samples, the CE starts to fluctuate remarkably after 25 cycles with a standard deviation as high as 4.5%. In contrast, only a small fluctuation of 1.0% is observed in NMC with 2 nm coating after 50 cycles, with an average CE of 99.0%. Although the cycling performance is not as good as that with 4.2 V cut-off, the remarkable contrast between samples with and without ALD coating clearly demonstrate the effectiveness of Al_2O_3 passivation.

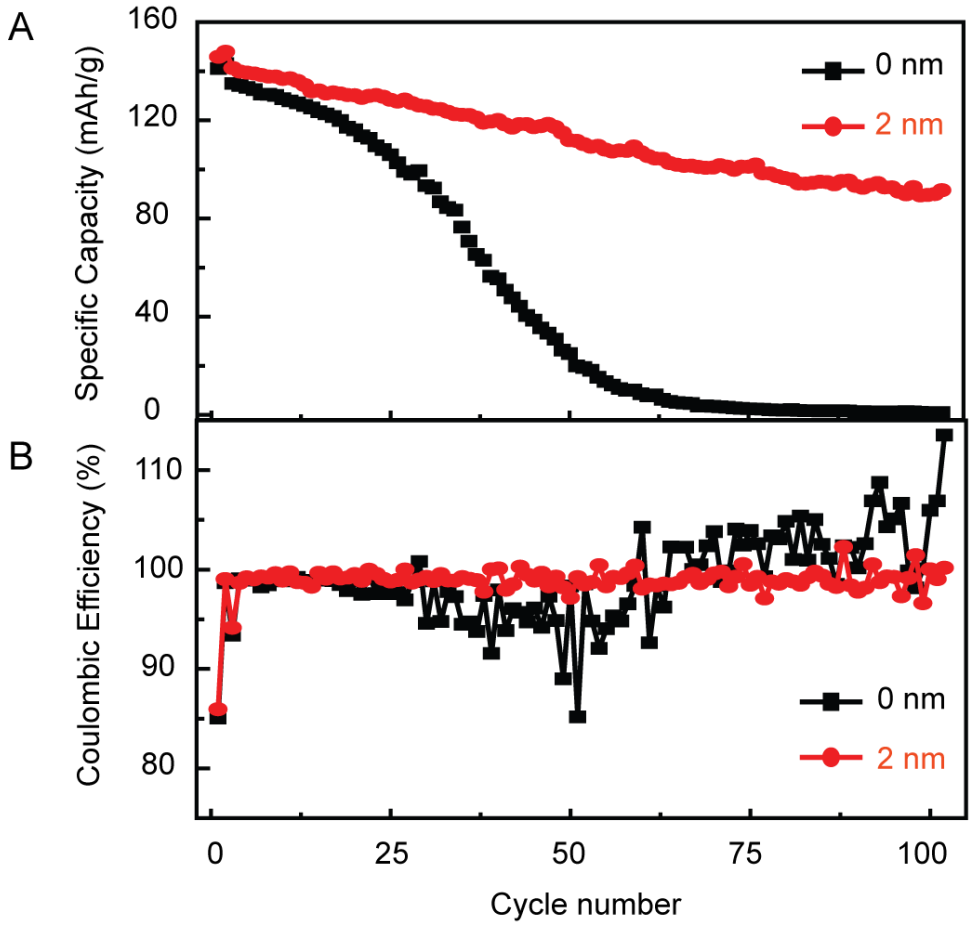

Figure 4.4. Electrochemical performance of Al_2O_3-coated NMC electrodes charged cycled between 2.8 and 4.25 V vs. Li^+/Li. (A) Cycling performance of NMC electrodes with 0 and 2 nm Al_2O_3 coating. (B) Coulombic efficiency of NMC electrodes in (A). All cells are cycled at C/3 between 4.25 and 2.8 V (1 C = 150 mA/g). A constant voltage step is added at the end of charging with a current cut-off of C/20.

To understand why the Al_2O_3 coating improves the cycling performance, the protective effect of Al_2O_3 is first examined by cyclic voltammetry of carbon fiber papers (CFPs). Carbon fiber papers (AvCarb MGL190) with and without 2 nm coating were combined with lithium metal counter electrodes, and scanned between 2.5 and 4.5 V vs Li^+/Li at 1 mV/s for 5 cycles (Figure 4.5A). The anodic current above 4.0 V vs Li^+/Li is significantly smaller than bare carbon,

indicating less oxidation of PEO electrolyte. For example, in cycle 1, anodic current densities on bare CFP are 13.7, 28.1 and 81.6 mA/cm^2 at 4.2, 4.3 and 4.5 V, respectively, but reduce to 7.9, 8.0 and 24.6 mA/cm^2 for CFP with 2 nm Al_2O_3 coating. Similarly, in cycle 5, while the anodic current density remains at 2.5, 3.5 and 28.1 mA/cm^2 at 4.2, 4.3 and 4.5 V for bare CFP, the current densities are only 0.78, 1.23, and 15.3 mA/cm^2 for CFP with 2 nm Al_2O_3, representing a reduction of 40-70% in the oxidation rate. It should be noted that the area for values above is based on geometric area, so the true anodic current density normalized to the electrode surface area is significantly lower. The background current due to double layer capacitance in Figure 4.5 is ~1 mA/cm^2 based on geometric footprint. As the scanning rate is 1 mV/s, the capacitance is ~1 mF/cm^2. Since the double layer capacitance on porous carbon surface is ~10 mF/cm^2, the estimated true surface area is ~100 cm^2, about 100 times of the geometric footprint[77].

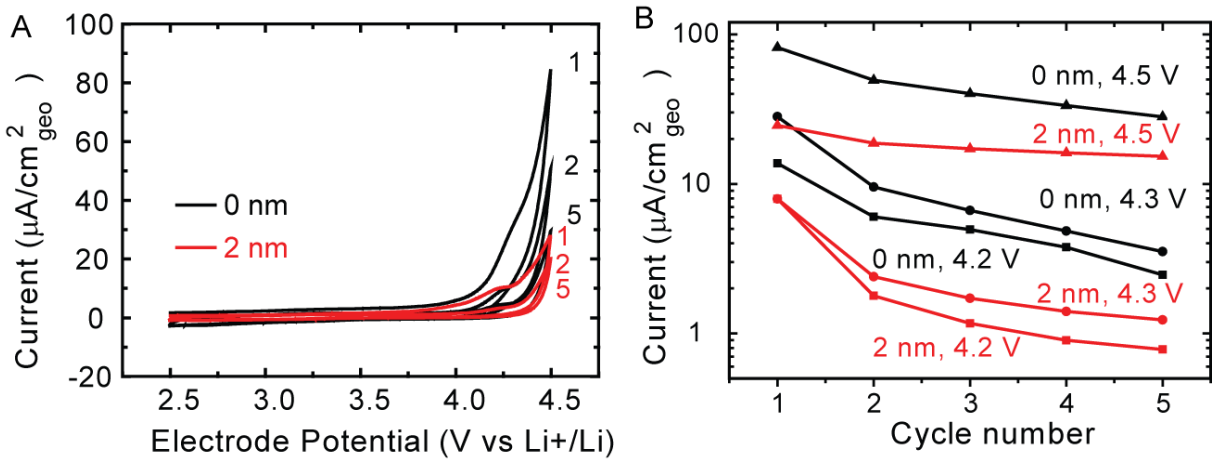

Figure 4.5. Electrochemical stability of PEO with NMC. (A) Cyclic voltammetry at cycle 1, 2 and 5 for NMC electrodes with 2 nm and without Al_2O_3 coating. The scan rate is 1 mV/s. (B) Corresponding anodic current densities at different electrode potentials for NMC electrodes with 2 nm and without Al_2O_3 coating. The background current due to double layer capacitance is subtracted based on the anodic current at 3.4 V vs. Li^+/Li in each cycle.

4.4 Analysis of the Cathode Electrolyte Interphase

The reduced oxidation rates of PEO may originate from multiple factors, such as reduced surface activity towards PEO oxidation, and changes in chemical composition in CEI. To better understand the protective mechanism, XPS depth profile of NMC electrodes after 50 cycles is measured. Two kinds of samples are compared: the bare NMC electrode and the NMC electrode with 2 nm Al_2O_3 coating, which were both rinsed in 1,2-dimethoxyethane (DME) for 15 seconds and dried before characterizations. Both samples are sputtered for 0, 2.5, 7.5 and 17.5 min to obtain the depth profile. As the nominal sputtering speed is 2 nm/min, they correspond to nominal depth of 0, 5, 15 and 35 nm, respectively. First, the Al peak is clear on NMC electrode with 2 nm Al_2O_3 coating. Interestingly, Al peaks at all depth correspond to Al-F bond instead of Al-O. This suggests that the Al_2O_3 coating reacts with F in LiTFSI to form AlF_3-like species during cycling, which is known to protect cathode materials[78, 79]. The F-1s peaks are also distinct for two samples. In the sample with 2 nm coating, although the surface signal is dominated by C-F from PVDF at 688.8 eV, the peak at 686.7 eV dominates for 2.5-17.5 min sputtering. This peak can be assigned to Al-F, which is consistent with results on the Al peak[79, 80]. The energy of 686.7 eV aligns with B-F too, which may come from the oxidation of LiBOB[81]. However, the concentration of B-F is unlikely to be high, since B signal is very weak on NMC surface (Figure 4.7A). On the other hand, the dominant F-1s signal in bare NMC is the C-F bond from PVDF. No Al-F or B-F is observed except a small peak at 17.5 min sputtering (Figure 4.6C).

O and C peaks also unveil important information. For the NMC electrode with 2 nm coating, although the dominant signal is C-O bond in O-1s (Figure 4.6D) and C-1s peaks (Figure 4.7), a metal-O peak arises starting from 2.5 min of sputtering (~5 nm), indicates that the CEI layer is thin[82, 83]. In contrast, on bare NMC electrode, no M-O bond is detected even down to 17.5 min

of sputtering (~35 nm), suggesting a thick layer of CEI, which may block ion transport. The difference in SEI thickness is also supported by XPS depth profile of Ni/Mn/Co, which shows up clearly after 2.5 min sputtering in the sample with 2 nm Al_2O_3 coating. On the other side, without Al_2O_3 coating, these transitional metals cannot be detected even after 17.5 min sputtering (Figure 4.8) [84]. C peaks further show that the major composition of carbon species in CEI is C-O-C (286.6 eV, ether) and C-C/C-H (284.8 eV) in both samples, with a low concentration of C=O centered at 289.2 eV, which may arise from the oxidation of PEG[81, 83, 85]. The XPS results clearly prove that there are remarkable differences of CEI for samples with Al_2O_3 coating and without coating. The participant of Al in CEI formation alters the surface chemistry and leads to more protective phases, such as AlF_x and BF_x, which slows down PEO oxidation. The thickness of CEI is also smaller, which facilitates ion transport.

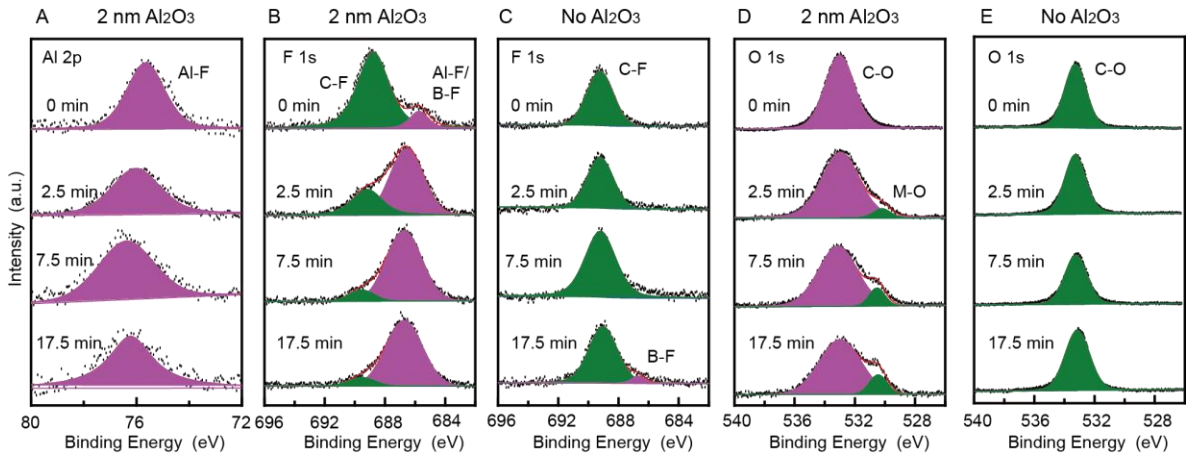

Figure 4.6. XPS depth profile on the surface of NMC electrodes cycled for 50 times. (A) Al-2p signal on NMC electrode with 2 nm Al_2O_3 coating. (B and C) F-1s signal on NMC with 2 nm Al_2O_3 coating (B) and bare NMC (C). (C) O-1s signal on NMC with 2 nm Al_2O_3 coating (D) and bare NMC (E).

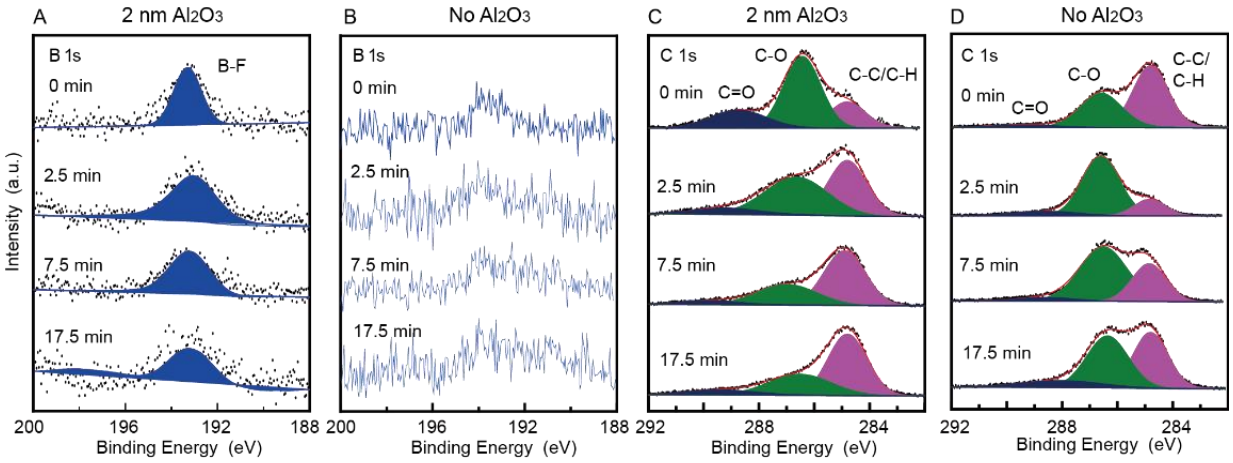

Figure 4.7. The XPS depth profile of NMC electrode after 50 cycles. (A and B) B-1s signal on NMC with 2 nm Al_2O_3 coating (A) and bare NMC (B). (C and D) C-1s signal on NMC with 2 nm Al_2O_3 coating (C) and bare NMC (D).

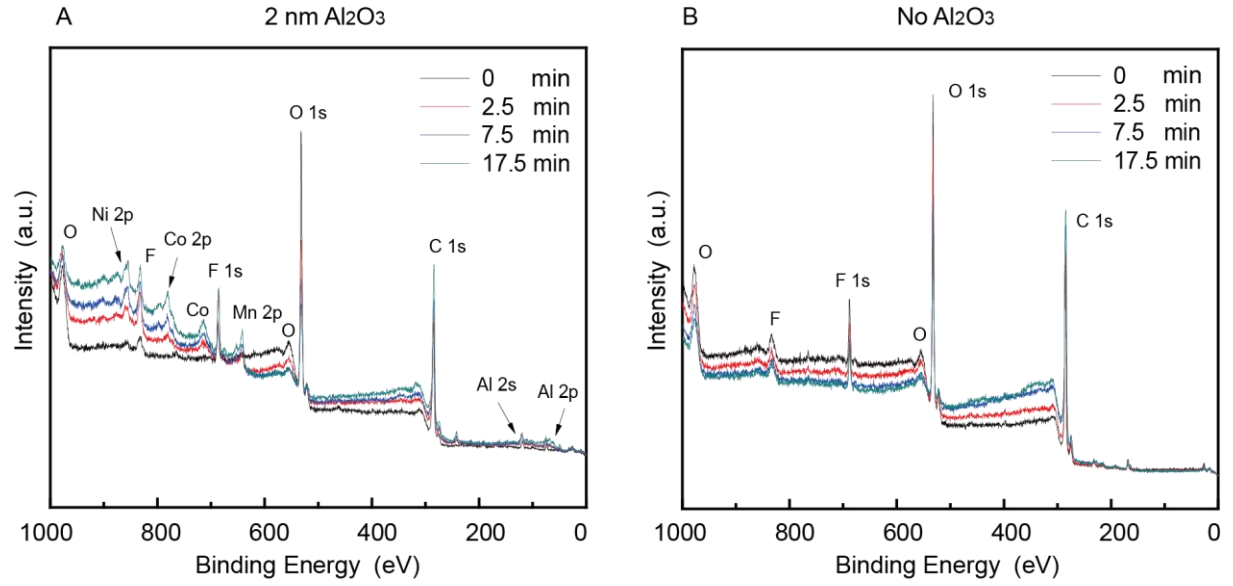

Figure 4.8. XPS surveys of NMC surface. (A) with 2 nm Al_2O_3 coating and (B) bare NMC. The peaks at 979 and 553 eV (in A and B) correspond to O Auger and O loss, respectively. The peak at 833 eV can be assigned to F Auger.

4.5 Nonflammability of the Electrolyte

Recently, Shuhong Jiao et al., reported highly stable cycling of NMC electrode in DME by using concentrated salt (2 M LiTFSI + 2 M LiDFOB), during the preparation of this paper[81]. The mechanism is that the decomposition of salt helps form a high-quality CEI to prevent the oxidation of this ether. However, DME is highly flammable, which has a low flash point of -2 ^{o}C[69]. Even with highly concentrated salt inside, it is easily ignitable (Figure 4.9a). In contrast, PEG has much better thermal stability. It has a high flash point of 156 ^{o}C, and it is difficult to catch fire under mild ignition (Figure 4.9B).

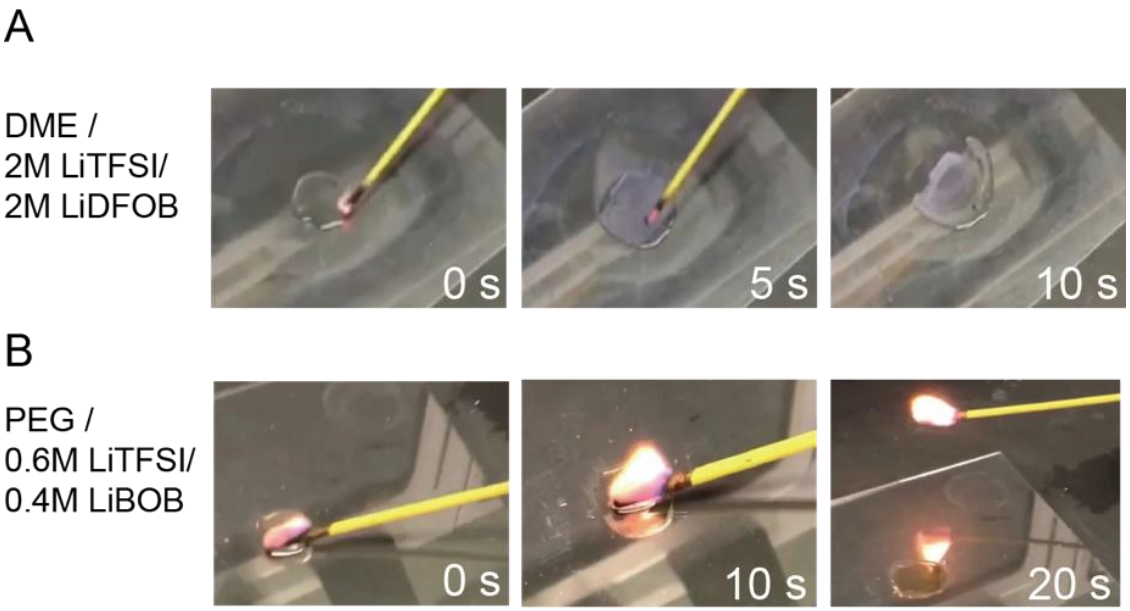

Figure 4.9. Flammability test. (A) 2M LiTFSI + 2M LiDFOB in DME and (B) our PEG-based electrolyte (0.6 M LiTFSI + 0.4 M LiBOB in PEG) at different times. DME electrolyte is easily ignitable, while PEG one does not catch fire for 30 seconds. The whole video can be found as supplemental video 1.

Moreover, regarding to cycling performance, the concentrated salt approach in PEG appears not as effective as in DME. First, the salt solubility in PEG is much lower than that in DME. Only 1 M LiTFSI + 1 M LiDFOB (1 M/1 M) can be dissolved inside, and the ionic

conductivity is only 5.5 × 10^{-4} S/cm at 30 °C, half of the 0.6 M LiTFSI + 0.4 M LiBOB in PEG electrolyte we use above. Moreover, such 1 M/1 M combination appears not highly effective regarding to preventing PEO oxidation. As illustrated in Figure 4.10A, bare NMC with 1 M LiTFSI + 1 M LiDFOB in PEG shows a similar cycling performance with bare NMC in 0.6 M LiTFSI + 0.4 M LiBOB in PEG, but it is much worse than 0.6 M LiTFSI + 0.4 M LiBOB in PEG with 2 nm Al2O3 coating. In addition, the average coulombic efficiency between cycle 10 and 23 is 98.03%, smaller than 99.44%, the CE with 2 nm Al2O3 coating in the same cycling range (Figure 4.10B). This demonstrates the importance of surface coating to alter surface chemistry and improve stability against electrolyte oxidation.

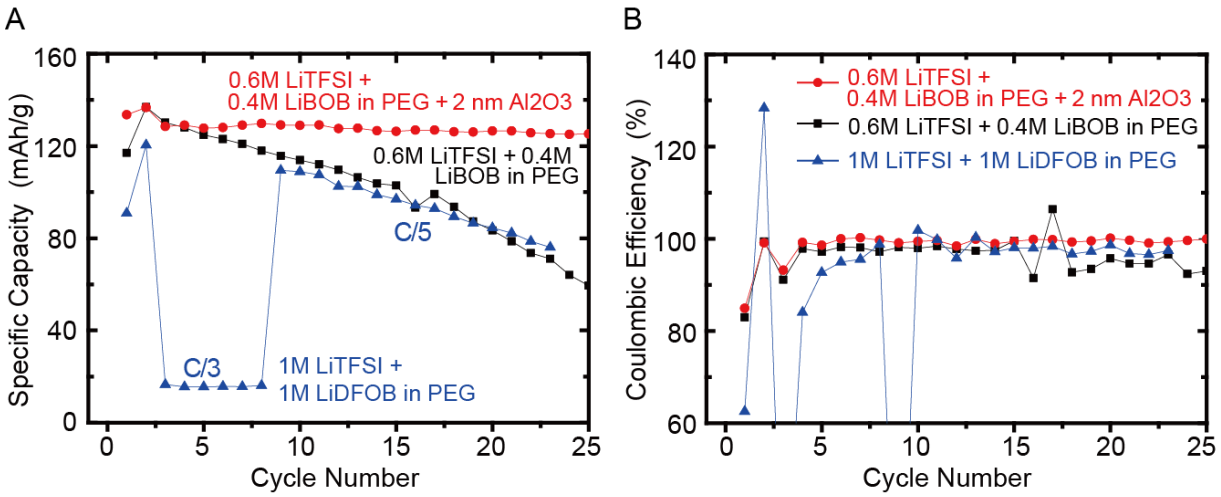

Figure 4.10. Effects of salt concentration. (A) Discharge capacity and (B) Coulombic efficiency vs. cycle number of concentrated 1 M LiTFSI + 1 M LiDFOB in PEG with bare NMC (blue), 0.6 M LiTFSI + 0.4 M LiBOB in PEG with bare NMC (black), and 0.6 M LiTFSI + 0.4 M LiBOB in PEG with 2 nm Al2O3-coated NMC (red). The data in red and black curves are the same as those in Figure 2. For 1 M LiTFSI + 1 M LiDFOB in PEG with bare NMC (blue), the cell is cycled at C/5 and C/10 for the 1st and 2nd cycle, respectively. The battery cannot be well cycled at C/3 due to reduced ionic conductivity, so the current was changed to C/5 at the 9th cycle. Therefore, due to the change of C rate, CE at the 3rd and 9th cycle are low, which are not included in (B).

4.6 Conclusion

Batteries with high energy density often has lower thermal stability and higher safety risks. Replacing flammable liquid organic electrolyte inside with more thermally stable ones is a promising solution, such as widely studied polyethylene oxide (PEO) or polyethylene glycol (PEG) electrolytes. Unfortunately, they are not stable with 4 V $Li(Ni_xMn_yCo_{1-x-y})O_2$ (NMC) cathodes, hindering them from application in batteries with high energy density.

In this chapter, we demonstrate that the compatibility between the polyether-based PEG electrolyte and NMC cathodes can be significantly improved by forming a 2 nm Al_2O_3 coating on NMC surface. This nanoscale coating dramatically changes the composition of the cathode electrolyte interphase and thus stabilizes PEG electrolyte with the NMC cathode. With the 2 nm ALD Al_2O_3 coating, the capacity remains at 84.7% after 80 cycles and 70.3% after 180 cycles. In contrast, the capacity fades to less than 50% after only 20 cycles in bare NMC electrodes. This study opens new opportunity to develop safe electrolyte for lithium batteries with high energy density.

Chapter 5: An Alternative PVdF/DMF-based Polymer Electrolyte for 4 V-class Cathode

5.1 Introduction

Solid-state lithium batteries have been intensively pursued as promising solutions to safety issues in Li-ion batteries with organic liquid electrolyte, such as leakage, flammability and unstable solid-electrolyte interface (SEI) formation[86-95]. Solid electrolyte is critical to the successful development of solid-state lithium batteries[96-102]. As an important class of solid electrolyte, solid polymer electrolytes (SPE), such as poly(ethylene oxide) (PEO), has attracted much attention due to their decent flexibility and facile processing compared with inorganic ceramic electrolytes[72, 103, 104]. However, the PEO–based SPEs usually show low ion conductivity (~ 10^{-6} - 10^{-7} S/cm) at room temperature[104], severely restricting their practical applications[105]. Tremendous efforts have been made to increase the ion conductivity of PEO-based electrolyte such as crosslinking[106], introducing ceramic fillers to form composite polymer electrolytes (CPEs)[98, 107-110] and adding plasticizers[110]. Beside low conductivity, PEO tends to be oxidized above 4 V vs Li/Li+, making it difficult to be paired with NMC materials and limiting energy density of the full cell. [109]. Therefore, developing polymer electrolyte stable with 4 V cathode and further enhancing their ionic conductivity are critical to the practical applications of solid-state lithium batteries. However, only occasional report on solid polymer electrolyte-based 4V batteries are reported [109].

Recently, poly(vinylidene fluoride) (PVDF) based SPE attracted much attention due to its non-flammability, easy processing, wide electrochemical window and high ion conductivity (~10^{-4}S/cm)[111]. In investigating the underlying transport mechanism in PVDF SPEs, we found that the quantity of dimethylformamide (DMF), which serves as both solvent and plasticizer, played a

significant role in ionic conductivity. Based on our results, when DMF remained at 20 wt% of the SPE, its ionic conductivity becomes higher than 1×10^{-4} S/cm. However, large amount of DMF plasticizer may soften the SPE and make it vulnerable to dendrite penetration.

To solve this issue, we demonstrate that nanowire fillers are excellent candidates to enhance mechanical strength. As a demonstration, we show that PVDF/DMF CPEs with randomly dispersed and interconnecting palygorskite nanowires exhibit both high ion conductivity and significantly enhanced mechanical properties. Palygorskite, a kind of hydrated magnesium aluminum silicate mineral ($(Mg,Al)_2Si_4O_{10}(OH)$), has been widely used as industrial floor absorbents, agricultural carriers, and environmental absorbents because of its particular physical properties[112, 113] . With one dimensional fiber structure, it can easily form an interconnected network even at low concentration, to provide excellent mechanical property. When added as fillers in the PVDF/DMF SPEs, it largely enhances both the stiffness and toughness of the membrane. The mechanical robustness allows suppression of lithium dendrite and improved cycling stability. The addition of 5 wt % palygorskite nanowires also enhances transference number of Li^+ from 0.21 to 0.54 as a result of interaction between the nanowires and ClO_4^- anions. With such high-performance PVDF/DMF CPEs, a solid-state lithium battery of $Li(Ni_{1/3}Mn_{1/3}Co_{1/3})O_2$ (NMC111)/PVDF-DMF/palygorskite CPE/Li presents a stable cycling over 200 times with 118.1 mAh/g discharge capacity retained. In addition to experiments, numerical calculations were also carried out, which further uncovers that nanowire−polymer interaction and interwire interactions are critical to the enhanced mechanical properties of samples with palygorskite nanowires added.

5.2 Fabrication Process and Film Characterizations

The free-standing PVDF/DMF-based polymer electrolytes and PVDF/DMF/palygorskite CPEs were prepared through a facile solution-casting method (Figure 5.1a).

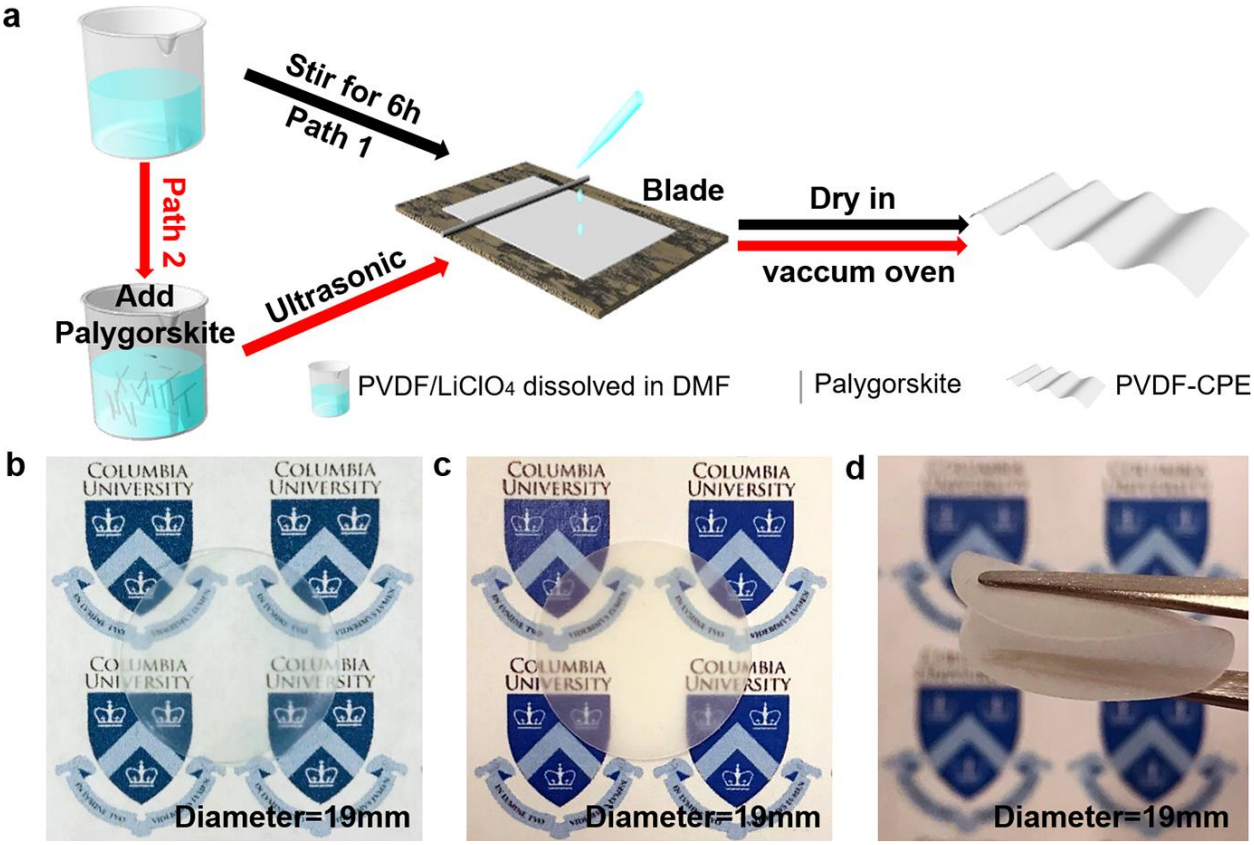

Figure 5.1. Fabrication of PVDF/DMF-based polymer electrolyte. (a) A Schematic diagram of the synthesis of PVDF/DMF-based polymer electrolytes and PVDF/palygorskite nanowires/CPE. (b–d) (b) PVDF/DMF polymer electrolyte membrane and (c) PVDF/DMF/palygorskite CPE membrane dried at 60 °C in vacuum chamber for 24 h. (d) Bent PVDF/DMF/palygorskite CPE showing excellent flexibility.

First, PVDF powders (Arkema Kynar 761), $LiClO_4$, and a certain amount of palygorskite nanowires were dissolved in DMF and stirred for 6 h at 50 °C. Then the solution was cast on glass and vacuum-dried at different temperatures between 25 to 120 °C to obtain free-standing PVDF/DMF-based polymer electrolytes containing different amounts of DMF. The film thickness

is ~100 μm. When vacuum-dried below 60 °C, the polymer electrolyte membrane is highly transparent and flexible, as shown in Figure 5.1c,d. However, if vacuum-dried above 80 °C, it turns nontransparent and the color changes from white to pale yellow. After adding palygorskite, the obtained PVDF/DMF CPEs are translucent with good flexibility (Figure 5.1d). The PVDF/DMF -based polymer electrolytes dried at various temperatures were first characterized by scanning electron microscopy (SEM). As shown in Figure 2a, compact and flat films with PVDF microstructures are presented, which help improve ionic conductivity.

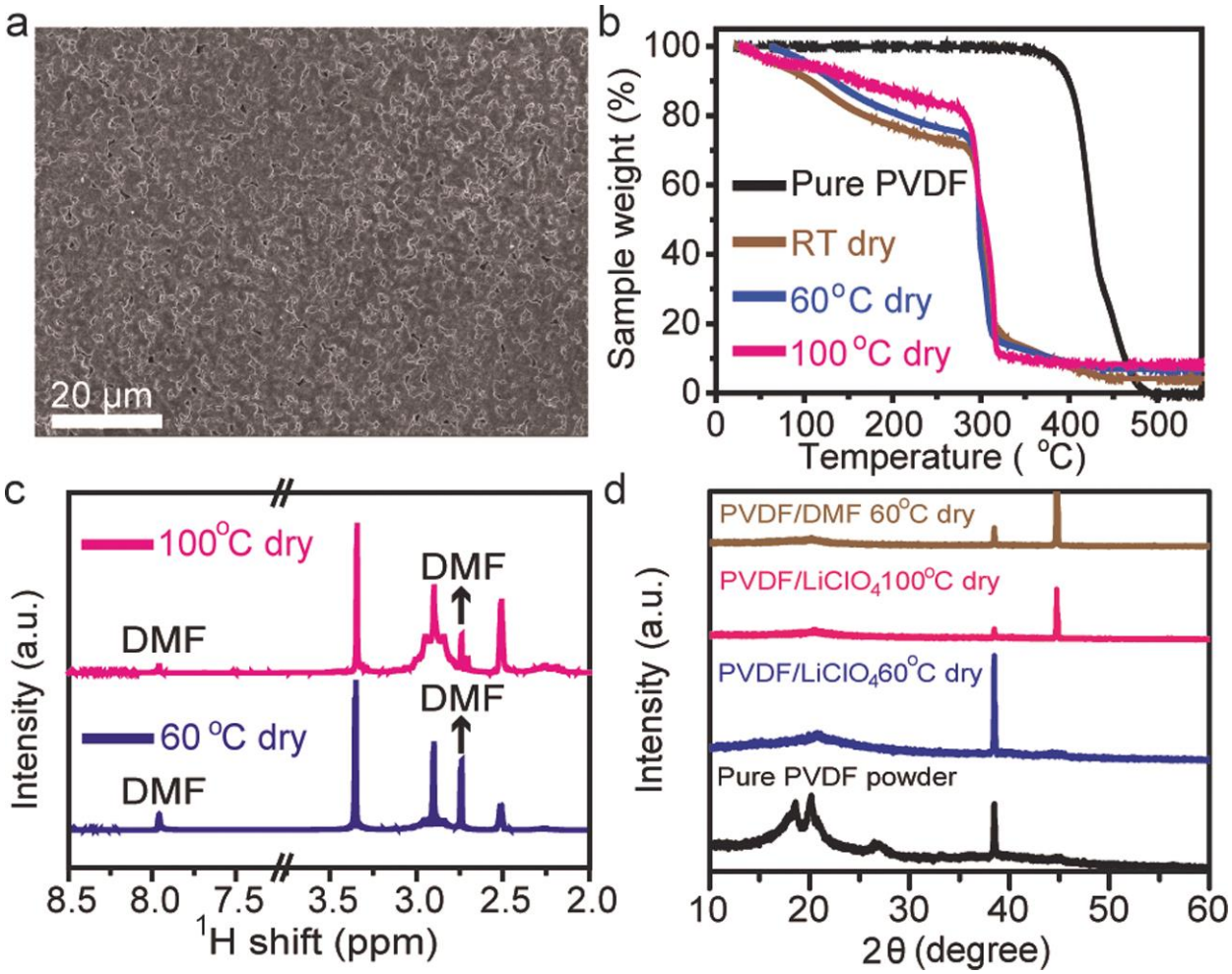

Figure 5.2. Characterizations of PVDF/DMF electrolyte dried at different temperatures. (a) SEM image of PVDF/DMF electrolyte vacuum-dried at 60 °C. (b) TGA curves of PVDF/DMF electrolyte under different temperatures in vacuum drying. (c) 1H NMR spectra of 60 and 100 °C vacuum-dried PVDF/DMF-

based polymer electrolytes. (d) XRD patterns of PVDF powder, PVDF electrolyte vacuum-dried at 60 °C, PVDF electrolyte vacuum-dried at 100 °C and PVDF/DMF vacuum-dried at 60 °C. The two peaks at 38.5° and 44.8° belongs to the aluminum substrate.

To investigate the thermal stability of PVDF/DMF polymer electrolytes and evaluate the amount of DMF inside, thermogravimetric analysis (TGA) and nuclear magnetic resonance (NMR) were performed. As shown in TGA results (Figure 5.2b), apparent weight loss occurs in PVDF/DMF -based polymer electrolytes below 300 °C but not in pure PVDF. To understand the mechanism behind this, TGA tests were further performed in PVDF/$LiClO_4$ and PVDF/DMF binary membranes (Figure 5.3).

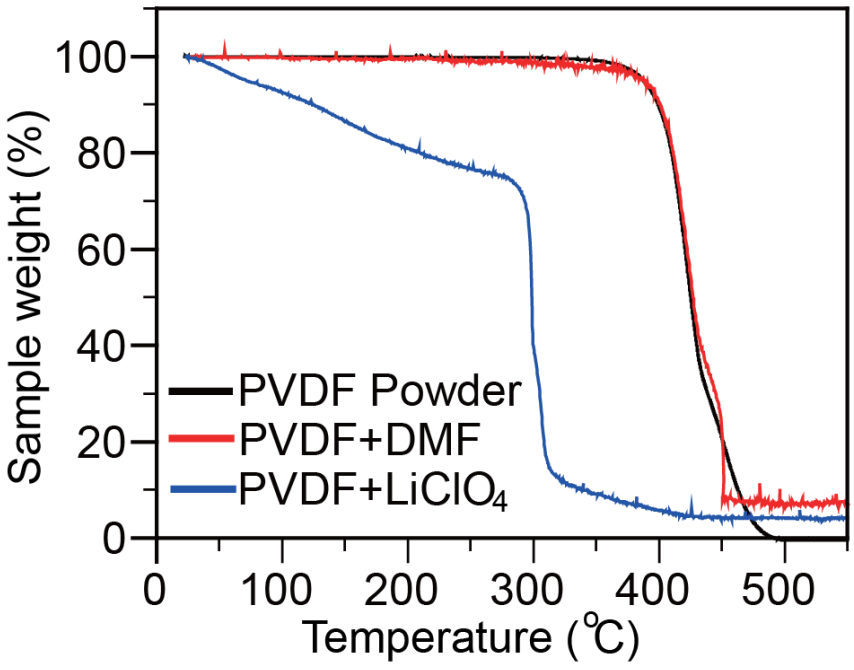

Figure 5.3. TGA curves of PVDF powder, PVDF polymer electrolyte without $LiClO_4$ vacuum dried under 60 ºC and PVDF/$LiClO_4$ membrane without DMF.

The $LiClO_4$-free PVDF/DMF membrane shows significant weight loss at 400 °C, similar to pure PVDF, but the DMF-free PVDF/$LiClO_4$ film shows remarkable weight loss at 300 °C similar to the polymer electrolyte. Therefore, the reduced thermal stability should be a result of $LiClO_4$, which is a well-known oxidant and accelerates the decomposition of PVDF. Nevertheless, stability up to 300 °C is still attractive for lithium batteries. To further determine the quality of DMF in different PVDF polymer electrolytes, 1H NMR test was carried out. The two peaks for DMF are located at 2.7 and 8.0 ppm (Figure 5.2c). Quantitative analysis show that the amount of DMF left are 23.6, 6.3, and 3.3 wt % for sample vacuum-dried at 60, 80, and 100 °C, respectively (Table 5.1).

Table 5.1. Relationship between vacuum dried temperature, DMF content, and ionic conductivity.

Vacuum Dried T (°C)	DMF Content (wt. %)	Ionic Conductivity (S/cm)
60	23.6	1.2×10^{-4}
80	6.3	2×10^{-6}
100	3.3	1×10^{-6}

To further understand the effect of DMF on PVDF/DMF-based polymer electrolytes compared with pure PVDF powders, X-ray diffraction (XRD) and Raman characterizations were also carried out. Although PVDF itself shows two small peaks at 18.5° and 20.1°, which corresponds to α-phase PVDF[114] these two peaks do not exist in PVDF polymer electrolyte membrane. Furthermore, these two peaks also vanish both in PVDF/DMF and PVDF/$LiClO_4$ binary membrane, indicating that both the DMF plasticizer and $LiClO_4$ amorphorize the film (Figure 5.2d). The peak at 38.5° and 44.8° come from the aluminum substrate. The existence of

DMF and $LiClO_4$ are also clearly shown in the Raman spectrum (Figure 5.4), as indicated by peaks at 869, 1105, 1421, and 1443 cm−1 for DMF[115] and 935 cm^{-1} for $LiClO_4$[116].

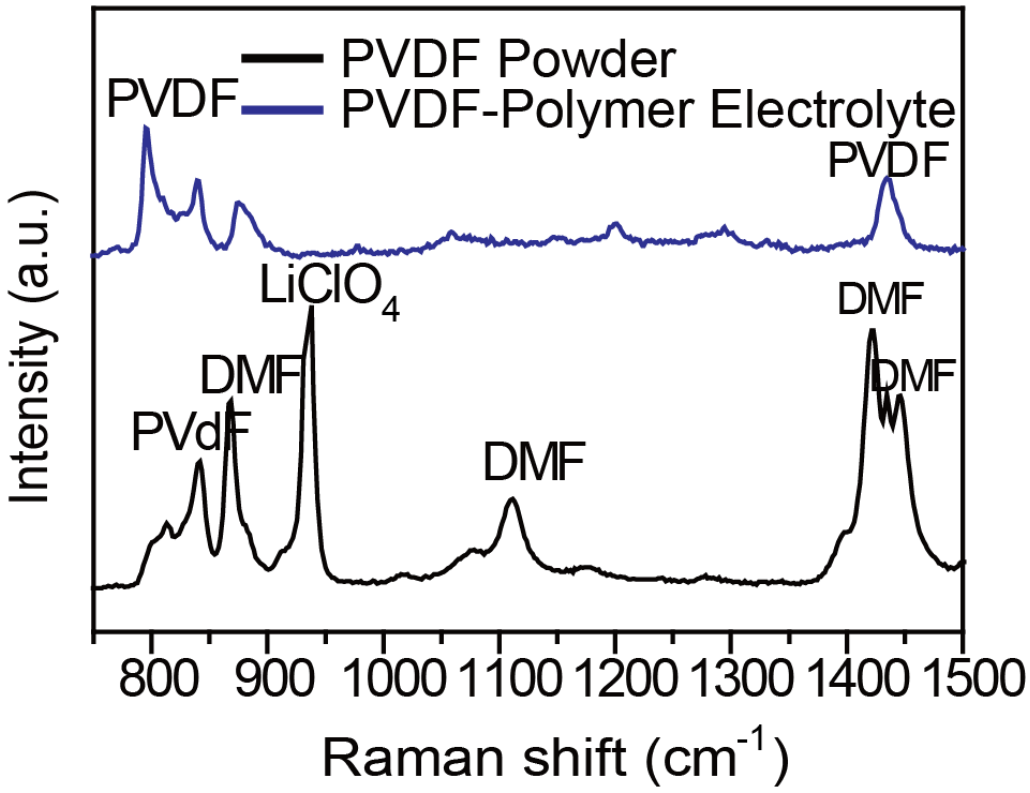

Figure 5.4. Raman spectra of PVDF/DMF polymer electrolyte and PVDF powder.

5.3 Electrochemical Characterizations

To understand the effect of DMF amount on PVDF/DMF polymer electrolyte conductivity, the ionic conductivities of PVDF/DMF polymer electrolytes at various temperatures were investigated by electrochemical impedance spectroscopy (EIS) measurements in a stainless steel/ PVDF/DMF-based polymer electrolyte/stainless steel configuration. The corresponding Nyquist plots at room temperature are presented in Figure 5.5.

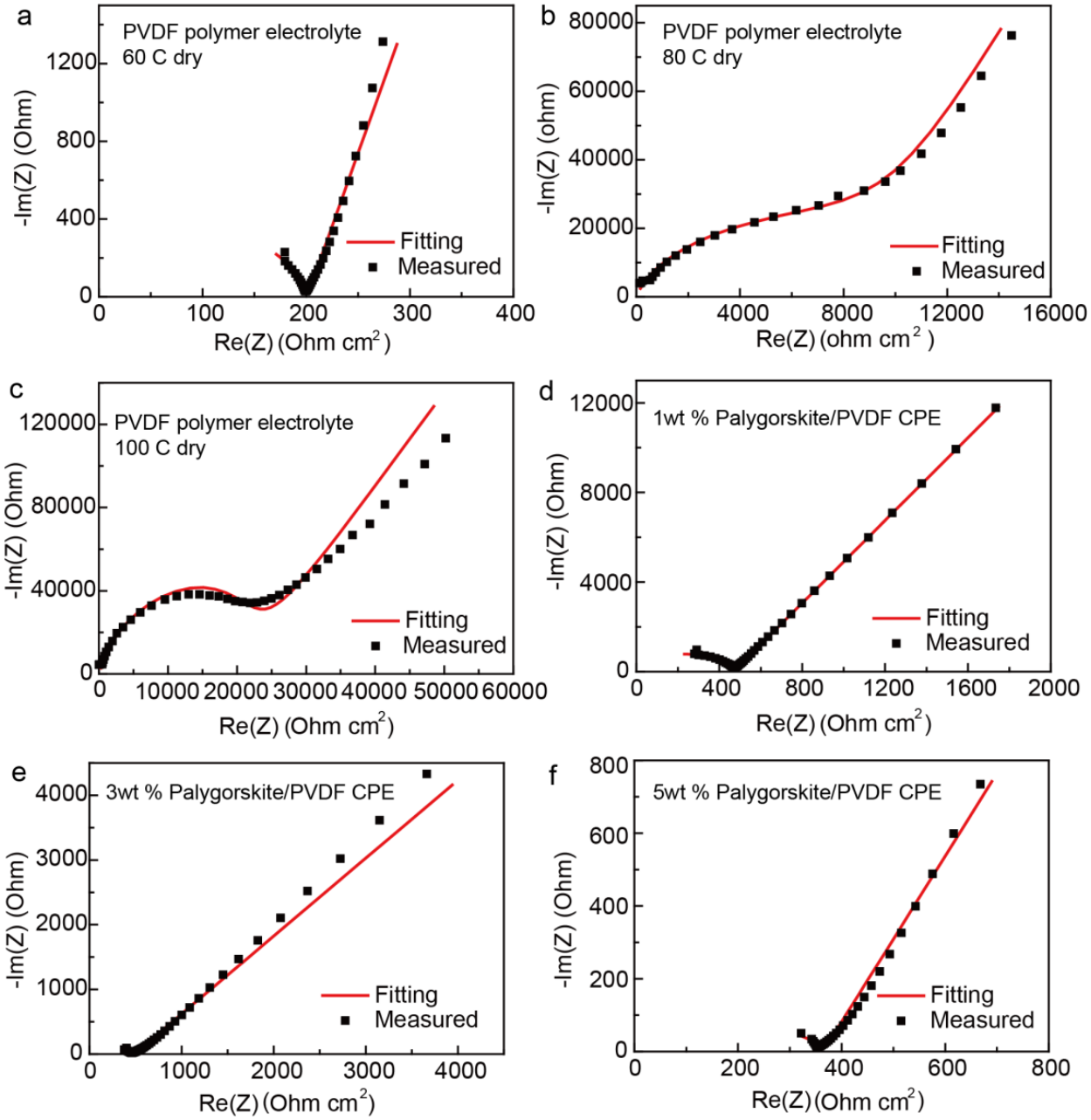

Figure 5.5. EIS for (a) 60 ℃ vacuum dried PVDF/DMF polymer electrolyte membrane (b) 80 ℃ vacuum dried PVDF/DMF polymer electrolyte membrane (c) 100 ℃ vacuum dried PVDF/DMF polymer electrolyte membrane (d) 1 wt% palygorskite PVDF/DMF CPE (e) 3 wt% palygorskite PVDF/DMF CPE and (f) 5 wt% palygorskite PVDF/DMF CPE.

Then ionic conductivities σ are calculated based on four samples at each drying temperature (Figure 5.6a). At room temperature, the ionic conductivity of PVDF/DMF polymer electrolyte vacuum-dried at 25 °C reaches 1.4×10^{-4} S/cm, which is similar to 1.2×10^{-4} S/cm for 60 °C sample, consistent with previous reports[117]. A sudden drop is observed between drying temperature of 70 and 80 °C, where conductivities decreases from 1.2×10^{-4} to 2.0×10^{-6} S/cm, and it further decreases to 1.1×10^{-6} S/cm for samples dried at 100 °C. This is consistent with the decreasing concentration of DMF in the electrolyte upon heating. The sudden drop between 70 and 80 °C indicates that DMF concentration decreases to a level lower than a critical threshold. The DMF concentration also affects the activation energy of ion transport. As shown in σ versus T plot in Figure 5.6b, the activation barriers are 0.39, 0.42, 0.64, and 0.63 eV for RT, 60, 80, and 100 °C dried samples. This indicates that high DMF content also reduces activation barrier to facilitate ion transport. These results indicate that DMF is critical to the ionic conductivity of such PVDF/DMF-based polymer electrolyte. At a weight content of 23.6%, the polymer electrolyte can be considered as a gel electrolyte or a hybrid solid/liquid electrolyte too.

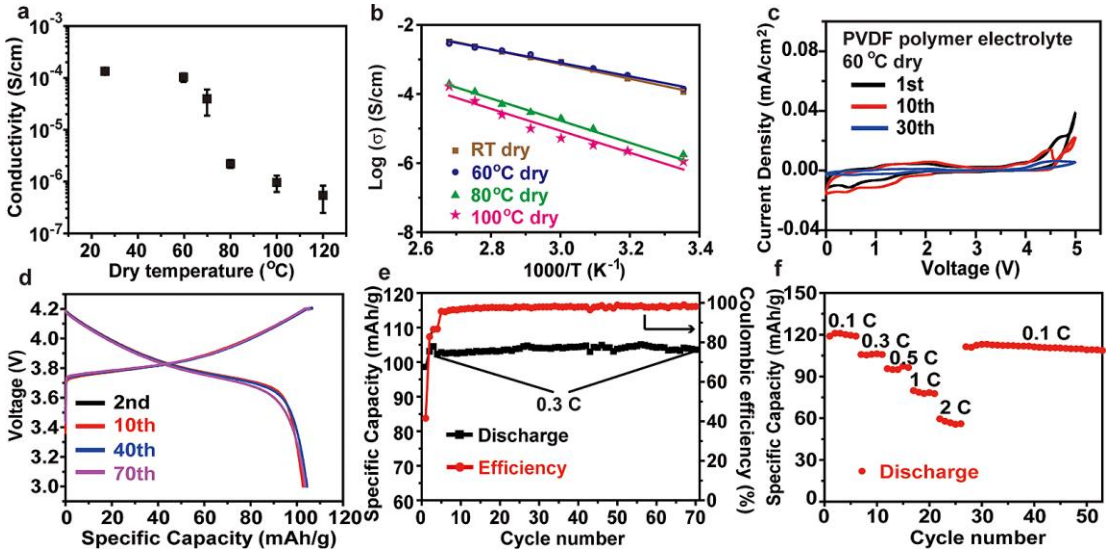

Figure 5.6. Electrochemical characterizations of PVDF/DMF polymer electrolyte. (a) The conductivities of PVDF/DMF polymer electrolytes as a function of vacuum-dried temperatures. (b)

Arrhenius plots of the PVDF/DMF based polymer electrolytes. (c) Cycle voltammetry curve of PVDF/DMF polymer electrolyte dried at 60 °C in vacuum. (d) Typical charge−discharge curves of NMC 111/PVDF-DMF/Li cells between 4.2 and 3.0 V at 0.3 C. (e) Cycle performance of a NMC 111/PVDF/DMF polymer electrolyte/Li cell at 0.3 C (1 C = 150 mA/g). (f) Power capability of such NMC111/PVDF-DMF/Li cell between 0.1 and 2 C rates.

To figure out how the DMF plasticizer affects electrochemical stability, cyclic voltammetry is performed at room temperature for PVDF/DMF polymer electrolyte samples dried at 60 °C. No obvious oxidation starts until 4.7 V versus Li/Li^+, indicating that the PVDF/DMF /$LiClO_4$ membrane can be stable with 4 V NMC cathodes (Figure 5.6c). To further evaluate their electrochemical performance, cells with $Li(Ni_{1/3}Mn_{1/3}Co_{1/3})O_2$ cathode (NMC 111), Li metal anode, and PVDF/DMF polymer electrolyte dried at 60 °C are assembled. The average thickness of PVDF/DMF electrolyte is 100 μm. The active material is around 1.6 mg/cm^2. All the battery tests are operated at 25 °C. The PVDF/DMF polymer electrolyte-cells are cycled between 4.2 and 3.0 V at 0.1 C (15 mA/g) for three cycles first, followed by 0.3 C for 70 cycles. In charging, a constant voltage step with a cutoff of C/20 is added at 4.2 V (Figure 5.6d). The discharge capacity slightly increases from 98.6 mA/g in cycle 1 to a peak value of 105.1 mA/g in cycle 58 and remains at 103.6 mAh/g at cycle 70 (Figure 5.6e). The specific capacity is also close to results in liquid electrolyte, which is ~125 mAh/g between 3.0 and 4.2 V (Figure 5.7a,b). The power capability test shows that the specific capacity remains at 106.2, 97.4, 79.8, and 59.5 mAh/g at 0.2, 0.5, 1, and 2 C, respectively, which indicates reasonable rate performance of the PVDF/DMF polymer electrolyte cell.

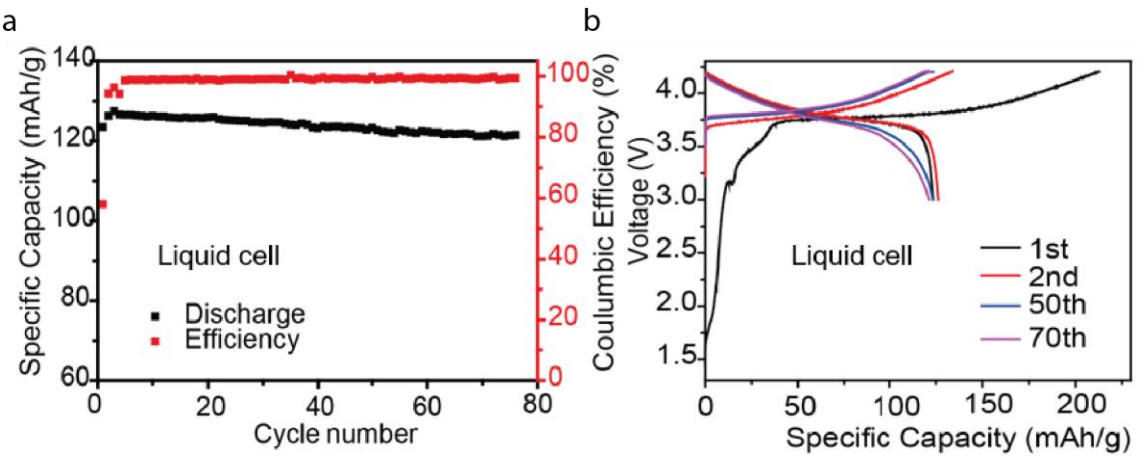

Figure 5.7. Cycling performance for liquid cell. (a) Cycling performance at 0.3 C of liquid electrolyte cell. (b) Typical charge−discharge curves of liquid electrolyte cell.

5.4 Addition of Palygorskite Nanowires for Performance Improvements

5.4.1 Motivation

Although DMF helps to increase ionic conductivity, the mechanical robustness of PVDF/DMF SPE membrane is seriously weakened (Fig.4.9a), which will comprise its capability again lithium dendrite and deteriorate battery safety [118]. To solve this issue, palygorskite nanowires are added re added into the solid electrolyte membranes as reinforcing elements to improve the mechanical properties. There are two reasons to choose this material. First, its nanowire shape can help form an interconnected and mechanically strong network. Second, palygorskite is a natural product with ultralow cost, much less than that to synthesize SiO_2, Al_2O_3 or ceramic electrolyte (e.g. LLZO) nanowires. TEM characterizations show that palygorskite nanowires have a diameter of ~50 nm and a length of ~1 μm (Figure 5.8a). It is also crystalline based on electron diffraction data (inset in Figure 5.8a). To prepare PVDF/DMF/palygorskite CPEs, palygorskite nanowires were added into DMF/PVDF solution with target weight percentage.

The cross-section SEM picture of palygorskite-modified membrane in Figure 5.8b further illustrates that palygorskite nanowires blend into the PVDF polymer matrix.

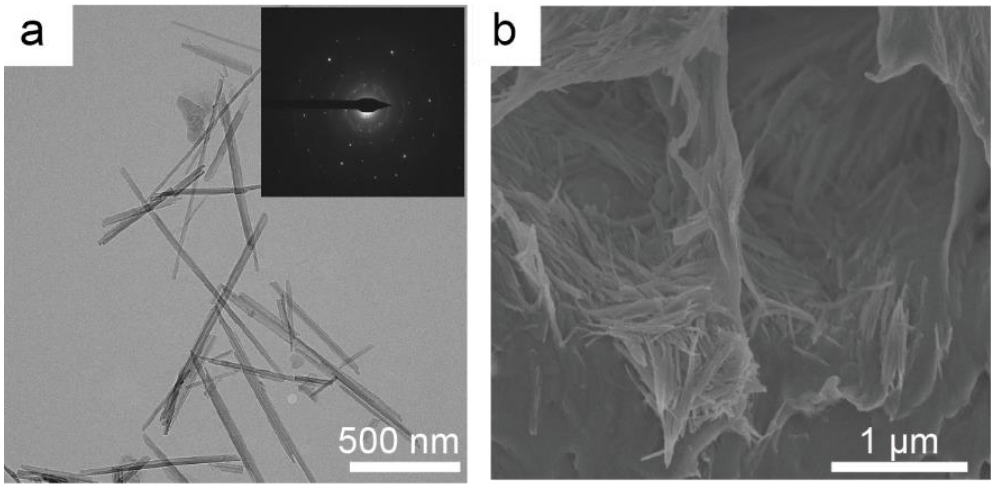

Figure 5.8. Electron microscopies of palygorskite nanowires. (a) A TEM image of palygorskite nanowires and corresponding electron diffraction pattern. (b) Cross-sectional SEM image of PVDF/palygorskite-CPE, showing that palygorskite nanowires blended into the PVDF matrix.

5.4.2 Mechanical and Thermal Stability with Palygorskite Nanowires

The enhancement in mechanical properties is demonstrated as the stress−strain responses of pure PVDF/DMF polymer electrolyte and PVDF/5 wt % palygorskite CPE at a constant tensile strain rate of 0.001/s, as shown in Figure 5.10a. Adding 5 wt % palygorskite nanowires to the PVDF/DMF polymer electrolyte not only significantly improves the Young's modulus from 9.0 to 96 MPa of membrane but also increases the yield stress by 200% (4.7 MPa versus 1.5 MPa). Although this value is much less than the threshold proposed by Newman[119] (shear modulus of 6.8 GPa), previous studies have shown that even lower Young's modulus of electrolyte can help suppress the dendrite growth to realize long-term cycling stability[59, 120]. To unveil the

connection between dendrite suppression and the addition of palygorskite nanowires, shorting time during lithium plating and SEM characterizations are carried out (Figure 5.9).

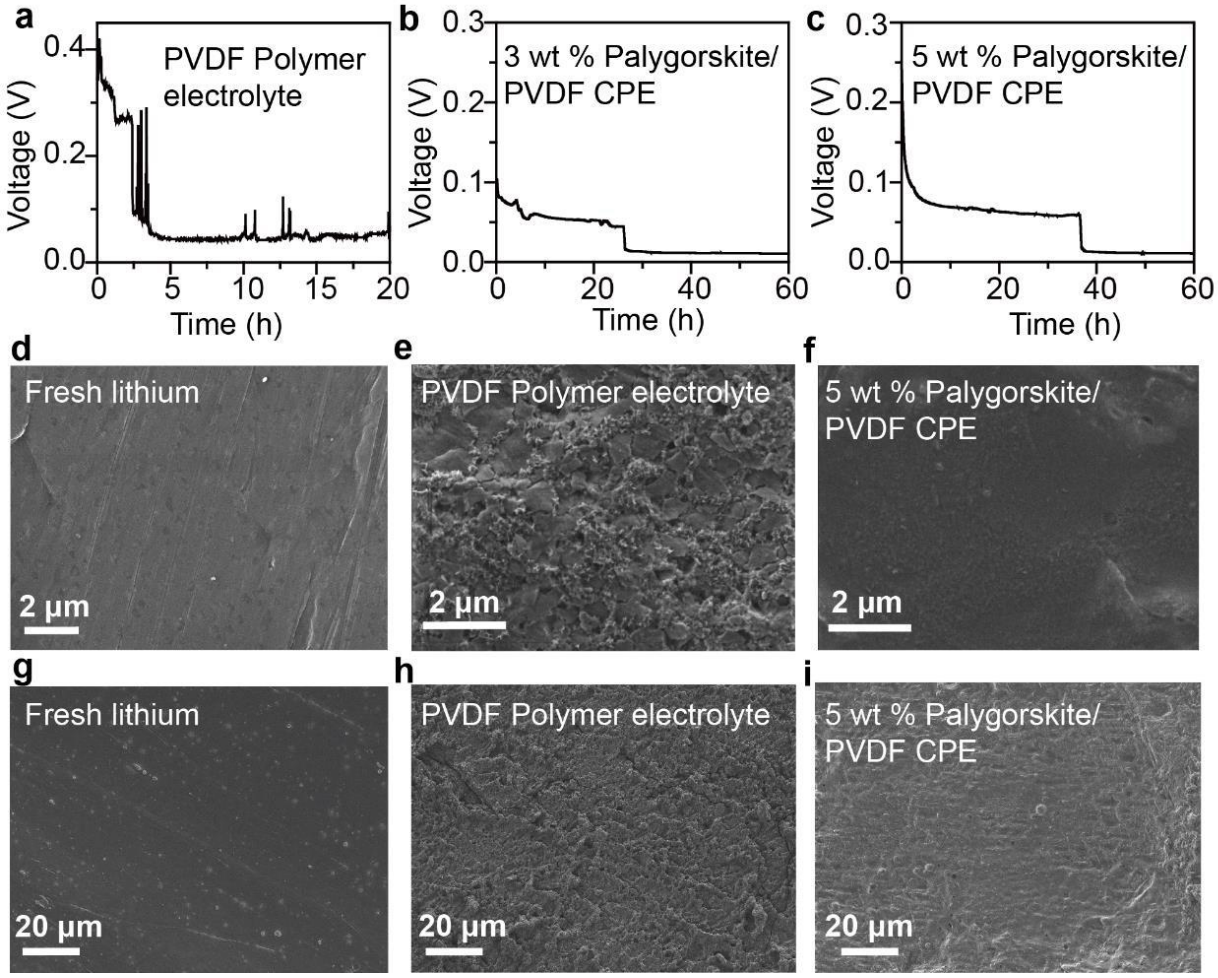

Figure 5.9. Li symmetric cell characterizations of PVDF/DMF-based electrolytes. (a-c) Voltage profile of (a) Li |PVDF/DMF Polymer electrolyte| Li cells, (b) Li |3 wt % Palygorskite/PVDF/DMF CPE| Li cells and (c) Li |5 wt % Palygorskite/PVDF/DMF CPE| Li cells with a constant current density of 0.3 mA/cm^2. (d-f) SEM images of the surface of the Li electrode (d) before Li deposition, (e) the Li electrode obtained from a Li |PVDF/DMF Polymer electrolyte| Li cell until shorting, and (f) from a Li |5 wt % Palygorskite/PVDF/DMF CPE| Li cell after applying a current density of 0.3 mA/cm^2 after the same time as that in (e). (g-i) Zoom-out SEM images of the surface of the Li electrode.

When 0.3 mA/cm2 is applied, the Li/Li cell with pure PVDF/DMF polymer electrolyte is shorted after only 3.8 h, which is equivalent to 1.14 mAh/cm2. Meanwhile, the time for 3 wt % palygorskite/PVDF/DMF CPE and 5 wt % palygorskite/PVDF/DMF CPE are 26 and 36 h, respectively, corresponding to 7.8 and 10.8 mAh/cm2, respectively. Moreover, the lithium surface with CPE is also much smoother than that without palygorskite addition (Figure 5.9f). This indicates that the addition of palygorskite nanowires in such CPE can suppress the growth of lithium dendrites. In our own full cell cycling, we also find that the addition of palygorskite nanowires enhances cycling life, as discussed below, but it should be noted that further investigations should be carried out to fully understand its capability to suppress dendrite, especially at high currents. Mechanical-wise, it is impressive that adding such a small amount of palygorskite can greatly improve the mechanical properties. To unveil the mechanisms behind, both theoretical and numerical analyses were performed. The enhanced stiffness of this composite can be mainly attributed to the matrix−nanowires interaction. In Figure 5.10b, analysis based on the Mori-Tanaka's theory indicates that with 5 wt % palygorskite the effective modulus E_{eff} can reach eight times that of pure PVDF matrix[121], slightly smaller than measured results of 10.7 times. The deviation is possibly due to the nanowire−nanowire interaction in a cross-linked network through nanowelding junctions, van der Waal interaction, and chemical bonds. To verify the effect of such internanowire interaction, Monte Carlo and finite element simulations were carried out to generate a network of 5 wt % randomly distributed nanowires, and nanowire deformation with the network externally stretched is calculated, as shown in Figure 5.10c. A significant portion of axial strain is undertaken by wire−wire junction, which indicates enhanced stiffness by forming wire−wire junctions as hinges. Therefore, we attribute both the nanowire−polymer interaction and the internanowire connections to be responsible for the

increased stiffness of modified PVDF/DMF polymer electrolyte membrane. Additionally, the composite electrolyte shows significantly increased fracture strain of 180%, which is twice that of pure PVDF/DMF polymer electrolyte membrane (90%) (Figure 5.10a). This toughening effect should be due to strong interfacial adhesion between nanowires and PVDF matrix[122], resisting nanowire pull-out when composite fracturing. Therefore, the additives of palygorskite nanowires allow the PVDF/DMF-based membrane to be mechanically robust, underpinning safety of solid electrolyte.

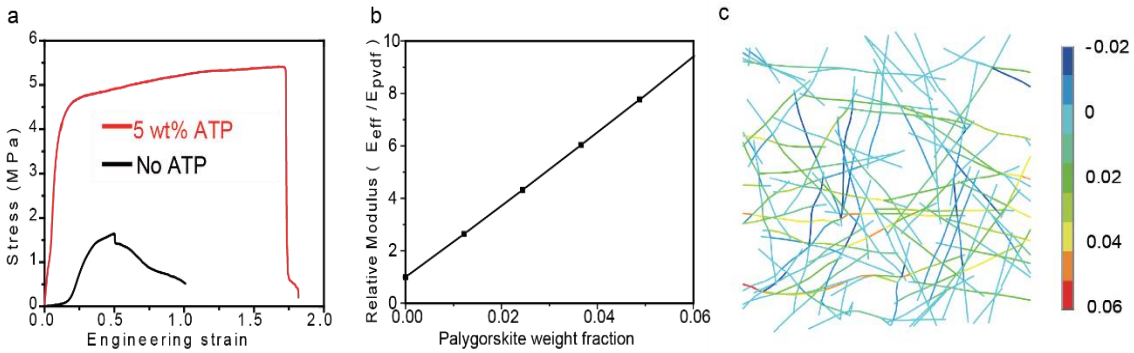

Figure 5.10. Mechanical properties of PVDF/DMF-based electrolytes. (a) Stress−strain relations of different PVDF/DMF-based membranes under uniaxial tension at strain rate of 0.001/s. (b) Effective Young's modulus of composite membrane with randomly distributed nanowire fillers as a function of weight fraction. (c) Axial strain contour of the deformed nanowire network at an average tensile strain of 5%.

Safety and nonflammability are also crucial to evaluate solid electrolytes. To prove the safety of PVDF/DMF-based solid electrolytes, nailing test was conducted. In the experiment, a pouch cell with PVDF/DMF CPE, NMC cathode and lithium anode was assembled, embedded with thermocouple to detect the real-time temperature changes. The cell was pre-charged to 4.0 V

and a stainless steel syringe needle was used to penetrate the pouch to mimic short circuit (Figure 5.11a). As shown in Figure 5.11c, after puncturing, the cell voltage decreased to 17 mV, but there is no significant increase in cell temperature showing limited safety hazards. Besides puncturing, PVDF/DMF film vacuum dried at 60 ^{o}C is also not ignitable under fire, as shown in Figure 5.11d. In contrast, pure PEO electrolyte can be easily ignited with fire. Such significant contrast further demonstrates the enhanced safety of PVDF/DMF-based solid electrolyte.

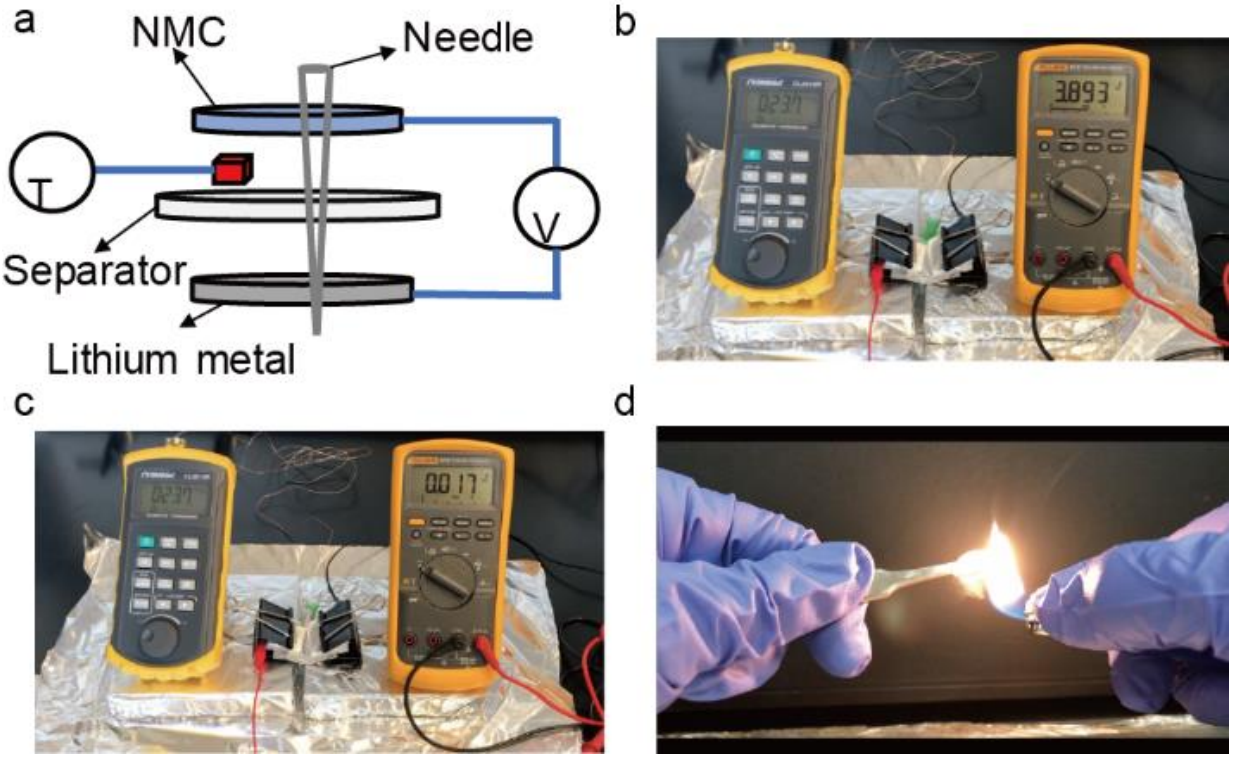

Figure 5.11. Safety tests for the PVDF/DMF-based electrolytes. (a) The Schematic diagram of the nailing test. (b) NMC/PVDF/DMF-palygorskite CPE/Li pouch cell before (b) and after (c) puncture. (d) Ignition test of PVDF/DMF film vacuum dried at 60 ^{o}C. The film does not catch fire when ignited.

5.4.3 Electrochemical Characterizations with Palygorskite Nanowires

To further evaluate the effect of palygorskite nanowires on PVDF/DMF-based CPEs, the ionic conductivities of PVDF/DMF CPEs with different weight percentages of paylgorskite

nanowires were investigated. All samples are dried in vacuum oven at 60 ºC for 24h, and four samples were tested for each weight percentage. The ionic conductivities of 1 wt %, 3 wt % and 5 wt % PVDF/DMF/palygorskite CPEs reach 1.4×10^{-4}, 1.7×10^{-4} and 8.3×10^{-5} S/cm, respectively. It is likely that due to the high aspect ratio of nanowires, only 1-3 wt % is enough to form a network and facilitate ionic transport, while adding more will block ion transport and thus reduce ionic conductivity. The corresponding activation barriers are 0.46, 0.32, and 0.36 eV, respectively (Figure 5.12), similar to the samples without palygorskite nanowires (Figure 5.6b).

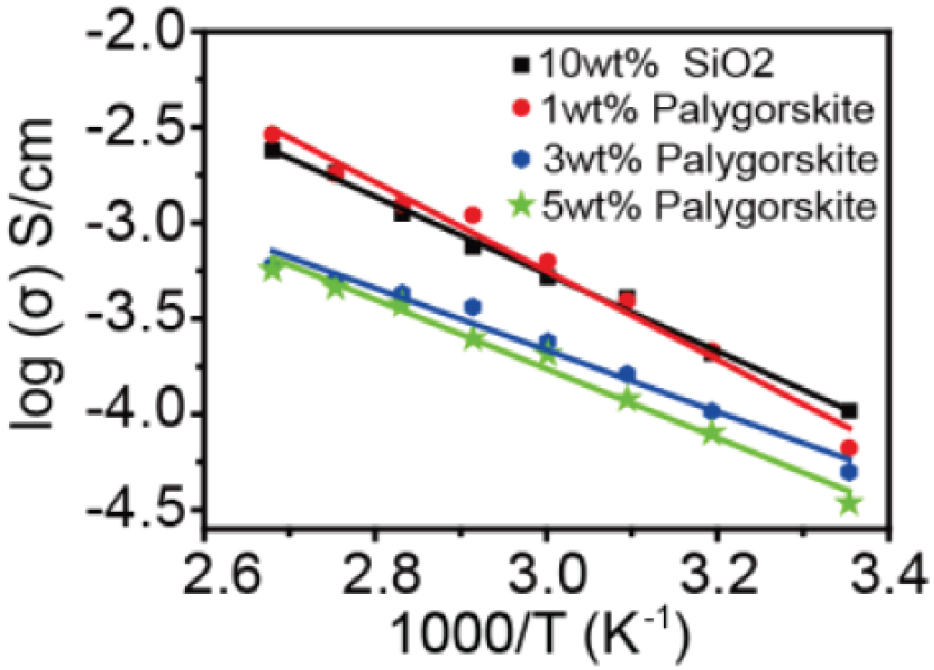

Figure 5.12. Arrhenius plots of PVDF/DMF based composite electrolytes with different content of ceramic fillers.

Also, the lithium ion transference number (t_{Li+}) of PVDF/DMF/palygorskite and PVDF/DMF polymer electrolytes were measured through potentiostatic polarization (PP) method (Figure 5.13)[123]. A small constant potential (8.7mV) was applied on PVDF/DMF-based polymer electrolytes between two lithium electrodes which leads to a decrease of the initial current

(I_0) until a steady-state current (I_{SS}) flowing through the cell. R_0 and R_{SS}, representing the charge-transfer resistance before and after the polarization of the system respectively, which were obtained by impedance spectra of the cell in the frequency range from 1 MHz to 0.1Hz with an oscillation voltage of 10 mV. t_{Li+} was calculated using the following equation[41]:

$$t_{Li^+}=\frac{I_{SS}(\Delta V-I_0R_0)}{I_0(\Delta V-I_{SS}R_{SS})}$$

As shown in Figure 5.13a, the interfacial resistance of PVDF/DMF polymer electrolyte increases from 222 to 301 Ohm after polarization. During the polarization process, the steady-state current (I_{SS}) decreases to a steady value of 0.0126 mA from the initial current (I_0) of 0.0287 mA. Therefore, the calculated t_{Li+} for the PVDF/DMF CE is 0.21. Similarly, the calculated t_{Li+} for the PVDF/DMF/5wt% palygorskite CPE and PVDF/DMF/3wt% palygorskite CPE is 0.54 and 0.31 respectively.

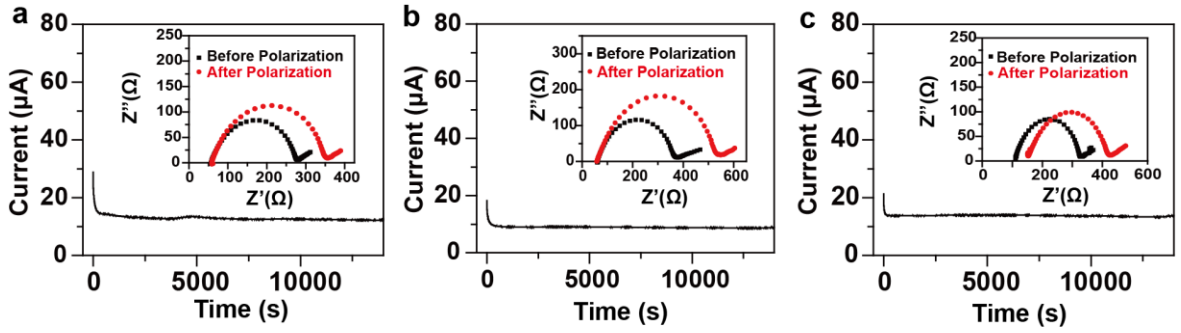

Figure 5.13. Current-time profile of PVDF/DMF-based electrolytes. (a) Li| pure PVDF/DMF |Li symmetric cell, (b) Li| PVDF/DMF/3 wt % palygorskite CPE |Li symmetric cell and Li| PVDF/DMF/5 wt % palygorskite CPE |Li symmetric cell after applying a DC voltage of 10 mV for determining Li^+ transfer number. The inset shows the Nyquist impedance spectra of the cell before and after polarization.

The enhanced t_{Li+} is likely due to two reasons. First, with the addition of inorganic fillers, the local chains of polymer can be relaxed and the segment motion is promoted under the

interaction of inorganic fillers and polymer chains, as a result, the mobility of Li ions and t_{Li+} can be enhanced[124]. Apart from stabilizing the amorphous state of the polymer, the exposed metal cations on the surface of palygorskite ceramic nanowires also interacts with ClO_4^- through Lewis acid–base interactions[125]. So, there may be interaction between the palygorskite and anions in the lithium salt which immobilize anion and enhance transference number. This assumption is confirmed through FTIR test.

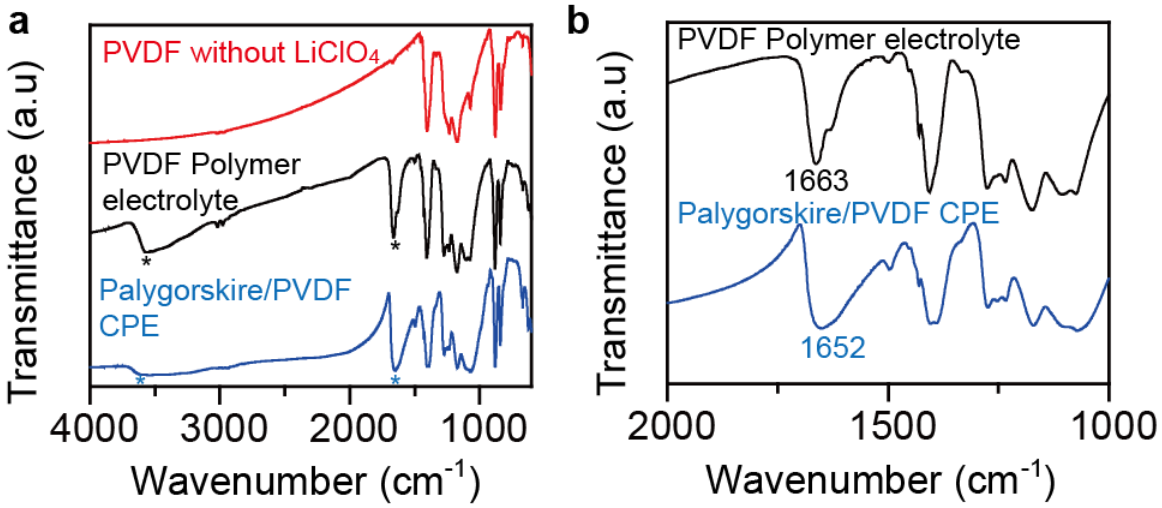

Figure 5.14. (a) FTIR spectra of the PVDF/DMF polymer electrolyte, PVDF/DMF polymer electrolyte without $LiClO_4$ and PVDF/DMF/Palygorskite CPE at 4000−600 cm^{-1}. (b) Zoom-in FTIR spectra of the PVDF/DMF polymer electrolyte membrane and PVDF/DMF/Palygorskite CPE membrane at 2000−1000 cm^{-1}.

The ClO_4^- peaks at 1663 cm^{-1} in PVDF polymer electrolyte shift to 1652 cm^{-1} in PVDF/DMF/Palygorskite CPEs. The shape of the peak at 3559 cm^{-1} also changes. These shifts in FTIR can be attributed to the interaction between palygorskite nanowires and the ClO_4^- anion, which alters the vibration modes in ClO_4^-. Such interactions enhances dissociation of $LiClO_4$, traps ClO_4^- on

nanowire surface, and thus increases transference number of Li^+. This has been observed in $Mg_2B_2O_5$[126] and $Li_7La_3Zr_2O_{12}$[124].

To further examine the electrochemical stability of PVDF/DMF/palygorskite CPEs, cyclic voltammetry is carried out first, as shown in Figure 5.15.

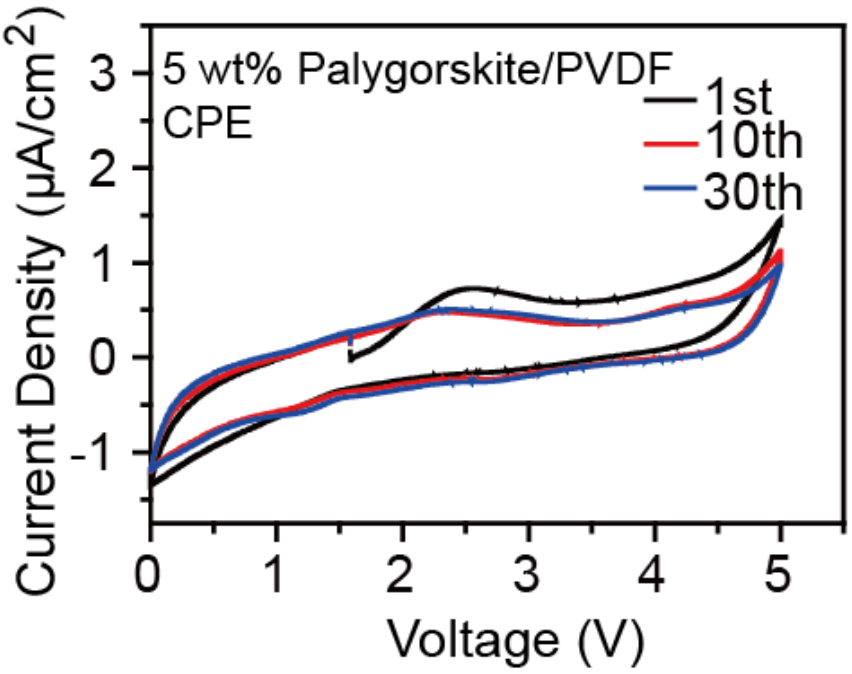

Figure 5.15. Cyclic voltammetry curve of 5 wt% Palygorskite/PVDF/DMF CPE with a scan rate of 10 mV/s.

The cathodic current density at 0 V vs. Li^+/Li is ~ 1 $\mu A/cm^2$, much smaller than that in pure PVDF/DMF membrane (Figure 5.6c). Since palygorskite nanowire is a well-known absorbent for organic solvent[113], they could trap DMF and reduce its reduction rate. Furthermore, full cell tests were performed with 5 wt % palygorskite nanowire fillers, and steady cycling is achieved too (Figure 5.16a). The cycling protocol is the same as pure PVDF/DMF polymer electrolyte, 0.1 C for three cycles, followed by 0.3 C between 4.2 and 3.0 V. At 0.3 C, the discharge capacity rises

from 117.6 mAh/g to 121.4 mAh/g in the first 5 cycles and retain 118.1 mAh/g after 200 cycles at 0.3 C. (Figure 5.16b), which shows that PVDF/DMF/Palygorskite CPEs work steadily in the cell.

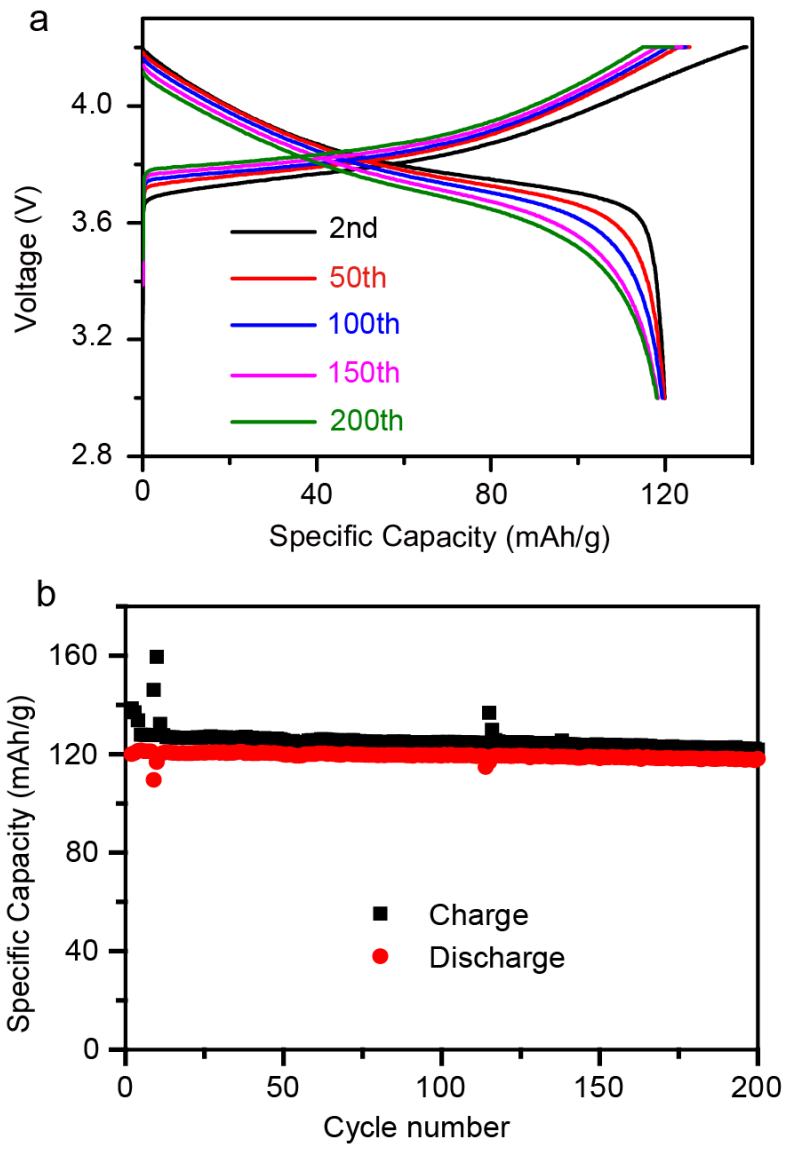

Figure 5.16. (a) Voltage profile and (b) cycling performance of NMC| PVDF/DMF/5 wt % palygorskite CPE |Li cell (1C = 150 mA/g).

Similarly, NMC/Li cells with 1 and 3 wt% of palygorskite nanowires were also tested for comparison. While similar cycling stability can be obtained, we noticed that cells with no or lower amount of palygorskite nanowires tend to have microshorting in a smaller number of cycles (e.g.

~90 cycles for 1 wt% and ~130 cycles for 3 wt%, Figure 5.17). Meanwhile, 5 wt% sample shows stability over 200 cycles and ongoing. This also indicates that the addition of palygorskite nanowires in such CPE can suppress the penetration of lithium dendrite so that longer cycle life can be achieved.

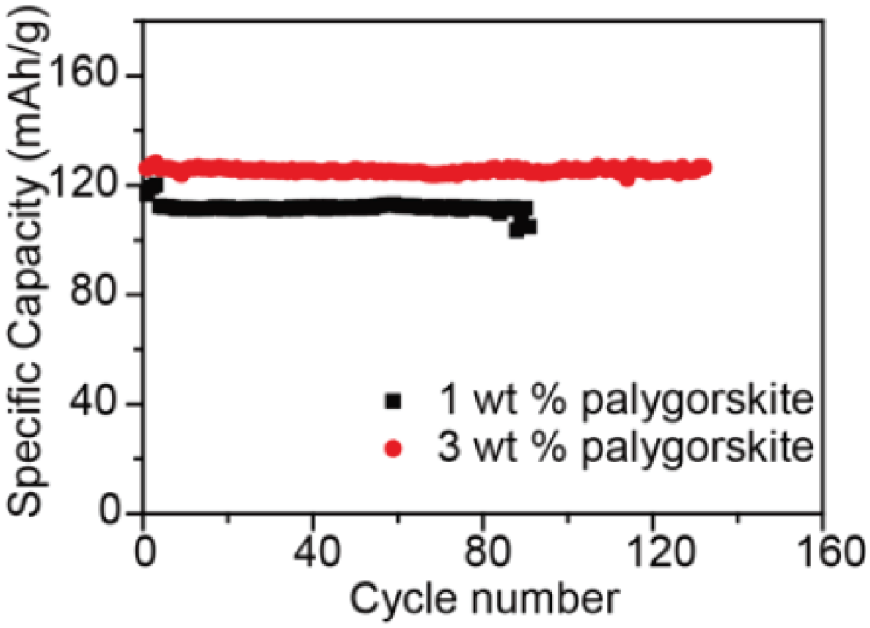

Figure 5.17. Discharge specific capacity vs cycle number (1C = 150 mA/g) of 1, 3 wt % PVDF/DMF/palygorskite CPE cell.

However, the performance of lithium/lithium symmetric cells (Figure 5.18) is not as good as the NMC 111 | PVDF/DMF/palygorskite CPE |Li cells. A possible reason is that in lithium/lithium symmetric cells, lithium metal is oxidized first at one electrode, which results in fresh new lithium metal surface that directly exposes to DMF, which may accelerate the degradation of cycling performance. This was also observed in past literature[127]. In the future, we will modify lithium surface (e.g. passivation layer[128, 129]), or replace DMF with more stable plasticizers, to address this issue.

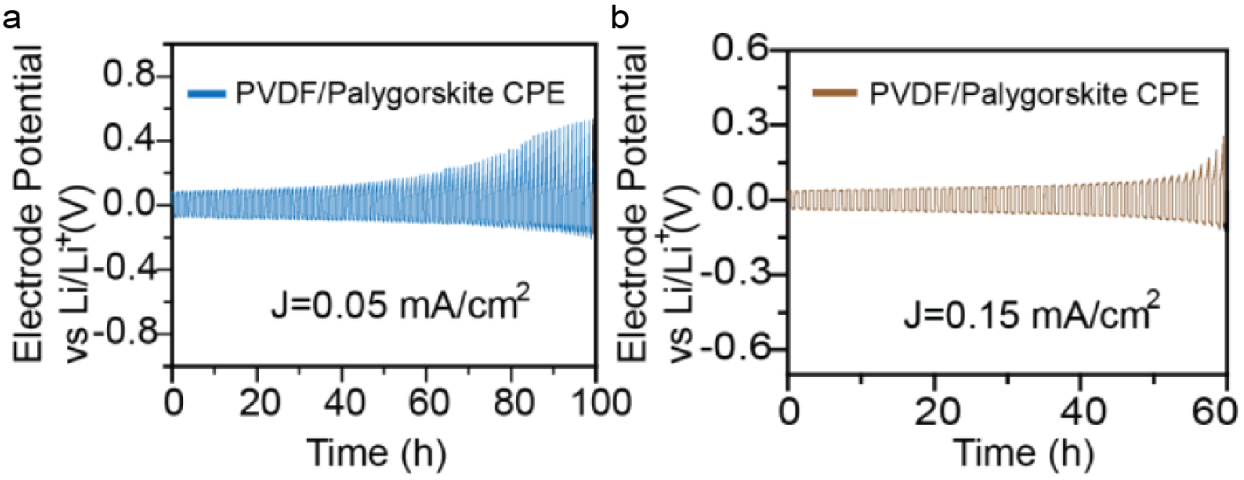

Figure 5.18. Galvanostatic cycles with a constant current density of (a) 0.05 mA/cm^2 and (b) 0.15 mA/cm^2 for Li |PVDF/DMF/palygorskite CE| Li cells at 25 °C.

5.5 Conclusion

Solid electrolytes are crucial for the development of solid-state batteries. Among different types of solid electrolytes, Polyethylene oxide (PEO)-based polymer electrolytes (SPE) have attracted extensive attentions owing to their excellent flexibility and easiness for processing. However, their relatively low ionic conductivities and electrochemical instability above 4V limit their applications in batteries with high energy density. Our choice for the replacement is PVDF/DMF composite polymer.

In this chapter, we have proposed the poly(vinylidene fluoride) (PVDF) polymer electrolytes with organic plasticizer DMF, which possess compatibility with 4V cathode and high ionic conductivity (1.2×10^{-4} S/cm) at room temperature. We also revealed the importance of plasticizer content to the ionic conductivity. To address weak mechanical strength of the PVDF electrolyte with plasticizer, we introduced palygorskite ($(Mg,Al)_2Si_4O_{10}(OH)$) nanowires as a new ceramic filler to form composite solid electrolytes (CPE), which greatly enhances both stiffness

and toughness of PVDF/DMF-based polymer electrolyte. With 5 wt % of palygorskite nanowires, not only the elastic modulus of PVDF/DMF CPE increases from 9.0 MPa to 96 MPa, but also its yield stress is enhanced by 200%. Moreover, numerical modeling uncovers that the strong nanowire-polymer interaction and crosslinking network of nanowires are responsible for such significant enhancement in mechanically robustness. The addition of 5% palygorskite nanowires also enhances transference number of Li^+ from 0.21 to 0.54, due to interaction between palygorskite and ClO_4^- ions. We further demonstrate full cells based on $Li(Ni_{1/3}Mn_{1/3}Co_{1/3})O_2$ (NMC111) cathode, PVDF/DMF/palygorskite CPE, and lithium anode, which can be cycled over 200 times at 0.3 C, with 97% capacity retention. Moreover, the PVDF matrix is much less flammable than PEO electrolytes. Our work illustrates that the PVDF/DMF/palygorskite CPE is a promising electrolyte for solid state batteries.

Chapter 6 Thesis Conclusion

Since the first commercialization in 1991 by Sony, lithium-ion batteries (LIBs) have risen rapidly as a new form of energy storage device. LIB plays a very important role in portable electronics, and its demands in electric vehicles and grid-level energy storage are increasing dramatically in recent years. However, the state-of-the-art battery technology does not well satisfy all the applications above. The next-generation batteries with better safety, higher energy density, faster charge/discharge rate, longer cycle life are desired.

In this thesis, we first demonstrate the fabrication of a flexible composite electrolyte composing of a vertically aligned and connected ceramic particles and a polymer, to avoid the processing difficulty in ceramic electrolyte and low conductivity in polymer electrolyte. LATP and LAGP NPs in the polyethylene oxide (PEO) matrix are two examples to maximize the ionic conductivity, while maintaining the flexibility of the composite. Ice-templating technique is used to realize this vertically aligned structure, and its conductivity reaches 0.52×10^{-4} S/cm for LATP/PEO, and 1.67×10^{-4} S/cm for LAGP/PEO composite electrolytes, which are several times higher than that of the composite electrolyte with randomly dispersed LATP/LAGP NPs. Mechanical and thermal stabilities are also enhanced compared to the pure PEO electrolyte. The LFP-LAGP/PEO-Li cell reaching 148.7 mAh/g during the first discharge at 0.3C has over 95% capacity retention after 200 cycles. This method opens a new approach to optimize ion conduction in composite solid electrolytes for next-generation rechargeable batteries.

Polyether-based electrolytes such as PEO and PEG are electrochemically instable above 4 V, limiting their use with high voltage cathodes such as NMC for high energy density. The compatibility between polyether-based electrolyte and NMC cathodes that can be significantly improved by forming a 2 nm Al_2O_3 coating on NMC surface is presented. This nanoscale coating

dramatically improves the cathode electrolyte interphase and thus stabilizes PEG electrolyte with the NMC cathode. Adding Al_2O_3, the capacity remains at 84.7% after 80 cycles and 70.3% after 180 cycles. Whereas the capacity fades to less than 50% after only 20 cycles in bare NMC electrodes. This study opens new opportunity to develop safe electrolyte for lithium batteries with high energy density.

In the final part we propose a new polymer electrolyte, the poly(vinylidene fluoride) (PVDF) polymer electrolyte with organic plasticizer DMF, which possesses compatibility with 4V cathode and high ionic conductivity (1.2×10^{-4} S/cm) at room temperature. The importance of plasticizer content to the ionic conductivity is also revealed. To tackle the weak mechanical strength of the PVDF/DMF electrolyte with plasticizer, palygorskite ($(Mg,Al)_2Si_4O_{10}(OH)$) nanowires are introduced as a new ceramic filler to form composite solid electrolytes (CPE), which greatly enhances both stiffness and toughness of PVDF/DMF-based polymer electrolyte. With 5 wt % of palygorskite nanowires, the elastic modulus of PVDF/DMF CPE increases from 9.0 MPa to 96 MPa, and its yield stress is enhanced by 200%. Furthermore, numerical modeling indicates that the strong nanowire-polymer interaction and crosslinking network of nanowires are responsible for such significant enhancement in mechanically strength. The addition of palygorskite nanowires also enhances transference number of Li^+ from 0.21 to 0.54, due to interaction between palygorskite and ClO_4^- ions. We further demonstrate that the full cells composed of $Li(Ni_{1/3}Mn_{1/3}Co_{1/3})O_2$ (NMC 111) cathode, PVDF/DMF/palygorskite CPE, and lithium metal anode, can be cycled over 200 times at 0.3 C, with 97% capacity retention. Moreover, the PVDF matrix is much less flammable than PEO electrolytes. Our work illustrates that the PVDF/DMF/palygorskite CPE is a promising electrolyte for solid state batteries.

All the parts are contributing to utilize the solid electrolytes including polymer and ceramic electrolytes for the rechargeable solid-state batteries, with better safety, higher energy density and more stable cycling.

References

1. https://www.marketsandmarkets.com/Market-Reports/electric-vehicle-market-209371461.html.

2. Armand, M. and J.M. Tarascon, *Building better batteries.* Nature, 2008. **451**: p. 652.

3. Manthiram, A., et al., *Nanostructured electrode materials for electrochemical energy storage and conversion.* Energy & Environmental Science, 2008. **1**(6): p. 621-638.

4. Tarascon, J.M. and M. Armand, *Issues and challenges facing rechargeable lithium batteries.* Nature, 2001. **414**(6861): p. 359-367.

5. Huggins, R.A., *Advanced Batteries: Materials Science Aspects.* Springer, 2008.

6. Chen, S., et al., *High-Efficiency Lithium Metal Batteries with Fire-Retardant Electrolytes.* Joule, 2018. **2**(8): p. 1548-1558.

7. Ren, X., et al., *Localized High-Concentration Sulfone Electrolytes for High-Efficiency Lithium-Metal Batteries.* Chem, 2018. **4**(8): p. 1877-1892.

8. Fu, K., et al., *Flexible, solid-state, ion-conducting membrane with 3D garnet nanofiber networks for lithium batteries.* Proceedings of the National Academy of Sciences of the United States of America, 2016. **113**(26): p. 7094-7099.

9. Manthiram, A., X. Yu, and S. Wang, *Lithium battery chemistries enabled by solid-state electrolytes.* Nature Reviews Materials, 2017. **2**: p. 16103.

10. Quartarone, E. and P. Mustarelli, *Electrolytes for solid-state lithium rechargeable batteries: recent advances and perspectives.* Chemical Society Reviews, 2011. **40**(5): p. 2525-2540.

11. Lin, D., Y. Liu, and Y. Cui, *Reviving the lithium metal anode for high-energy batteries.* Nat Nano, 2017. **12**(3): p. 194-206.

12. Xu, W., et al., *Lithium metal anodes for rechargeable batteries.* Energy & Environmental Science, 2014. **7**(2): p. 513-537.

13. Whittingham, M.S., *Materials challenges facing electrical energy storage.* Mrs Bulletin, 2008. **33**(4): p. 411-419.

14. Xu, K., *Nonaqueous liquid electrolytes for lithium-based rechargeable batteries.* Chemical Reviews, 2004. **104**(10): p. 4303-4417.

15. Armand, M., et al., *Ionic-liquid materials for the electrochemical challenges of the future.* Nature Materials, 2009. **8**(8): p. 621-629.

16. Goodenough, J.B. and K.S. Park, *The Li-Ion Rechargeable Battery: A Perspective.* Journal of the American Chemical Society, 2013. **135**(4): p. 1167-1176.

17. Wu, H., et al., *Stable cycling of double-walled silicon nanotube battery anodes through solid-electrolyte interphase control.* Nat Nano, 2012. **7**(5): p. 310-315.

18. Kim, J.G., et al., *A review of lithium and non-lithium based solid state batteries.* Journal of Power Sources, 2015. **282**: p. 299-322.

19. Sun, Y.G., *Lithium ion conducting membranes for lithium-air batteries.* Nano Energy, 2013. **2**(5): p. 801-816.

20. Verma, P., P. Maire, and P. Novák, *A review of the features and analyses of the solid electrolyte interphase in Li-ion batteries.* Electrochimica Acta, 2010. **55**(22): p. 6332-6341.

21. Scrosati, B., J. Hassoun, and Y.-K. Sun, *Lithium-ion batteries. A look into the future.* Energy & Environmental Science, 2011. **4**(9): p. 3287-3295.

22. Lin, D., et al., *High Ionic Conductivity of Composite Solid Polymer Electrolyte via In Situ Synthesis of Monodispersed SiO2 Nanospheres in Poly(ethylene oxide).* Nano Letters, 2016. **16**(1): p. 459-465.

23. Buschmann, H., et al., *Structure and dynamics of the fast lithium ion conductor "Li7La3Zr2O12".* Physical Chemistry Chemical Physics, 2011. **13**(43): p. 19378-19392.

24. Liu, X., J. Fu, and C. Zhang, *Preparation of NASICON-Type Nanosized Solid Electrolyte Li1.4Al0.4Ti1.6(PO4)3 by Evaporation-Induced Self-Assembly for Lithium-Ion Battery.* Nanoscale Research Letters, 2016. **11**(1): p. 551.

25. Fergus, J.W., *Ceramic and polymeric solid electrolytes for lithium-ion batteries.* Journal of Power Sources, 2010. **195**(15): p. 4554-4569.

26. Suo, L., et al., *A new class of Solvent-in-Salt electrolyte for high-energy rechargeable metallic lithium batteries.* Nature Communications, 2013. **4**: p. 1481.

27. Hasegawa, S., et al., *Study on lithium/air secondary batteries—Stability of NASICON-type lithium ion conducting glass–ceramics with water.* Journal of Power Sources, 2009. **189**(1): p. 371-377.

28. Knauth, P., *Inorganic solid Li ion conductors: An overview.* Solid State Ionics, 2009. **180**(14–16): p. 911-916.

29. Imanishi, N., et al., *Lithium anode for lithium-air secondary batteries.* Journal of Power Sources, 2008. **185**(2): p. 1392-1397.

30. Wang, C., et al., *Suppression of Lithium Dendrite Formation by Using LAGP-PEO (LiTFSI) Composite Solid Electrolyte and Lithium Metal Anode Modified by PEO (LiTFSI) in All-Solid-State Lithium Batteries.* ACS Applied Materials & Interfaces, 2017. **9**(15): p. 13694-13702.

31. Kitaura, H. and H. Zhou, *Electrochemical performance and reaction mechanism of all-solid-state lithium–air batteries composed of lithium, Li1+xAlyGe2−y(PO4)3 solid electrolyte and carbon nanotube air electrode.* Energy & Environmental Science, 2012. **5**(10): p. 9077-9084.

32. Ohta, S., et al., *Electrochemical performance of an all-solid-state lithium ion battery with garnet-type oxide electrolyte.* Journal of Power Sources, 2012. **202**: p. 332-335.

33. Kokal, I., et al., *Sol-gel synthesis and lithium ion conductivity of Li7La3Zr2O12 with garnet-related type structure.* Solid State Ionics, 2011. **185**(1): p. 42-46.

34. Lim, Y.J., et al., *Ceramic-Based Composite Solid Electrolyte for Lithium-Ion Batteries.* ChemPlusChem, 2015. **80**(7): p. 1100-1103.

35. Ohta, N., et al., *Enhancement of the High-Rate Capability of Solid-State Lithium Batteries by Nanoscale Interfacial Modification.* Advanced Materials, 2006. **18**(17): p. 2226-2229.

36. Scrosati, B. and J. Garche, *Lithium batteries: Status, prospects and future.* Journal of Power Sources, 2010. **195**(9): p. 2419-2430.

37. Manuel Stephan, A. and K.S. Nahm, *Review on composite polymer electrolytes for lithium batteries.* Polymer, 2006. **47**(16): p. 5952-5964.

38. Yang, C.-M., et al., *Gel-type polymer electrolytes with different types of ceramic fillers and lithium salts for lithium-ion polymer batteries.* Journal of Power Sources, 2006. **156**(2): p. 574-580.

39. Liu, Y., J.Y. Lee, and L. Hong, *Morphology, crystallinity, and electrochemical properties of in situ formed poly(ethylene oxide)/TiO2 nanocomposite polymer electrolytes.* Journal of Applied Polymer Science, 2003. **89**(10): p. 2815-2822.

40. Croce, F., S. Sacchetti, and B. Scrosati, *Advanced, lithium batteries based on high-performance composite polymer electrolytes.* Journal of Power Sources, 2006. **162**(1): p. 685-689.

41. Liu, W.L., N.; Sun, J.; Hsu, P.-C.; Li, Y.; Lee, H.-W.; Cui, Y., *Ionic Conductivity Enhancement of Polymer Electrolytes with Ceramic Nanowire Fillers.* Nano Letters, 2015. **15**(4): p. 2740-2745.

42. Langer, F., et al., *Microstructure and temperature dependent lithium ion transport of ceramic–polymer composite electrolyte for solid-state lithium ion batteries based on garnet-type Li7La3Zr2O12.* Solid State Ionics, 2016. **291**: p. 8-13.

43. Liu, W., et al., *Interfacial Impedance Studies of Multilayer Structured Electrolyte Fabricated With Solvent-Casted PEO10–LiN(CF3SO2)2 and Ceramic Li1.3Al0.3Ti1.7(PO4)3 and Its Application in All-Solid-State Lithium Ion Batteries.* Journal of Electrochemical Energy Conversion and Storage, 2016. **13**(2): p. 021008-021008-6.

44. Wang, Y.-J., Y. Pan, and L. Chen, *Ion-conducting polymer electrolyte based on poly(ethylene oxide) complexed with Li1.3Al0.3Ti1.7(PO4)3 salt.* Materials Chemistry and Physics, 2005. **92**(2–3): p. 354-360.

45. Dudney, N. and S. Kalnaus. *https://energy.gov/sites/prod/files/2015/06/f23/es182_dudney_2015_o.pdf*. 2015 [cited 2016 September 26 2016].

46. Wicklein, B., et al., *Thermally insulating and fire-retardant lightweight anisotropic foams based on nanocellulose and graphene oxide.* Nat Nano, 2015. **10**(3): p. 277-283.

47. Sander, J.S., et al., *High-performance battery electrodes via magnetic templating.* Nature Energy, 2016. **1**: p. 16099.

48. Deville, S., et al., *Freezing as a path to build complex composites.* Science, 2006. **311**(5760): p. 515-518.

49. Deville, S., *Freeze-casting of porous ceramics: A review of current achievements and issues.* Advanced Engineering Materials, 2008. **10**(3): p. 155-169.

50. Pawelec, K.M., et al., *Ice-templated structures for biomedical tissue repair: From physics to final scaffolds.* Applied Physics Reviews, 2014. **1**(2).

51. Deville, S., *Ice-templating, freeze casting: Beyond materials processing.* Journal of Materials Research, 2013. **28**(17): p. 2202-2219.

52. Kawahara, H., *The structures and functions of ice crystal-controlling proteins from bacteria.* Journal of Bioscience and Bioengineering, 2002. **94**(6): p. 492-496.

53. Gutierrez, M.C., M.L. Ferrer, and F. del Monte, *Ice-templated materials: Sophisticated structures exhibiting enhanced functionalities obtained after unidirectional freezing and ice-segregation-induced self-assembly.* Chemistry of Materials, 2008. **20**(3): p. 634-648.

54. Duluard, S., et al., *Lithium conducting solid electrolyte Li1.3Al0.3Ti1.7(PO4)(3) obtained via solution chemistry.* Journal of the European Ceramic Society, 2013. **33**(6): p. 1145-1153.

55. Liu, W., et al., *Novel Structured Electrolyte for All-Solid-State Lithium Ion Batteries.* 2015(56611): p. V001T02A002.

56. Wang, C.S., X.W. Zhang, and A.J. Appleby, *Solvent-free composite PEO-ceramic fiber/mat electrolytes for lithium secondary cells.* Journal of the Electrochemical Society, 2005. **152**(1): p. A205-A209.

57. Khan, M.S. and S. Sultana, *Synthesis and Properties of High Strength Thin Film Composites of Poly(ethylene Oxide) and PEO-PMMA Blend with Cetylpyridinium Chloride Modified Clay.* International Journal of Polymer Science, 2015. **2015**: p. 10.

58. Tung, S.-O., et al., *A dendrite-suppressing composite ion conductor from aramid nanofibres.* Nature Communications, 2015. **6**: p. 6152.

59. Khurana, R., et al., *Suppression of Lithium Dendrite Growth Using Cross-Linked Polyethylene/Poly(ethylene oxide) Electrolytes: A New Approach for Practical Lithium-Metal Polymer Batteries.* Journal of the American Chemical Society, 2014. **136**(20): p. 7395-7402.

60. Croce, F., et al., *Nanocomposite polymer electrolytes for lithium batteries.* Nature, 1998. **394**(6692): p. 456-458.

61. Zheng, J., M. Tang, and Y.-Y. Hu, *Lithium Ion Pathway within Li7La3Zr2O12-Polyethylene Oxide Composite Electrolytes.* Angewandte Chemie International Edition, 2016. **55**(40): p. 12538-12542.

62. Zhai, H., et al., *A Flexible Solid Composite Electrolyte with Vertically Aligned and Connected Ion-Conducting Nanoparticles for Lithium Batteries.* Nano Letters, 2017. **17**(5): p. 3182-3187.

63. Ma, C., et al., *Excellent Stability of a Lithium-Ion-Conducting Solid Electrolyte upon Reversible Li+/H+ Exchange in Aqueous Solutions.* Angewandte Chemie International Edition, 2015. **54**(1): p. 129-133.

64. Hong, C., et al., *Camphene-based freeze-cast ZrO2 foam with high compressive strength.* Materials Chemistry and Physics, 2010. **119**(3): p. 359-362.

65. Mariappan, C.R., et al., *Grain boundary resistance of fast lithium ion conductors: Comparison between a lithium-ion conductive Li–Al–Ti–P–O-type glass ceramic and a Li1.5Al0.5Ge1.5P3O12 ceramic.* Electrochemistry Communications, 2012. **14**(1): p. 25-28.

66. Guo, Q., et al., *New Class of LAGP-Based Solid Polymer Composite Electrolyte for Efficient and Safe Solid-State Lithium Batteries.* ACS Applied Materials & Interfaces, 2017. **9**(48): p. 41837-41844.

67. Bachman, J.C., et al., *Inorganic Solid-State Electrolytes for Lithium Batteries: Mechanisms and Properties Governing Ion Conduction.* Chemical Reviews, 2016. **116**(1): p. 140-162.

68. Tsai, P.-C., et al., *Single-particle measurements of electrochemical kinetics in NMC and NCA cathodes for Li-ion batteries.* Energy & Environmental Science, 2018. **11**(4): p. 860-871.

69. Hess, S., M. Wohlfahrt-Mehrens, and M. Wachtler, *Flammability of Li-Ion Battery Electrolytes: Flash Point and Self-Extinguishing Time Measurements.* Journal of The Electrochemical Society, 2015. **162**(2): p. A3084-A3097.

70. MacFarlane, D.R., et al., *Energy applications of ionic liquids.* Energy & Environmental Science, 2014. **7**(1): p. 232-250.

71. Radin, M.D., et al., *Narrowing the Gap between Theoretical and Practical Capacities in Li-Ion Layered Oxide Cathode Materials.* Advanced Energy Materials, 2017. **7**(20): p. 1602888.

72. Zhang, J., et al., *Flexible and ion-conducting membrane electrolytes for solid-state lithium batteries: Dispersion of garnet nanoparticles in insulating polyethylene oxide.* Nano Energy, 2016. **28**: p. 447-454.

73. Ma, J., et al., *A Strategy to Make High Voltage LiCoO2 Compatible with Polyethylene Oxide Electrolyte in All-Solid-State Lithium Ion Batteries.* Journal of The Electrochemical Society, 2017. **164**(14): p. A3454-A3461.

74. Jiao, S., et al., *Behavior of Lithium Metal Anodes under Various Capacity Utilization and High Current Density in Lithium Metal Batteries.* Joule, 2018. **2**(1): p. 110-124.

75. Li, S., et al., *A Superionic Conductive, Electrochemically Stable Dual-Salt Polymer Electrolyte.* Joule, 2018.

76. Zheng, J., et al., *Electrolyte additive enabled fast charging and stable cycling lithium metal batteries.* Nature Energy, 2017. **2**(3).

77. Ji, H., et al., *Capacitance of carbon-based electrical double-layer capacitors.* Nature Communications, 2014. **5**: p. 3317.

78. Sun, Y.K., et al., *The role of AlF3 coatings in improving electrochemical cycling of Li-enriched nickel-manganese oxide electrodes for Li-ion batteries.* Adv Mater, 2012. **24**(9): p. 1192-6.

79. Xie, J., et al., *Atomic Layer Deposition of Stable LiAlF4 Lithium Ion Conductive Interfacial Layer for Stable Cathode Cycling.* ACS Nano, 2017. **11**(7): p. 7019-7027.

80. Makarowicz, A., et al., *Electronic structure of Lewis acid sites on high surface area aluminium fluorides: a combined XPS and ab initio investigation.* Physical Chemistry Chemical Physics, 2009. **11**(27): p. 5664-5673.

81. Jiao, S., et al., *Stable cycling of high-voltage lithium metal batteries in ether electrolytes.* Nature Energy, 2018.

82. Fleutot, B., et al., *Surface film morphology (AFM) and chemical features (XPS) of cycled V2O5 thin films in lithium microbatteries.* Journal of Power Sources, 2008. **180**(2): p. 836-844.

83. Zhao, W., et al., *High Voltage Operation of Ni-Rich NMC Cathodes Enabled by Stable Electrode/Electrolyte Interphases.* Advanced Energy Materials, 2018. **8**(19).

84. Bergmann, A., et al., *Reversible amorphization and the catalytically active state of crystalline Co3O4 during oxygen evolution.* Nat Commun, 2015. **6**: p. 8625.

85. Bodenes, L., et al., *The Solid Electrolyte Interphase a key parameter of the high performance of Sb in sodium-ion batteries: Comparative X-ray Photoelectron Spectroscopy study of Sb/Na-ion and Sb/Li-ion batteries.* Journal of Power Sources, 2015. **273**: p. 14-24.

86. Armand, M., et al., *Ionic-liquid materials for the electrochemical challenges of the future.* Nature materials, 2009. **8**(8): p. 621.

87. Xu, K., *Nonaqueous liquid electrolytes for lithium-based rechargeable batteries.* Chemical reviews, 2004. **104**(10): p. 4303-4418.

88. Goodenough, J.B. and K.-S. Park, *The Li-ion rechargeable battery: a perspective.* Journal of the American Chemical Society, 2013. **135**(4): p. 1167-1176.

89. Lin, D., Y. Liu, and Y. Cui, *Reviving the lithium metal anode for high-energy batteries.* Nature nanotechnology, 2017. **12**(3): p. 194.

90. Cheng, X.-B., et al., *Dual-phase lithium metal anode containing a polysulfide-induced solid electrolyte interphase and nanostructured graphene framework for lithium–sulfur batteries.* ACS nano, 2015. **9**(6): p. 6373-6382.

91. Cheng, X.-B., et al., *Implantable solid electrolyte interphase in lithium-metal batteries.* Chem, 2017. **2**(2): p. 258-270.

92. Cheng, X.-B., et al., *Sulfurized solid electrolyte interphases with a rapid Li+ diffusion on dendrite-free Li metal anodes.* Energy Storage Materials, 2018. **10**: p. 199-205.

93. Cheng, X.-B. and Q. Zhang, *Dendrite-free lithium metal anodes: stable solid electrolyte interphases for high-efficiency batteries.* Journal of Materials Chemistry A, 2015. **3**(14): p. 7207-7209.

94. Rettenwander, D., et al., *Structural and electrochemical consequences of Al and Ga cosubstitution in Li7La3Zr2O12 solid electrolytes.* Chemistry of Materials, 2016. **28**(7): p. 2384-2392.

95. Yang, C., et al., *Flexible Aqueous Li‐Ion Battery with High Energy and Power Densities.* Advanced Materials, 2017. **29**(44).

96. Zhai, H., et al., *A Flexible Solid Composite Electrolyte with Vertically Aligned and Connected Ion-Conducting Nanoparticles for Lithium Batteries.* Nano Lett, 2017. **17**(5): p. 3182-3187.

97. Fu, K.K., et al., *Flexible, solid-state, ion-conducting membrane with 3D garnet nanofiber networks for lithium batteries.* Proceedings of the National Academy of Sciences, 2016. **113**(26): p. 7094-7099.

98. Tao, X., et al., *Solid-State Lithium–Sulfur Batteries Operated at 37° C with Composites of Nanostructured Li7La3Zr2O12/Carbon Foam and Polymer.* Nano letters, 2017. **17**(5): p. 2967-2972.

99. Zhao, C.-Z., et al., *An anion-immobilized composite electrolyte for dendrite-free lithium metal anodes.* Proceedings of the National Academy of Sciences, 2017. **114**(42): p. 11069-11074.

100. Cheng, L., et al., *Effect of surface microstructure on electrochemical performance of garnet solid electrolytes.* ACS applied materials & interfaces, 2015. **7**(3): p. 2073-2081.

101. Cheng, L., et al., *Enhanced lithium ion transport in garnet-type solid state electrolytes.* Journal of Electroceramics, 2017. **38**(2-4): p. 168-175.

102. Yao, X., et al., *High‐Performance All‐Solid‐State Lithium–Sulfur Batteries Enabled by Amorphous Sulfur‐Coated Reduced Graphene Oxide Cathodes.* Advanced Energy Materials, 2017. **7**(17).

103. Lin, D., et al., *High ionic conductivity of composite solid polymer electrolyte via in situ synthesis of monodispersed SiO2 nanospheres in poly (ethylene oxide).* Nano letters, 2015. **16**(1): p. 459-465.

104. Xue, Z., D. He, and X. Xie, *Poly (ethylene oxide)-based electrolytes for lithium-ion batteries.* Journal of Materials Chemistry A, 2015. **3**(38): p. 19218-19253.

105. Liu, W., et al., *Flexible and stretchable energy storage: recent advances and future perspectives.* Advanced materials, 2017. **29**(1).

106. Fu, K.K., et al., *Toward garnet electrolyte–based Li metal batteries: An ultrathin, highly effective, artificial solid-state electrolyte/metallic Li interface.* Science Advances, 2017. **3**(4): p. e1601659.

107. Liu, W., et al., *Enhancing ionic conductivity in composite polymer electrolytes with well-aligned ceramic nanowires.* Nature energy, 2017. **2**(5): p. 17035.

108. Liu, W., et al., *Improved lithium ionic conductivity in composite polymer electrolytes with oxide-ion conducting nanowires.* ACS nano, 2016. **10**(12): p. 11407-11413.

109. Zhang, J., et al., *High-voltage and free-standing poly (propylene carbonate)/Li 6.75 La 3 Zr 1.75 Ta 0.25 O 12 composite solid electrolyte for wide temperature range and flexible solid lithium ion battery.* Journal of Materials Chemistry A, 2017. **5**(10): p. 4940-4948.

110. Li, J., et al., *Solid Electrolyte: the Key for High-Voltage Lithium Batteries.* Advanced Energy Materials, 2015. **5**(4).

111. Zhang, X., et al., *Synergistic Coupling between Li6.75La3Zr1.75Ta0.25O12 and Poly(vinylidene fluoride) Induces High Ionic Conductivity, Mechanical Strength, and Thermal Stability of Solid Composite Electrolytes.* J Am Chem Soc, 2017. **139**(39): p. 13779-13785.

112. Zuo, S., et al., *Preparation of 3D interconnected hierarchical porous N-doped carbon nanotubes.* Carbon, 2018. **129**: p. 199-206.

113. Murray, H.H., *Traditional and new applications for kaolin, smectite, and palygorskite: a general overview.* Applied clay science, 2000. **17**(5-6): p. 207-221.

114. Kiener, C.A., et al., *Identification of an Activated Catalyst in the Iridium-Catalyzed Allylic Amination and Etherification. Increased Rates, Scope, and Selectivity.* Journal of the American Chemical Society, 2003. **125**(47): p. 14272-14273.

115. Kuzmin, A.N., et al., *Resonance Raman Probes for Organelle-Specific Labeling in Live Cells.* Scientific Reports, 2016. **6**: p. 28483.

116. Giorgini, M.G., et al., *Solvation Structure around the Li+ Ion in Mixed Cyclic/Linear Carbonate Solutions Unveiled by the Raman Noncoincidence Effect.* The Journal of Physical Chemistry Letters, 2015. **6**(16): p. 3296-3302.

117. Zhang, X., et al., *Synergistic Coupling between Li6.75La3Zr1.75Ta0.25O12 and Poly(vinylidene fluoride) Induces High Ionic Conductivity, Mechanical Strength, and Thermal Stability of Solid Composite Electrolytes.* Journal of the American Chemical Society, 2017. **139**(39): p. 13779-13785.

118. Bachman, J.C., et al., *Inorganic solid-state electrolytes for lithium batteries: mechanisms and properties governing ion conduction.* Chemical reviews, 2015. **116**(1): p. 140-162.

119. Monroe, C. and J. Newman, *The impact of elastic deformation on deposition kinetics at lithium/polymer interfaces.* Journal of the Electrochemical Society, 2005. **152**(2): p. A396-A404.

120. Tikekar, M.D., L.A. Archer, and D.L. Koch, *Stabilizing electrodeposition in elastic solid electrolytes containing immobilized anions.* Science Advances, 2016. **2**(7): p. e1600320.

121. Qiu, Y.P. and G.J. Weng, *On the application of Mori-Tanaka's theory involving transversely isotropic spheroidal inclusions.* International Journal of Engineering Science, 1990. **28**(11): p. 1121-1137.

122. Chen, Y., et al., *Effects of geometrical and mechanical properties of fiber and matrix on composite fracture toughness.* Composite Structures, 2015. **122**: p. 496-506.

123. Bruce, P.G. and C.A. Vincent, *Steady state current flow in solid binary electrolyte cells.* Journal of electroanalytical chemistry and interfacial electrochemistry, 1987. **225**(1-2): p. 1-17.

124. Zhang, W.Q., et al., *A durable and safe solid-state lithium battery with a hybrid electrolyte membrane.* Nano Energy, 2018. **45**: p. 413-419.

125. Scrosati, B., F. Croce, and S. Panero, *Progress in lithium polymer battery R&D.* Journal of Power Sources, 2001. **100**(1): p. 93-100.

126. Sheng, O., et al., *Mg2B2O5 Nanowire Enabled Multifunctional Solid-State Electrolytes with High Ionic Conductivity, Excellent Mechanical Properties, and Flame-Retardant Performance.* Nano letters, 2018.

127. Zhang, X., et al., *Synergistic Coupling between Li6.75La3Zr1.75Ta0.25O12 and Poly(vinylidene fluoride) Induces High Ionic Conductivity, Mechanical Strength, and Thermal Stability of Solid Composite Electrolytes.* Journal of the American Chemical Society, 2017. **139**(39): p. 13779-13785.

128. Wu, M., et al., *Electrochemical behaviors of a Li3N modified Li metal electrode in secondary lithium batteries.* Journal of Power Sources, 2011. **196**(19): p. 8091-8097.

129. Li, N.W., et al., *A Flexible Solid Electrolyte Interphase Layer for Long‐Life Lithium Metal Anodes.* Angewandte Chemie International Edition, 2018. **57**(6): p. 1505-1509.